Masterarbeit

A photoionization scheme to create cold ionic impurities from Rydberg atoms

Christian Tomschitz
23. Oktober 2018

Hauptberichter: Prof. Dr. Tilman Pfau
Mitberichter: PD Dr. Eberhard Goering

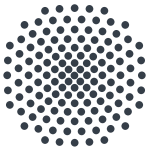

Universität Stuttgart
5. Physikalisches Institut

vorgelegt an der
Universität Stuttgart
5. Physikalisches Institut
Pfaffenwaldring 57
70569 Stuttgart

Eidesstattliche Erklärung

Hiermit versichere ich gemäß §24 Absatz 7 der Prüfungsordnung der Universität Stuttgart für den Masterstudiengang Physik vom 31. Juli 2015, dass ich diese Arbeit selbständig verfasst habe, dass ich keine anderen als die angegebenen Quellen benutzt und alle wörtlich oder sinngemäß aus anderen Werken übernommenen Aussagen als solche gekennzeichnet habe. Ich versichere, dass die eingereichte Arbeit weder vollständig noch in wesentlichen Teilen Gegenstand eines anderen Prüfungsverfahrens gewesen ist. Weiterhin versichere ich, dass das elektronische Exemplar mit dem Inhalt der Druckexemplare übereinstimmt.

Christian Tomschitz
Stuttgart, den 23. Oktober 2018

Deutsche Zusammenfassung

Im Zuge dieser Masterarbeit wurde ein neuartiges Photoionisationsschema implementiert, mit dem hochangeregte Rydbergatome in kalte Ionen umgewandelt werden können. Bei diesem sogenannten V-Schema werden Rydbergatome in den Zwischenzustand $|6P_{3/2}\rangle$ des Elements Rubidium abgeregt. Dies geschieht mit einem Laser bei einer Wellenlänge von etwa 1020 nm. Mit einem weiteren infraroten Laser werden die Atome bei einer Wellenlänge von 1010 nm aus dem Zwischenzustand photoionisiert. Um kalte Ionen mit möglichst geringer kinetischer Energie zu erzeugen, muss der Photoionisationslaser möglichst nah über die Ionisationsschwelle eingestellt werden. Für kurze Ionisationszeiten sind dazu hohe Intensitäten des Photoionisationslasers notwendig. Auf diese Art ist es möglich, mit hohen Repetitionsraten kalte Ionen zu erzeugen.

Im Rahmen dieser Arbeit wurde das Lasersystem für die Photoionisation aufgebaut. Der Aufbau besteht im Wesentlichen aus einem Toptica DLpro Laser mit einer optischen Ausgangsleistung von etwa 28 mW bei einer Wellenlänge von 1010 nm. Des Weiteren wurde ein selbstgebauter Transferresonator verwendet, der die Frequenzstabilisierung des Photoionisationslasers mit Hilfe eines frequenzstabilisierten 780 nm Lasers ermöglicht. Ein Halbleiterlaserverstärker wurde eingebaut, welcher die nötige optische Leistung in der Größenordnung von 1 W liefert, die für eine schnelle und effiziente Photoionisation erforderlich ist.

Für das Photoionisationslasersystem wurde ein neues Transferresonatordesign entworfen, welches sich einerseits durch eine hohe Stabilität auszeichnet, andererseits durch den modularen Aufbau eine Vielzahl an Anwendungsmöglichkeiten zulässt. Der selbstgebaute Transferresonator besteht aus zwei kommerziell erhältlichen Spiegelhaltern, die mit einem Edelstahlrohr fest verschraubt werden. Auf beide Spiegelhalter sind Rohre geschraubt, welche die Spiegel des Transferresonators und einen Piezokristall zur periodischen Längenänderung des Transferresonators beinhalten. Die Charakterisierung des Transferresonators ergab einen freien Spektralbereich von 928(65) MHz. Für die Finesse des Transferresonators wurden 143(53) für das Licht des 780 nm Lasers und 371(41) für Licht des 1010 nm Laser ermittelt.

Um die Zeitskala zu untersuchen, auf welcher der Photoionisationsprozess stattfindet, wurden Simulationen durchgeführt. Dazu wurden die optischen Blochgleichungen des im ersten Abschnitt beschriebenen Dreiniveausystems numerisch gelöst. In den Simulationen wird der Übergang vom Zwischenzustand ins Kontinuum als laserinduzierter Zerfall beschrieben. Für eine V-förmige Photoionisation aus dem $|40S_{1/2}\rangle$ Rydbergzustand wurden beispielhaft

Simulationen durchgeführt. Die Auswirkung unterschiedlicher Leistungen des Photoionisationslaser auf die Dauer des Photoionisationsprozesses wurde untersucht.

Im Experiment wurde die Photoionisationseffizienz als Funktion der Laserleistung des Photoionisationslasers für eine Photoionisation aus dem $|51S_{1/2}\rangle$ Rydbergzustand untersucht. In weiteren Messungen wurden die Rabioszillationen zwischen dem Rydbergzustand und dem angeregten $|6P_{3/2}\rangle$ Zustand betrachtet. Die Verstimmung des angeregten Zustandes durch den sogenannten AC Stark Effekt wurde als Funktion der Photoionisationslaserleistung gemessen. Aus den Messwerten wurde der Wirkungsquerschnitt der Photoionisation aus dem $|6P_{3/2}\rangle$ Zustand bestimmt. Unter Berücksichtigung von Dephasierungsmechanismen ergab sich ein Wert von $\sigma = 8.9(10) \times 10^{-22}\,\mathrm{m}^2$.

Das im Zuge dieser Masterarbeit aufgebaute Photoionisationslasersystem wurde zudem verwendet, um die Rydbergblockade zu vermessen, die durch ein einzelnes Ion vermittelt wird [1].

Abstract

In this master thesis, a V-type photoionization scheme has been implemented to produce cold ions from rubidium Rydberg atoms. As part of the implementation, a 1010 nm laser system has been set up. The laser system comprises a self-built transfer cavity, which is used to frequency-stabilize the photoionization laser. The cavity is based on a novel design presented in this work.

The V-type photoionization scheme has been analyzed in numerical simulations to gain insight into the timescale of the photoionization process. Furthermore, the ac Stark shift imparted onto the energy levels of the rubidium atoms by the photoionization laser has been studied. Measurements have been performed in order to determine the photoionization cross section of the transition from the $|6P_{3/2}\rangle$ state in ^{87}Rb into the continuum, yielding a value of $8.9(10) \times 10^{-22}\,\mathrm{m}^2$.

The V-type photoionization process and the built laser system have been used to study the Rydberg blockade induced by a single ion [1].

Table of Contents

List of Figures

1 Introduction

1.1 Rydberg atoms

Rydberg atoms are highly excited atoms with one electron orbiting the ionic core on a large radius [2]. They are named after the Swedish physicist Johannes Rydberg [3]. Rydberg atoms can be excited optically using narrow linewidth lasers [4]. They exhibit some interesting general properties that scale with the principal quantum number n. For instance, S-state Rydberg atoms have an increased lifetime compared to lower-lying states, scaling with n^3. The lifetime of the $|50S_{1/2}\rangle$ Rydberg state of ^{87}Rb is around 141 µs [5] compared to about 27 ns for the $|5P_{1/2}\rangle$ excited state [6]. The orbital radius of Rydberg atoms scales with n^2, and their binding energy follows a n^{-2} dependence [2], usually resulting in a weak binding to the ionic core.
This weak binding of the excited electron leads to a large polarizability of Rydberg atoms that scales with n^7. The van der Waals coefficient C_6 scales with n^{11} [4]. This leads to strong, long-range interactions of the Rydberg atoms, which shift the Rydberg energy levels of neighboring atoms, making it impossible to excite two Rydberg atoms within a certain blockade radius r_B at the same time [7–9]. This interesting effect is known as the dipole-induced Rydberg blockade, scaling with n^{11}.
Another mechanism is the ion-induced Rydberg blockade dominated by the charge-induced dipole interaction, scaling with n^7. Due to the giant interactions between Rydberg atoms and a large sensitivity to external fields, Rydberg atoms have sparked the interest of the current research.

Along with ions [10], nitrogen-vacancy centers [11, 12] or quantum dots [13–15], Rydberg atoms show a huge potential for a wide range of applications in the pioneering fields of quantum information technology, quantum computing or quantum communication [16–21].

Many interesting properties of Rydberg atoms have been studied extensively in the course of the past 80 years [22]. By exploiting the above-mentioned, basic properties of Rydberg atoms, significant new discoveries have been made. Only some of them are mentioned in the following. Rydberg atoms have been analyzed in ultracold quantum gases, leading to excitations of single Rydberg atoms in a Bose-Einstein condenstate [23]. Two-qubit quantum gates have been explored [24, 25] and Rydberg atoms have been employed to study nonlinear quantum optics down to the single photon level [26, 27]. This progress of Rydberg physics has been closely linked to new developments in laser cooling, atom trapping, and imaging [28, 29].

In the course of research, homonuclear Rydberg molecules, in which a neutral ground state atom is bound to the Rydberg atom due to the interaction with the Rydberg electron, have become a matter of keen interest, and inspired further inquiry [30–37].

1.2 Studying ion-atom scattering in the ultracold regime

The aim of a new experiment at the 5$^{\text{th}}$ Institute for Physics at the University of Stuttgart is to study ion-atom scattering in the ultracold, quantum regime [38]. So far, ion-atom interactions have been studied in the cold regime for different combinations of species [39–49], mainly using Paul traps in combination with a conventional magnetic or optical traps for the neutral atoms. However, due to the micromotion of the ions in Paul traps, the interaction could have been only studied in the essentially classical regime. Until now, the S-wave scattering regime has not yet been reached in any experiment [38].

In the new experiment, either a ^{6}Li*-^{6}Li or a ^{7}Li*-^{7}Li Rydberg molecule will replace the Paul trap. After the Rydberg molecule has been initialized by photoassociation out of an ultracold atomic cloud, the single lithium Rydberg molecule will be photoionized in order to trigger the ultracold scattering process [38]. The outcome of this process will then be detected with high spatial and temporal resolution using a delay-line detector. To magnify the scattering wavefunction up to a factor of 1000, an ion microscope containing three electrostatic lenses will be used [50]. Rydberg molecules have been chosen, since they offer well-defined starting conditions with only one single Rydberg excitation due to the Rydberg blockade and the tight focus of the respective laser beams. Moreover, ion and atom are already close to each other.

To photoionize the Rydberg molecule, a novel V-type photoionization process is employed. In such a V-type scheme, the Rydberg atom gets deexcited into an intermediate state, from where it is photoionized. In contrast to electric field ionization, the photoionization offers high spatial control due to a tight focus of the photoionization beam, and the recoil imparted by the photoionization laser onto the emerging ion is negligible. As the wavelength of the photoionization laser can be tuned directly above the ionization threshold, ultra low-energy ions can be produced, since the electron carries away most of the kinetic energy of the system, and the photoionization allows to minimize the total energy impact onto the ion-atom system.

For the Li^{+}-Li ion-atom system, a photoionization laser which is blue-detuned by maximally 10 GHz from the ionization threshold yields a kinetic energy of the ion that is much smaller than the S-wave scattering limit of the ion-atom system. In order to achieve a diabatic photoionization process for the lithium system (which is to prevent the Rydberg molecule wavefunction from evolving), the timescale is limited to photoionization times on the order of a few ns [38]. The V-type photoionization process can be realized on such a timescale and benefits further from a fast repetition rate.

In the scope of this thesis, the aforementioned V-type photoionization scheme has been implemented. However, it has been exemplified for ^{87}Rb. In the future, the experiment will also feature a lithium oven, and the knowledge gained with the rubidium system can be employed to set up a new photoionization system for lithium.

1.3 About this thesis

This master thesis will be subdivided into seven chapters. This chapter has already given an introduction into the background of Rydberg physics and the novel V-type photoionization scheme. In chapter 2, the theoretical foundations will be outlined. The experimental and optical setup for the V-type photoionization of ^{87}Rb will be presented in chapter 3, and chapter 4 will report on the self-built transfer cavity that is used to frequency-stabilize the 1010 nm photoionization laser. Results of numerical photoionization simulations will be shown in chapter 5. The experiments that have been performed with the photoionization laser system will be outlined and analyzed in chapter 6. Chapter 7 will summarize the content of this thesis, and it will provide an outlook into further research directions. Supplemental material will be attached in the appendix.

2 Theoretical foundations

In this chapter, the theoretical foundations for the mechanisms related to the photoionization of rubidium described in this thesis will be given. At the beginning, there will be a brief review of the element rubidium. The second section will be dedicated to the atom-light interaction, whereas the fundamental theory of optical resonators will be described in the third section. At last, a short introduction into dipole matrix elements in quantum mechanics will be given. Further information on specific topics will be provided in the respective chapters in appropriate detail. For information that is not covered in this thesis, the reader is referred to literature.

2.1 Physical properties of rubidium

Rubidium (derived from the latin expression *rubidus*, deepest red) is an alkali metal with a silver-white apperance [51]. Naturally, the element rubidium consists of two different bosonic isotopes. ^{85}Rb is stable and has a natural abundance of 72.17 % compared to ^{87}Rb with 27.83 %. In the experiment, the weakly radioactive isotope ^{87}Rb (with a half-life of roughly 49 billion years [52]) is used.

As an alkali atom, rubidium has one valence electron. In its $5S_{1/2}$ ground state, the ionization energy $\mathcal{E}_\mathrm{I}$ of a ^{87}Rb atom is 4.177 127 06(10) eV [53]. The nuclear spin of a ^{87}Rb atom is $I = 3/2$. Due to its positive scattering length, ^{87}Rb is a suitable element for Bose-Einstein condensation [54]. Selected properties of ^{87}Rb are presented in Tab. 2.1 along with their numeric value and the reference.

Tab. 2.1: Physical properties of ^{87}Rb.

Property	Symbol	Numeric value	Reference
Atomic number	Z	37	[51]
Number of nucleons	A	87	[51]
Atomic mass	m	$1.443\,160\,684(72) \times 10^{-25}$ kg	[55]
Nuclear spin	I	3/2	[51]
Ionization limit	$\mathcal{E}_\mathrm{I}$	4.177 127 06(10) eV	[53]

2.2 Atom-light interaction

This section will introduce the most important principles of atom-light interactions that are essential in order to fully comprehend the work presented in this thesis. It will outline the density matrix formalism, the temporal evolution of quantum systems, the fundamentals of a three-level system, and the ac Stark effect. However, the subjects covered in the following subsections will provide but a quick overview and will present the notation that is used consistenly throughout the thesis. For a more comprehensive insight in atom-light interactions, the reader will find a comprehensive overview of the subject in standard references such as [56–58].

2.2.1 The atom-light interaction Hamiltonian

A single non-interacting atom with i discrete energy levels $|i\rangle$ with energy eigenvalues $\mathcal{E}_i = \hbar\omega_i$ is represented by the Hamiltonian

$$\mathcal{H}_0 = \sum_i \hbar\omega_i \left|i\right\rangle \left\langle i\right| . \tag{2.1}$$

Commonly, the interaction of an atom with a classical light field is dominated by the electric field component $\mathbf{E}$ of the light field that couples to the atomic dipole moment $\mathbf{d}$. In the dipole-approximation, this interaction is described by the interaction Hamiltonian [59]

$$\mathcal{H}_\mathrm{I} = -\mathbf{d} \cdot \mathbf{E}. \tag{2.2}$$

The electric dipole moment is given by $\mathbf{d} = -e\mathbf{r}$, where e is the elementary charge and $\mathbf{r}$ denotes the position operator. The atom-light interaction Hamiltonian is composed of both $\mathcal{H}_0$ and $\mathcal{H}_\mathrm{I}$ and given by

$$\mathcal{H}_\mathrm{AL} = \mathcal{H}_0 + \mathcal{H}_\mathrm{I}. \tag{2.3}$$

2.2.2 Density matrix formalism

Whenever a pure state in a quantum system can be described by a single wavefunction $|\psi(t)\rangle$, it is possible to define a density operator [60] by the outer product

$$\rho(t) = \left|\psi(t)\right\rangle \left\langle\psi(t)\right| . \tag{2.4}$$

Expanding the wavefunction $|\psi(t)\rangle$ into a complete set of orthonormal basis functions $\{|n\rangle\}$ leads to

$$\left|\psi(t)\right\rangle = \sum_n c_n(t) \left|n\right\rangle \tag{2.5}$$

and the density operator from Eqn. (2.4) becomes

$$\rho(t) = \sum_{n,m} c_n(t) c_m^*(t) \left|n\right\rangle \left\langle m\right| = \sum_{n,m} \rho_{nm}(t) \left|n\right\rangle \left\langle m\right|, \tag{2.6}$$

where the elements $\left\langle n\right| \rho(t) \left|m\right\rangle = \rho_{nm}(t)$ describe the time-dependent matrix elements of the density operator [56]. The diagonal elements $n = m$ of the density matrix in Eqn. (2.6) are called *populations* and the off-diagonal elements $n \neq m$ are referred to as *coherences* as they descibe the coherent superpositions of the states $\left|n\right\rangle$ and $\left|m\right\rangle$. Due to population conservation, the normalization condition of the density matrix is $\mathrm{Tr}[\rho] = 1$, where $\mathrm{Tr}[\rho]$ is the trace of ρ.

Since the density matrix formalism is capable of describing both coherent and incoherent evolutions of atomic ensembles, it will be used within this work in order to describe and compute the time evolution of the quantum systems [58, 61].

2.2.3 Time evolution of quantum systems

By taking the time derivative of the density operator from Eqn. (2.4), one obtains

$$\frac{\partial \rho(t)}{\partial t} = \left(\frac{\partial}{\partial t} \left|\psi(t)\right\rangle\right) \left\langle\psi(t)\right| + \left|\psi(t)\right\rangle \left(\frac{\partial}{\partial t} \left\langle\psi(t)\right|\right). \tag{2.7}$$

Inserting the Schrödinger equation $i\hbar \frac{\partial}{\partial t} \left|\psi(t)\right\rangle = \mathcal{H} \left|\psi(t)\right\rangle$ and its dual expression into Eqn. (2.7) results in the von-Neumann equation

$$\frac{\partial \rho}{\partial t} = -\frac{i}{\hbar} \left[\mathcal{H}, \rho\right], \tag{2.8}$$

that describes the time evolution of a coherent quantum system characterized by the density operator with respect to the Hamiltonian $\mathcal{H}$ [58]. However, the full quantum mechanical description is given by the Liouville-von-Neumann equation

$$\frac{\partial \rho}{\partial t} = -\frac{i}{\hbar} \left[\mathcal{H}, \rho\right] + \mathcal{L}(\rho), \tag{2.9}$$

a master equation, which also includes incoherent processes such as decay or dephasing mechanisms that are included in the Lindblad operator $\mathcal{L}(\rho)$ [62]. For example, the Lindblad operator for a decay between two states $\left|i\right\rangle$ and $\left|j\right\rangle$ at a decay rate Γ_{ij} is given by

$$\mathcal{L}(\rho) = -\frac{1}{2} \sum_{i,j} \Gamma_{ij} \left(C_{ij}^\dagger C_{ij} \rho + \rho C_{ij}^\dagger C_{ij}\right) + \sum_{i,j} \Gamma_{ij} C_{ij} \rho C_{ij}^\dagger, \tag{2.10}$$

where $C_{ij}^\dagger = \left|i\right\rangle \left\langle j\right| = C_{ji}$ is a transition operator [61, 63]. The description of dephasing can be achieved in a similar way that is not presented here.

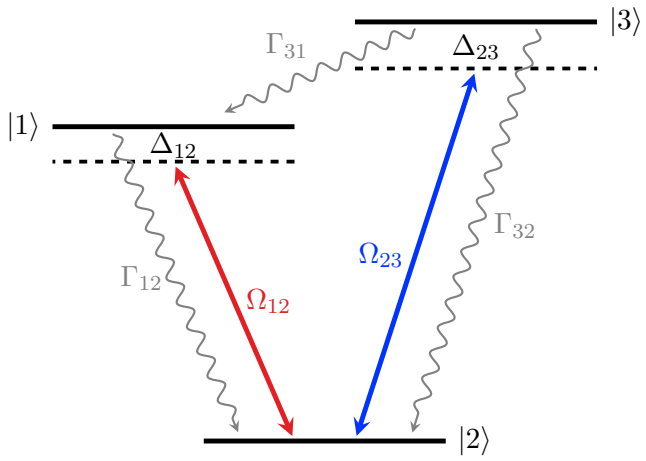

Fig. 2.1: V-type three-level system. The laser-driven transitions between levels $|i\rangle$ and $|j\rangle$ are indicated with corresponding Rabi frequencies Ω_{ij}. The detuning of a laser with respect to the atomic transition is marked with Δ_{ij}. Possible decay paths are denoted with Γ_{ij}. The transition from $|1\rangle$ to $|3\rangle$ is forbidden by selection rules.

2.2.4 V-type three-level system

In this section, an atomic three-level system is examined. A typical representation of such a system is the V-type configuration as shown in Fig. 2.1. In the basis of the three states

$$|1\rangle = \begin{pmatrix} 1 \\ 0 \\ 0 \end{pmatrix}, \qquad |2\rangle = \begin{pmatrix} 0 \\ 1 \\ 0 \end{pmatrix}, \qquad |3\rangle = \begin{pmatrix} 0 \\ 0 \\ 1 \end{pmatrix}, \tag{2.11}$$

the Hamiltonian is diagonal, and following Eqn. (2.1) defined as

$$\mathcal{H}_0 = \begin{pmatrix} \hbar\omega_1 & 0 & 0 \\ 0 & \hbar\omega_2 & 0 \\ 0 & 0 & \hbar\omega_3 \end{pmatrix}. \tag{2.12}$$

The transitions from $|1\rangle$ to $|2\rangle$ and from $|2\rangle$ to $|3\rangle$ are driven with two laser beams described by electric fields

$$\begin{aligned} E_{12} &= \frac{1}{2} E_{0,12} \left(e^{-i\omega_{12}t} + e^{i\omega_{12}t} \right), \\ E_{23} &= \frac{1}{2} E_{0,23} \left(e^{-i\omega_{23}t} + e^{i\omega_{23}t} \right), \end{aligned} \tag{2.13}$$

with amplitudes $E_{0,12}$ and $E_{0,23}$ and angular frequencies ω_{12} and ω_{23}, respectively. Both transitions are far detuned from each other, and the influence of one laser onto the other transition and vice versa can be neglected.

Hence, the interaction Hamiltonian according to Eqn. (2.2) becomes

$$\mathcal{H}_\mathrm{I} = \frac{1}{2}\begin{pmatrix} 0 & -d_{12}E_{12} & 0 \\ -d_{21}E_{21} & 0 & -d_{23}E_{23} \\ 0 & -d_{32}E_{32} & 0 \end{pmatrix}, \tag{2.14}$$

assuming that the transition from $|1\rangle$ to $|3\rangle$ is forbidden by electric dipole selection rules and $E_{ij} = E_{ji}^*$. To simplify the evaluation of the Hamiltonian $\mathcal{H}_\mathrm{AL} = \mathcal{H}_0 + \mathcal{H}_\mathrm{I}$, it is useful to perform a transformation into the rotating frame of the laser frequencies, and to apply the rotating-wave approximation to remove rapidly oscillating terms [57, 64]. In said rotating frame, the atom-light interaction Hamiltonian reads

$$\mathcal{H}_\mathrm{AL} = \hbar\begin{pmatrix} -\Delta_{12} & \frac{1}{2}\Omega_{12} & 0 \\ \frac{1}{2}\Omega_{12}^* & 0 & \frac{1}{2}\Omega_{23} \\ 0 & \frac{1}{2}\Omega_{23}^* & -\Delta_{23} \end{pmatrix}, \tag{2.15}$$

where $\Delta_{12} = (\omega_1 - \omega_2) - \omega_{12}$ and $\Delta_{23} = (\omega_3 - \omega_2) - \omega_{23}$ are the detunings of the lasers with respect to the atomic transitions, $\Omega_{ij} = -d_{ij}E_{ij}/\hbar$ are the Rabi frequencies that express the coupling strength of the respective transition and $\Omega_{ij} = \Omega_{ji}^*$. Furthermore, an energy offset of $-\hbar\omega_2$ has been applied making $|2\rangle$ the zero energy ground state of the system.

To obtain the full temporal evolution of the three-level system, one still has to add the incoherent evolution described by the Lindblad operator. An exact evaluation of Eqn. (2.10) results in

$$\mathcal{L}(\rho) = \begin{pmatrix} \Gamma_{12}\rho_{22} - \Gamma_{31}\rho_{11} & -\frac{1}{2}(\Gamma_{12} + \Gamma_{31} + \Gamma_{32})\rho_{12} & -\frac{1}{2}\Gamma_{31}\rho_{13} \\ -\frac{1}{2}(\Gamma_{12} + \Gamma_{31} + \Gamma_{32})\rho_{21} & -(\Gamma_{12} + \Gamma_{32})\rho_{22} & -\frac{1}{2}(\Gamma_{12} + \Gamma_{32})\rho_{23} \\ -\frac{1}{2}\Gamma_{31}\rho_{31} & -\frac{1}{2}(\Gamma_{12} + \Gamma_{32})\rho_{32} & \Gamma_{31}\rho_{11} + \Gamma_{32}\rho_{22} \end{pmatrix} \tag{2.16}$$

where Γ_{ij} denotes the decay from $|i\rangle$ to $|j\rangle$. Using the Liouville-von-Neumann equation (2.9) it is now possible to describe the dynamics of the considered three-level system [58].

2.2.5 The ac Stark effect

An atom placed inside a monochromatic light field oscillating at an angular frequency ω_L is described by the interaction Hamiltonian

$$\mathcal{H}_\mathrm{I} = -\mathbf{d}\cdot\mathbf{E}, \tag{2.17}$$

where $\mathbf{d}$ is again the electric dipole operator and $\mathbf{E} = \frac{1}{2}\mathbf{E}_0\left(e^{-i\omega_\mathrm{L}t} + e^{i\omega_\mathrm{L}t}\right)$ is the applied electric field [58]. In the presence of an oscillating electric field an atomic level experiences an energy shift, which is called the ac Stark shift (or light shift). It can be calculated using second order time-independent perturbation theory [65].

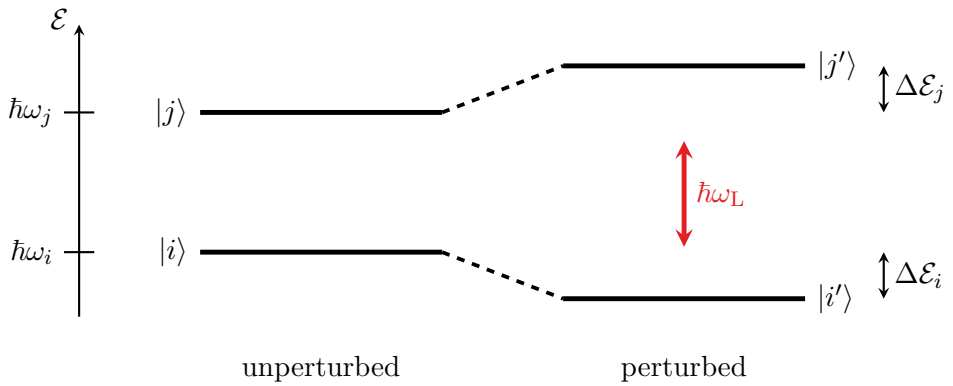

Fig. 2.2: Illustration of the ac Stark shift in a two-level system. On the left the unperturbed states $|i\rangle$ and $|j\rangle$ have an energy difference of $\hbar\omega_{ij}$. A far red-detuned laser beam with $(\omega_{ij} - \omega_\mathrm{L}) > 0$ shifts the two levels by the same energy.

Since the first order shift with respect to $\mathcal{H}_\mathrm{I}$ vanishes in alkali atoms [66], one can analyze the energy shift $\Delta\mathcal{E}_i = \mathcal{E}_i - \mathcal{E}_i^0$ of a level $|i\rangle$ using

$$\Delta\mathcal{E}_i = \sum_{i\neq j} |\langle i|\,\mathcal{H}_\mathrm{I}\,|j\rangle|^2 \left(\frac{1}{\mathcal{E}_i^0 - \mathcal{E}_j^0 + \hbar\omega_\mathrm{L}} + \frac{1}{\mathcal{E}_i^0 - \mathcal{E}_j^0 - \hbar\omega_\mathrm{L}} \right). \tag{2.18}$$

Here, $\mathcal{E}_i^0$ and $\mathcal{E}_j^0$ are the unpertubed eigenenergies of the states $|i\rangle$ and $|j\rangle$, and the sum over j considers all transitions from state $|i\rangle$ that are allowed by electric dipole selection rules. Since the frequency ω_L of the light field may be detuned significantly from the atomic resonance frequency $\omega_{ij} = (\mathcal{E}_j^0 - \mathcal{E}_i^0)/\hbar$, the rotating-wave approximation cannot be applied and hence both co- and counter-rotating terms need to be considered in Eqn. (2.18) [58, 67, 68].

As an example, Fig. 2.2 shows an illustration of the ac Stark effect for only two states $|i\rangle$ and $|j\rangle$. For a red-detunded laser, that is $\omega_{ij} - \omega_\mathrm{L} > 0$, the low-lying state $|i\rangle$ experiences a red-shift whereas the state $|j\rangle$ is shifted towards blue frequencies. The total ac Stark shift is given by $\Delta\mathcal{E}_\mathrm{ac} = \Delta\mathcal{E}_j - \Delta\mathcal{E}_i$.

2.3 Resonator theory

Optical resonators are used in a wide range of applications. Among them are laser resonators surrounding the gain medium, interferometers, optical filters, spectrum analyzers or optical frequency standards such as reference cavities [69]. This section will focus on the latter and will give a theoretical overview on spherical resonators.

In the following, some important general formulae will be presented, the resonator stability conditions will be outlined and the mode-matching of a laser beam and a resonator will be illustrated. A brief discussion on the contribution of transversal modes in resonators will conclude the section.

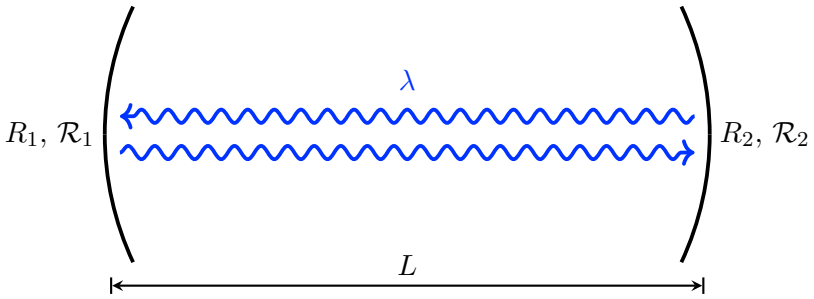

Fig. 2.3: Schematic drawing of a spherical resonator. The two mirrors with curvatures $R_{1,2}$ and reflectivities $\mathcal{R}_{1,2}$ have a distance of L.

2.3.1 Free spectral range and finesse

A spherical resonator consist of two mirrors of reflectivities $\mathcal{R}_{1,2}$ and curvatures $R_{1,2}$ separated by a distance L. Such a resonator is schematically depicted in Fig. 2.3. Light of a laser beam trapped between the two mirrors of this resonator is reflected back and forth. Standing waves as eigenmodes of the resonator emerge once the condition for constructive interference

$$q\frac{\lambda}{2} = L \tag{2.19}$$

is met, where q is an integer and λ the wavelength of the light inside the resonator. Using the relation $c = \nu \cdot \lambda$ with the speed of light c in the respective medium, one obtains the frequency of the q-th mode as

$$\nu_q = \frac{qc}{2L}. \tag{2.20}$$

The constant spacing of two adjacent modes ν_q and ν_{q+1} is called the free spectral range of a resonator [70] and is defined as

$$\Delta\nu_{\mathrm{FSR}} = \nu_{q+1} - \nu_q = \frac{c}{2L}. \tag{2.21}$$

Due to the non-unity reflectivities of the two mirrors, light can enter and exit the cavity. The transmitted intensity distribution of the resonator as a function of the light frequency ν is given by

$$I_{\mathrm{T}}(\nu) = I_0 \left[1 + \left(\frac{2\mathcal{F}}{\pi}\right)^2 \sin^2\left(\frac{\pi\nu}{\Delta\nu_{\mathrm{FSR}}}\right)\right]^{-1}. \tag{2.22}$$

A detailled derivation for Eqn. (2.22) is given in Ref. [71]. The parameter $\mathcal{F}$ is called the finesse of a resonator. It is defined as the ratio of the free spectral range and the full width at half maximum (FWHM) of the transmission peaks. It is

$$\mathcal{F} = \frac{\Delta\nu_{\mathrm{FSR}}}{\nu_{\mathrm{FWHM}}} = \frac{\pi\sqrt{\mathcal{R}}}{1-\mathcal{R}}, \tag{2.23}$$

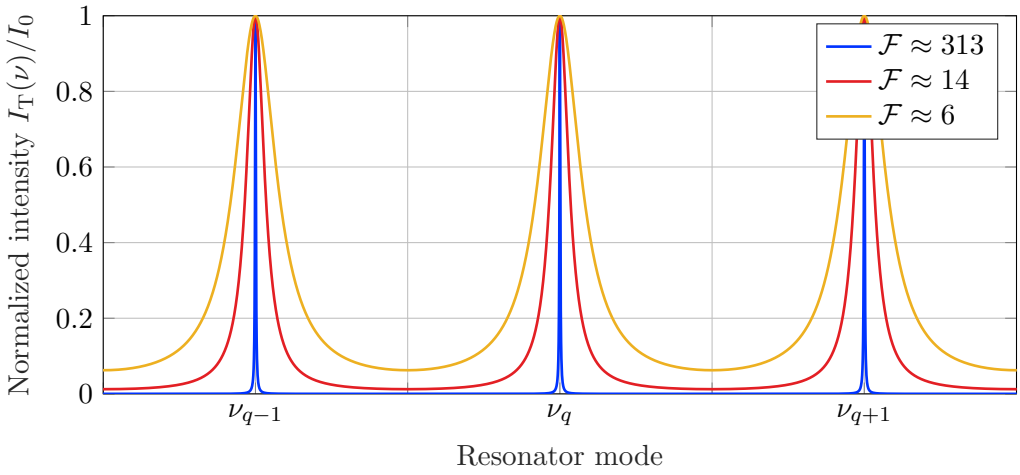

Fig. 2.4: Normalized transmitted light intensity $I_T(\nu)/I_0$ of a spherical resonator as a function of the resonator mode for three different reflectivities $\mathcal{R} = \mathcal{R}_{1,2} = \{0.60, 0.80, 0.99\}$. With increasing reflectivities $\mathcal{R}$ the finesse $\mathcal{F}$ becomes larger and the width ν_{FWHM} of the transmission peaks gets smaller.

where $\mathcal{R} = \sqrt{\mathcal{R}_1 \mathcal{R}_2}$ is the combined reflectivity of both mirrors. The finesse is a measure for the quality of a resonator and proportional to the Q-factor in mechanical oscillators [72]. In Fig 2.4 the spectrum from Eqn. (2.22) is plotted for three different mirror reflectivities.

2.3.2 Resonator stability

There are various types of resonators that use different configurations of concave, convex, planar or spherical mirrors. Not all combinations provide a stable resonator. This section will give a quantitative overview on the criteria for the stability of resonators.

A resonator can be treated as a periodic optical system. Unwrapping the resonator presented in Fig. 2.3 and deconstructing it into a propagation through free space, a mirror, another propagation, and again a mirror makes it easy to describe the resonator within the ray transfer matrix formalism.

A detailed consideration of the eigenvalues of the arising matrix in said formalism [73] yields the stability condition

$$0 \leq g_1 g_2 \leq 1. \tag{2.24}$$

The so-called stability parameters g_i in above inequality are defined by

$$g_i = 1 - \frac{L}{2f_i}. \tag{2.25}$$

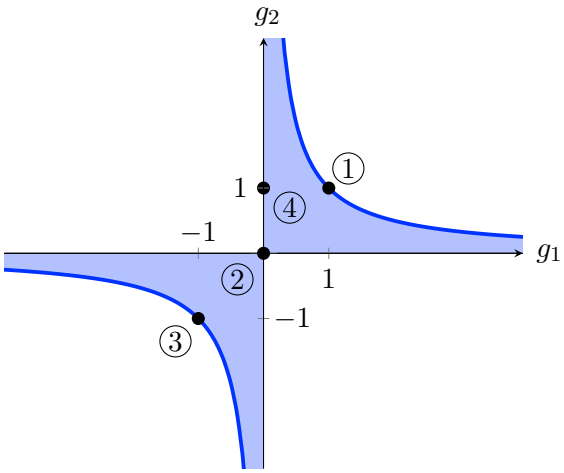

Fig. 2.5: Stability diagram of a resonator. For values g_1 and g_2 in the shaded regions of the plot a resonator fulfills Eqn. (2.25) and is stable. There are four special cases pointed out: (1) planar resonator, (2) confocal resonator, (3) spherical resonator and (4) confocal-planar resonator.

This expression is the general solution for any mirror with focal length f_i [74]. The stability condition from Eqn. (2.24) can be transferred into a stability diagram as shown in Fig. 2.5. In this figure, there are four special cases of resonators pointed out. Note the spherical resonator with $f_i = -R_i/2$ and the confocal-planar resonator with $R_1 = -L$ and $R_2 = \infty$ [74].

2.3.3 Mode matching of light beams and resonators

All considerations in previous sections have been made under the assumption of plane waves light fields. However, laser beams are more accurately described as Gaussian beams. Gaussian beams are the solution of the paraxial Helmholtz equation with axial symmetry. The electric field distribution of Gaussian beams is described by

$$\mathbf{E}(r,z) = \mathbf{E}_0 \frac{w_0}{w(z)} \exp\left(\frac{r^2}{w^2(z)}\right) \times \exp\left(ikz - i\psi(z)\right) \times \exp\left(ik\frac{r^2}{2R(z)}\right). \tag{2.26}$$

The first factor in Eqn. (2.26) describes the amplitude distribution, the second one the longitudinal phase and the third factor the radial phase of the beam [74]. The beam waist at position z is described by

$$w(z) = w_0\sqrt{1 + \left(\frac{z}{z_\mathrm{R}}\right)^2}, \tag{2.27}$$

where w_0 is the minimum beam waist and

$$z_\mathrm{R} = \frac{\pi w_0^2}{\lambda} \tag{2.28}$$

is the Rayleigh length. The curvature of the wavefront of the beam is given by

$$R(z) = z\left[1 + \left(\frac{z_\mathrm{R}}{z}\right)^2\right]. \tag{2.29}$$

Furthermore, k is the wavevector and $\psi(z)$ is the so-called Gouy phase [74], which will be examined more closely in Sec. 2.3.4.

To allow for the best mode matching of the incident laser beam and the resonator, it is mandatory that the curvatures of the mirrors $R_{1,2}$ at positions $z_{1,2}$ match the curvatures of the Gaussian beam at the same positions $z_{1,2}$. Thus, the conditions

$$R_1 = z_1 + \frac{z_\mathrm{R}^2}{z_1}, \qquad R_2 = z_2 + \frac{z_\mathrm{R}^2}{z_2} \qquad \text{with} \qquad z_2 = z_1 + L \tag{2.30}$$

need to apply [75].

2.3.4 Resonance frequencies of a resonator

Gaussian beams as described in Eqn. (2.26) are not the only solution to the paraxial Helmholtz equation. Another solution is given by Hermite-Gaussian beams, that have a transversal intensity profile which is described by two sets of Hermite polynomials [76]. The Hermite-Gaussian modes are labelled with TEM_{lm} where $l, m \in \mathbb{Z}$ and $l, m = 0$ is the Gaussian fundamental mode.

The contribution of Hermite-Gaussian modes as well as the previously introduced Gouy phase $\psi(z)$ change the resonance frequencies of a resonator. In a spherical resonator these are

$$\nu_{q,l,m} = q\Delta\nu_\mathrm{FSR} + (l + m + 1)\,\frac{\Delta\psi(z)}{\pi}\Delta\nu_\mathrm{FSR}, \tag{2.31}$$

where q represents longitudinal modes and l, m label transverse modes [69]. The expression $\Delta\psi(z) = \psi(z_2) - \psi(z_1)$ is the Gouy phase difference with

$$\psi(z) = \arctan\left(\frac{z}{z_\mathrm{R}}\right). \tag{2.32}$$

The Gouy phase difference in Eqn. (2.31) collectively shifts the resonance frequencies of a resonator by a significant fraction of $\Delta\nu_\mathrm{FSR}$. Fundamental modes $l, m = 0$ hence appear at positions

$$\nu_{q,0,0} = \left(q + \frac{\Delta\psi(z)}{\pi}\right)\Delta\nu_\mathrm{FSR}. \tag{2.33}$$

Additionally, higher order modes of a Hermite-Gaussian beam appear in the spectrum of a resonator.

2.4 Dipole matrix elements

This section will give a brief introduction into the quantum mechanical calculation of dipole matrix elements. A transition between two atomic states $|J, m_J\rangle$ and $|J', m_{J'}\rangle$ is coupled by the dipole operator $\mathbf{d} = -e\mathbf{r}$. The dipole matrix element $\boldsymbol{\mu} = \langle J, m_J | \, \mathbf{d} \, | J', m_{J'} \rangle$ determines the coupling strength of said two levels and it arises due to the overlap of the wavefunctions of levels $|J, m_J\rangle$ and $|J', m_{J'}\rangle$. Some physical properties such as radiative lifetimes or transition probabilities can be calculated knowing the quantity of the dipole matrix element [77].

When dealing with angular momenta, it is reasonable to perform a change of basis and approach arising problems in a spherical basis, where the unit vectors $\hat{\mathbf{e}}_q$ are defined by

$$\hat{\mathbf{e}}_{\pm 1} = \mp \frac{1}{\sqrt{2}} (\hat{\mathbf{x}} \pm i\hat{\mathbf{y}}) \qquad \text{and} \qquad \hat{\mathbf{e}}_0 = \hat{\mathbf{z}}, \tag{2.34}$$

where $\hat{\mathbf{x}}$, $\hat{\mathbf{y}}$ and $\hat{\mathbf{z}}$ are the Carthesian basis vectors. The expression of the q-th component of the dipole operator in the new basis is then given by

$$\mathbf{d}_q = -er \sqrt{\frac{4\pi}{3}} Y_1^q(\vartheta, \varphi) \hat{\mathbf{e}}_q. \tag{2.35}$$

Here, $Y_l^m(\vartheta, \varphi)$ are spherical harmonics and $q = \{-1, 0, +1\}$ labels the three different polarizations $\{\sigma^+, \pi, \sigma^-\}$ of light [78].

The Wigner-Eckart theorem allows to factorize the dipole operator into a reduced matrix element and an angular contribution, which can be expressed solely in terms of Clebsch-Gordan coefficients or Wigner 3-j symbols (:::). It is

$$\begin{aligned} \langle J, m_J | \, \mathbf{d}_q \, | J', m_{J'} \rangle &= \langle J \| \mathbf{d} \| J' \rangle \times \langle J, m_J | J', m_{J'}; 1 \; q \rangle \\ &= \langle J \| \mathbf{d} \| J' \rangle \times (-1)^{J'-1+m_J} \sqrt{2J+1} \begin{pmatrix} J' & 1 & J \\ m_{J'} & q & -m_J \end{pmatrix}. \end{aligned} \tag{2.36}$$

The reduced matrix element $\langle J \| \mathbf{d} \| J' \rangle$ contains the radial dependence of the dipole matrix element, while its orientation is fully described by Clebsch-Gordan coefficients [58, 79, 80].

The total angular momentum $\mathbf{J} = \mathbf{L} + \mathbf{S}$ of the atom is a composition of the orbital angular momentum $\mathbf{L}$ and the electron spin $\mathbf{S}$. Since both $\mathbf{L}$ and $\mathbf{S}$ refer to different Hilbert spaces and the dipole operator leaves the electron spin untouched, it is possible to further decompose the reduced matrix element from Eqn. (2.36). Applying the Wigner-Eckart theorem and using Wigner 6-j symbols {:::} yields

$$\langle J \| \mathbf{d} \| J' \rangle = \langle L \| \mathbf{d} \| L' \rangle \times (-1)^{J'+L+1+S} \sqrt{(2J'+1)(2L+1)} \begin{Bmatrix} L & L' & 1 \\ J' & J & S \end{Bmatrix}. \tag{2.37}$$

A further decomposition results in

$$\langle L \| \mathbf{d} \| L' \rangle = \langle nL | \, e\mathbf{r} \, | n'L' \rangle \times (-1)^{-L} \sqrt{2L'+1} \begin{pmatrix} L & 1 & L' \\ 0 & 0 & 0 \end{pmatrix}, \tag{2.38}$$

where

$$\langle nL|\, e\mathbf{r}\, |n'L'\rangle = \boldsymbol{\mu}_{\mathrm{rad}} = \int R^*_{nL}(\mathbf{r}) e\mathbf{r} R_{n'L'}(\mathbf{r}) r^2 \,\mathrm{d}r \tag{2.39}$$

is the radial matrix element with $R_{nL}(\mathbf{r})$ being the radial wavefunctions with respect to the quantum numbers n and L [77].

3 Experimental setup

This chapter will provide an introduction into the Rydberg excitation scheme employed in the experiment and the V-type photoionization scheme implemented in the scope of this thesis. Moreover, the optical setup of the photoionization laser system (1010 nm) and a proposed extension of the Rydberg excitation and deexcitation laser system (1020 nm) will be presented.

3.1 Rydberg excitation and V-type photoionization scheme

To excite atoms to the Rydberg state, a two-photon process is employed using a 420 nm and a 1020 nm laser in a ladder-configuration. Both lasers have a narrow linewidth on the order of 25 kHz [81]. The light of the 420 nm laser is σ^+-polarized and drives the transition from the $|5S_{1/2}, F = 2, m_F = 2\rangle$ ground state to the $|6P_{3/2}, F = 3, m_F = 3\rangle$ intermediate state in ^{87}Rb. The blue laser has a detuning Δ with respect to the atomic resonance frequency, which is discussed later. The setup of the 420 nm laser system is described in Ref. [81].

From the $|6P_{3/2}\rangle$ intermediate state, S- and D-Rydberg states can be adressed using the 1020 nm laser. For S-states σ^--polarized light is used, D-states can be excited with σ^+ polarization. Only $|nS_{1/2}\rangle$ states are considered in this thesis. The wavelength of the infrared laser can be set to any desired wavelength in the range from 1000 to 1025 nm [82], which allows to adress many different Rydberg states with principal quantum number n. More information on the 1020 nm laser system can also be found in Ref. [81].

The excitation scheme as depicted in Fig. 3.1 is called an *inverted scheme* as the laser with the smaller wavelength operates on the transition from the ground to the intermediate state and the infrared laser drives the transition to the Rydberg state. The related *normal scheme* utilizes a 780 nm laser to drive the transition $|5S_{1/2}\rangle \rightarrow |5P_{3/2}\rangle$ and a 480 nm laser to get to the Rydberg state. The inverted scheme has two advantages. Firstly, the available lasers at 1020 nm deliver more optical output power than the 480 nm lasers in the normal scheme [82]. Secondly, the $|6P_{3/2}\rangle$ state with $\tau_{6P_{3/2}} = 112$ ns has a much larger lifetime [83] compared to the $|5P_{3/2}\rangle$ state with $\tau_{5P_{3/2}} = 27$ ns [52] and the dipole matrix elements for the transitions into the Rydberg state are larger [84].

As mentioned above, the transition $|5S_{1/2}, F = 2, m_F = 2\rangle \rightarrow |6P_{3/2}, F = 3, m_F = 3\rangle$ is driven off-resonantly with the blue laser being detuned by $\Delta = 2\pi \times 80$ MHz. Commonly, this detuning is large compared to the Rabi frequencies of the 420 nm and 1020 nm laser

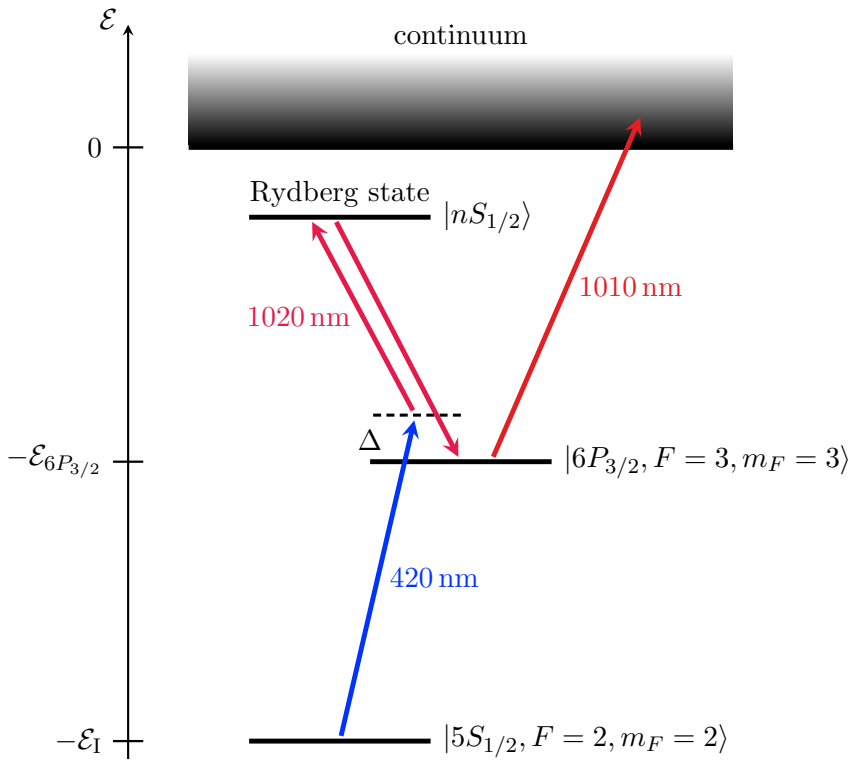

Fig. 3.1: Inverted Rydberg excitation and V-type photoionization scheme in ^{87}Rb. A 420 nm and a tunable 1020 nm laser in ladder-configuration excite atoms from the $|5S_{1/2}\rangle$ ground state to the $|nS_{1/2}\rangle$ Rydberg state. The blue laser is detuned by $\Delta = 2\pi \times 80\,\mathrm{MHz}$ with respect to the atomic resonance frequency to adiabatically eliminate the $|6P_{3/2}\rangle$ intermediate state. The Rydberg deexcitation is driven on resonance with the 1020 nm laser and a high power 1010 nm laser photoionizes the atom.

and large compared to the decay rate of the $|6P_{3/2}\rangle$ state with $\Gamma_{6P_{3/2}} = 2\pi \times 1.42\,\mathrm{MHz}$. Hence, the $|6P_{3/2}\rangle$ intermediate state experiences only a weak coherent coupling to the ground and Rydberg state and does not get populated substantially. This is called the adiabatic elimination of an intermediate state. As a consequence the three-level system can be treated as an effective two-level system $|5S_{1/2}\rangle \rightarrow |nS_{1/2}\rangle$ with an effective two-photon Rabi frequency [85]

$$\Omega_{\mathrm{eff}} = \frac{\Omega_{420}\Omega_{1020}}{2\Delta}. \tag{3.1}$$

Here, Ω_i are the Rabi frequencies of the respective lasers. The adiabatic elimination of the $|6P_{3/2}\rangle$ state allows for a fast and efficient Rydberg excitation [86, 87].

For the photoionization, a two-photon V-type scheme is used by applying the 1020 nm and the 1010 nm laser. The 1020 nm Rydberg laser deexcites the atom in resonance with the $|6P_{3/2}, F = 3, m_F = 3\rangle$ intermediate state using σ^--polarized light. For example, with a waist $w = 5\,\mu\mathrm{m}$ and a laser power of $P = 1\,\mathrm{mW}$ a deexcitation Rabi frequency of $\Omega = 2\pi \times 26\,\mathrm{MHz}$ can readily be achieved in a transition from the $|51S_{1/2}\rangle$ state. The

tuneable photoionization laser operates at a wavelength of 1010 nm. In Sec. 3.2 the setup of the photoionization laser system is described. The photoionization rate from the $|6P_{3/2}\rangle$ state into the continuum is given by

$$\Gamma = \frac{\sigma \lambda I}{hc}, \tag{3.2}$$

which is determined by the photoionization cross section σ, the wavelength λ of the photoionization laser and its intensity I [88]. Further information of the photoionization rate and the treatment of the transition at hand as a decay is given in Sec. 5.1.

The binding energy of the $|6P_{3/2}\rangle$ state is calculated as $\mathcal{E}_{6P_{3/2}} = 2.949\,918\,69\,\text{eV}$, which corresponds to a wavelength of

$$\lambda_{\text{th}} = \frac{hc}{\mathcal{E}_{6P_{3/2}}} = 1010.295\,\text{nm}. \tag{3.3}$$

The absorption of a photon at this wavelength exactly overcomes the binding energy of the atom and gently pushes the electron over the ionization threshold. A consideration of energy and momentum conservation in the emerging electron-ion system yields an electron energy of

$$\mathcal{E}_{e^-} = \frac{m_{\text{ion}}}{m_{\text{ion}} + m_{e^-}} \mathcal{E}_{\text{ex}} \tag{3.4}$$

after the photoionization, where $\mathcal{E}_{\text{ex}} = \mathcal{E}_{1010} - \mathcal{E}_{6P_{3/2}}$ is the excess energy, $\mathcal{E}_{1010}$ is the energy of a photon of the ionization laser, and m_{ion} and m_{e^-} are the masses of the ion and electron, respectively. Since the mass ratio $m_{e^-}/m_{\text{ion}} \ll 1$, the electron carries away most of the kinetic energy of the system leaving a low-energy ion. For instance, the kinetic energy of the electron is $\mathcal{E}_{e^-} = 132\,\mu\text{eV}$ for a photoionization laser wavelength of $\lambda = 1010.186\,\text{nm}$. Furthermore, the excess kinetic energy of the ion can be calculated with

$$\mathcal{E}_{\text{ion}} = \frac{m_{e^-}}{m_{\text{ion}} + m_{e^-}} \mathcal{E}_{\text{ex}} = 0.84\,\text{neV}, \tag{3.5}$$

corresponding to a temperature of $T = 9.7\,\mu\text{K}$.

3.2 Photoionization laser system

In this section, the optical setup of the photoionization laser system will be described. A schematic drawing can be found in Fig. 3.2. The whole setup is placed on a 90 cm × 60 cm breadboard[1] that is mounted on top of the laser table with four 21 cm high stainless steel posts. This laser table extension is mantled within a cage of opaque plexi glass for reasons of laser safety and temperature stability.

[1] Nexus breadboard B6090L

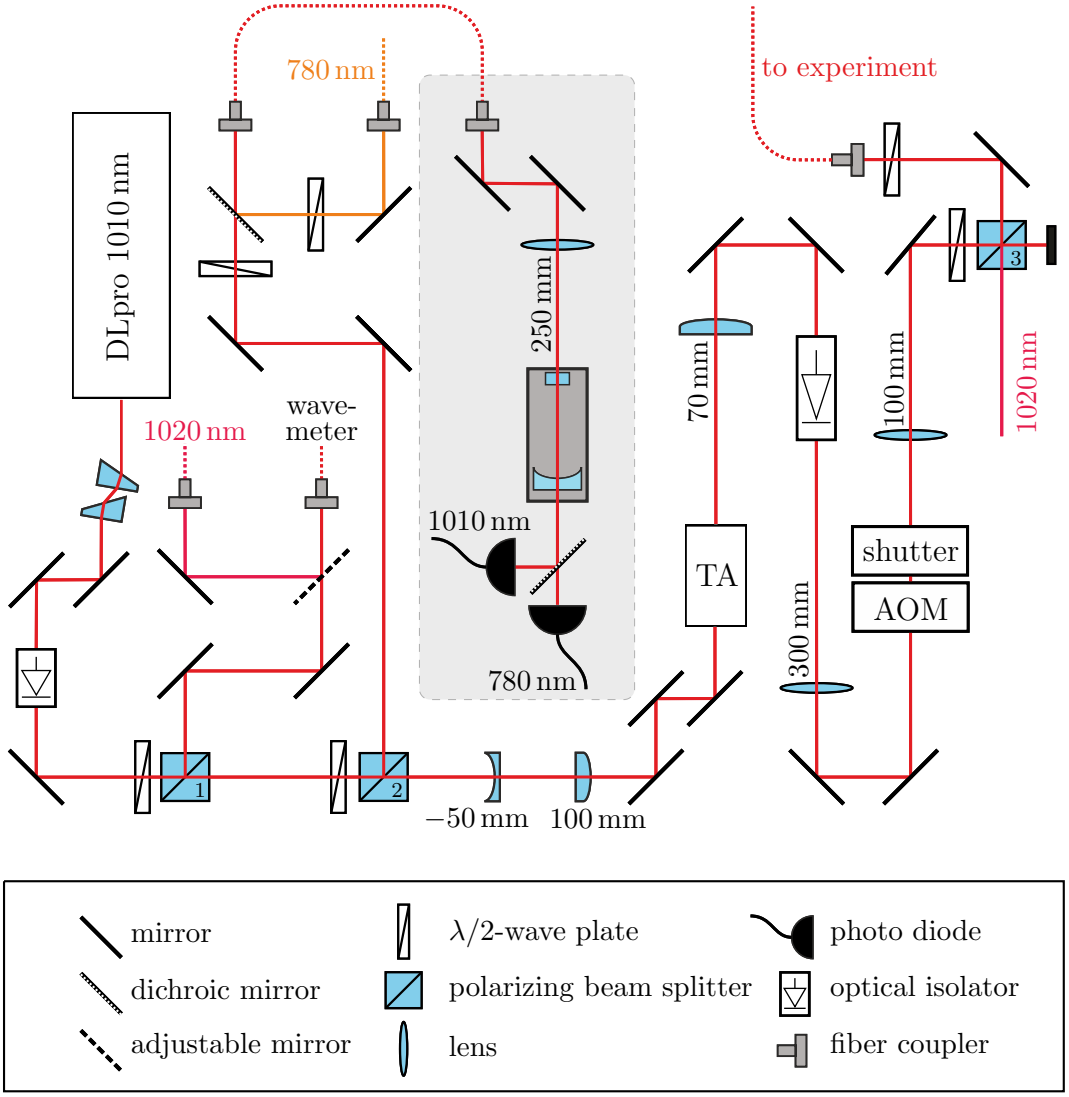

Fig. 3.2: Schematics of the optical setup of the 1010 nm photoionization laser. After the DLpro laser the shape of the beam is adjusted with an anamorphic prism pair to gain a round beam profile. The beam is coupled through an optical isolator. Using a $\lambda/2$-wave plate and a PBS, 2 mW of the beam power is guided to a fiber coupler to the wavemeter. 8 mW of the input power is directed to the cavity branch, where both the photoionization laser and a 780 nm laser are overlapped with the help of a dichroic mirror and coupled into a polarization-maintaining fiber to the transfer cavity. The cavity, mode-matching optics and the detection photo diodes (gray box) are set up on the laser table to give further stability to the cavity. The third branch of the laser (approximately 18 mW) is coupled into a tapered amplifier (TA) using a cylindrical 2:1 telescope. After the TA the laser has a power of 2 W. Subsequently, the beam propagates through a cylindrical beam shaping lens, an optical isolator and is focussed through an AOM and a shutter with the help of a 3:1 telescope. Behind the third PBS, the beam is coupled into a polarization-maintaining fiber to the experiment.

The photoionization laser is a Toptica DLpro laser with a wavelength of 1010 nm. An injection current of 91 mA produces an optical output power of 28 mW. The beam height of the whole setup is 75 mm. Right after the laser output, an anamorphic prism pair is used to transform the input beam into a circular-shaped beam. The laser beam is coupled through an optical isolator[2] using two mirrors. At two polarizing beam splitters (PBS 1 and PBS 2) the beam is divided into three branches. In the following, these three branches are referred to as *wavemeter*, *cavity* and *TA* branch. The abbreviation TA stands for tapered amplifier.

The optical power that is deflected into the wavemeter branch can be adjusted with the $\lambda/2$-wave plate in front of PBS 1. Roughly 2 mW are coupled into the fiber connected to a wavemeter[3]. With an adjustable mirror after the fiber outcoupler, the light of the 1020 nm laser (see Sec. 3.3) from the laser table (see Ref. [81]) can be coupled into the fiber instead of the photoionization laser in order to avoid unplugging fibers at the input ports of the wavemeter.

The combination of the second $\lambda/2$-wave plate and the PBS 2 branches off about 8 mW into the cavity branch. With the help of two mirros and another $\lambda/2$-wave plate, the 1010 nm laser is coupled into a polarization-maintaining single mode fiber. In front of the fiber, a long-pass dichroic mirror[4] is placed. This is where the infrared laser is overlapped with a 780 nm laser, which allows for a co-propagation of both lasers through the fiber.

After the fiber, which is outcoupled on the laser table, both laser beams are coupled into the transfer cavity using two mirrors and a lens with a focal length of 250 mm to fulfill the mode-matching conditions for the cavity. The cavity is used to perform a transfer-lock from the 780 nm laser to the photoionization laser. The light transmitted through the cavity of both lasers is separated with a short-pass dichroic mirror[5] and distributed to a photo diode each. To prevent leakage light from the photoionization laser to reach the photo diode of the 780 nm laser, a band pass filter[6] is installed. The self-built transfer cavity is discussed in appropriate detail in Ch. 4.

In the TA branch, an aberation-balanced [89] and cylindrical 2:1 telescope magnifies the photoionization laser beam in one direction to maximize the overlap of the laser beam with the input facet of the tapered amplifier (TA). The TA itself is seeded with a laser power of 18 mW. An injection current into the TA chip[7] of 5.8 A creates an optical output power of 2 W at 1010 nm. After the TA, a 70 mm cylindrical lens is used to correct the beam shape of the output mode as best as possible. A two-stage optical isolator[8] with an isolation larger than 60 dB prevents reflections into the TA chip [90].

[2] Linos FI-980-3SC
[3] Burleigh WA-10
[4] Thorlabs DMLP950
[5] Thorlabs DMSP950
[6] Thorlabs FB780-10
[7] Dilas TA-1010-2000-CM, facet size $6 \times 1.2\,\mu m^2$
[8] Linos FI-980-5TIC

A 3:1 telescope focuses the laser beam through an acusto-optic modulator[9] (AOM) and a shutter[10]. The first diffraction order of the AOM (+200 MHz) is coupled into a polarization-maintaining fiber to the experiment. Due to the diffraction efficiency of the AOM and the coupling efficiency of the fiber, approximately 500 mW photoionization laser power are available after the fiber. At PBS 3, the photoionization laser can be overlapped with the 1020 nm Rydberg excitation and deexcitation laser (see Sec. 3.3).

3.3 Rydberg excitation and deexcitation laser system

In this section, an extension for the setup of the 1020 nm Rydberg excitation and deexcitation laser will be proposed. The major part of the 1020 nm laser system already exists and is depicted in Fig. 3.7 in Ref. [81].

The main idea of the setup presented in Fig. 3.3 in this work is to overlap three laser beams to have all lasers for the V-type photoionization process accessing the experiment chamber through the same viewport. The two Rydberg lasers for the excitation and deexcitation and the photoionization laser are combined in front of the fiber to the experiment to ensure the overlap of the beams. The proposed setup is described in the following.

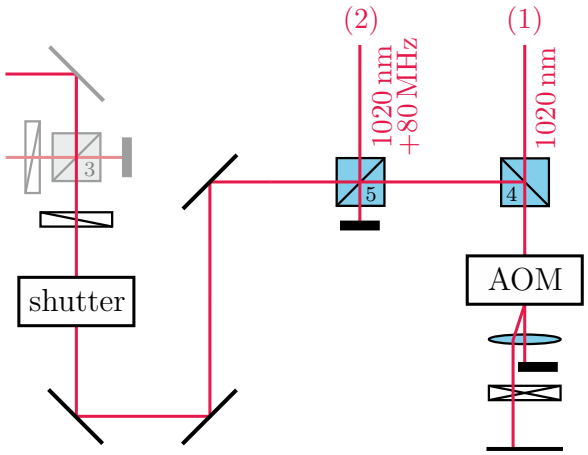

Fig. 3.3: Proposed optical setup of the 1020 nm Rydberg excitation and deexcitation laser system. The first 1020 nm beam (1) is guided through a double-pass AOM with a total frequency modulation of −160 MHz. It is used for the Rydberg deexcitation. The AOM double-pass consists of a lens, a $\lambda/4$-wave plate and a mirror. The second incoming 1020 nm beam (2) is already modulated with +80 MHz and it is directly coupled into the fiber to the experiment via the shutter and PBS 3 serving as the Rydberg excitation laser. The zeroth order of the AOM is blocked. The overlap with the photoionization laser setup in Fig. 3.2 is greyed out in this schematic.

[9] Crystal Technology AOM 3200-1117
[10] Uniblitz LS3ZM2

At PBSC 1 in Ref. [81], the first 1020 nm laser beam is picked up[11]. The second 1020 nm beam (+80 MHz) is picked up just before the fiber to the experiment using a flip mirror. Two periscopes are used to guide the laser beams from the laser table to the setup of the photoionization laser.

Fig. 3.3 illustrates the suggested setup of the Rydberg lasers on the aforementioned laser table extension. Light of the 1020 nm beam (1) without frequency shift is transmitted through PBS 4 and coupled into an AOM in double-pass configuration, leading to a frequency shift of −160 MHz. This laser is used for the Rydberg deexcitation.

The second 1020 nm laser (+80 MHz) is used for the Rydberg excitation. At a 90:10 beam splitter (BS 5), the beam is overlapped with the deexcitation beam and coupled into the fiber to the experiment. A shutter is utilized to block the laser beams.

Since the 420 nm laser is detuned by +80 MHz, the combined frequency shifts of the Rydberg excitation laser (−160 MHz) and the Rydberg deexcitation laser (+80 MHz) ensure that the Rydberg deexcitation laser couples the Rydberg state $|nS_{1/2}\rangle$ resonantly to the $|6P_{3/2}\rangle$ state.

[11] Note the different notation PBSC for polarizing beam splitter cubic, which is used in Ref. [81]

4 Self-built transfer cavity

In this chapter, the self-built transfer cavity will be introduced, and the specific requirements for the cavity will be sketched out. A novel transfer cavity design will be presented and explained. The developed theoretical mode-matching considerations will be continued and applied to the cavity at hand. Finally, the self-built cavity will be characterized and the frequency and length stabilization of both the involved lasers and the cavity will be presented. A tutorial on how to easily adjust the cavity and couple light into it can be found in appendix A.4.

4.1 Requirements

The principal purpose of the cavity is to perform a transfer lock from a laser with wavelength 780 nm to a laser with wavelength 1010 nm. Therefore, a cavity with an active length-stabilization mechanism is needed. This is realized making use of a piezo actuator to keep the cavity at constant length. Due to previous experiences of the institute with plano-concave cavities, this configuration is also used for the cavity presented in this thesis.

In order to produce slow ions and impart as little energy as possible onto them during the photoionization process, the 1010 nm photoionization laser should be tuned close to the ionization threshold of the ^{87}Rb atoms. Therefore, a free spectral range of around $\Delta\nu_{\mathrm{FSR}} \approx 1\,\mathrm{GHz}$ is required. Rearranging Eqn. (2.21) would yield a desired length of the cavity of $L = c/(2\Delta\nu_{\mathrm{FSR}}) = 150\,\mathrm{mm}$. However, the cavity length is chosen to be $L = 160\,\mathrm{mm}$ resulting in a free spectral range of $\Delta\nu_{\mathrm{FSR}} = 937.5\,\mathrm{MHz}$. The reason for the slightly longer cavity is the degeneracy of fundamental and Hermite-Gaussian modes that would appear in a cavity of 150 mm length. This will be briefly discussed in Sec. 4.4.2.

Since a laser linewidth on the order of tens of MHz is sufficient for the photoionization process, no high finesse cavity is needed. Therefore, this aspect is not considered in the conception of the transfer cavity.

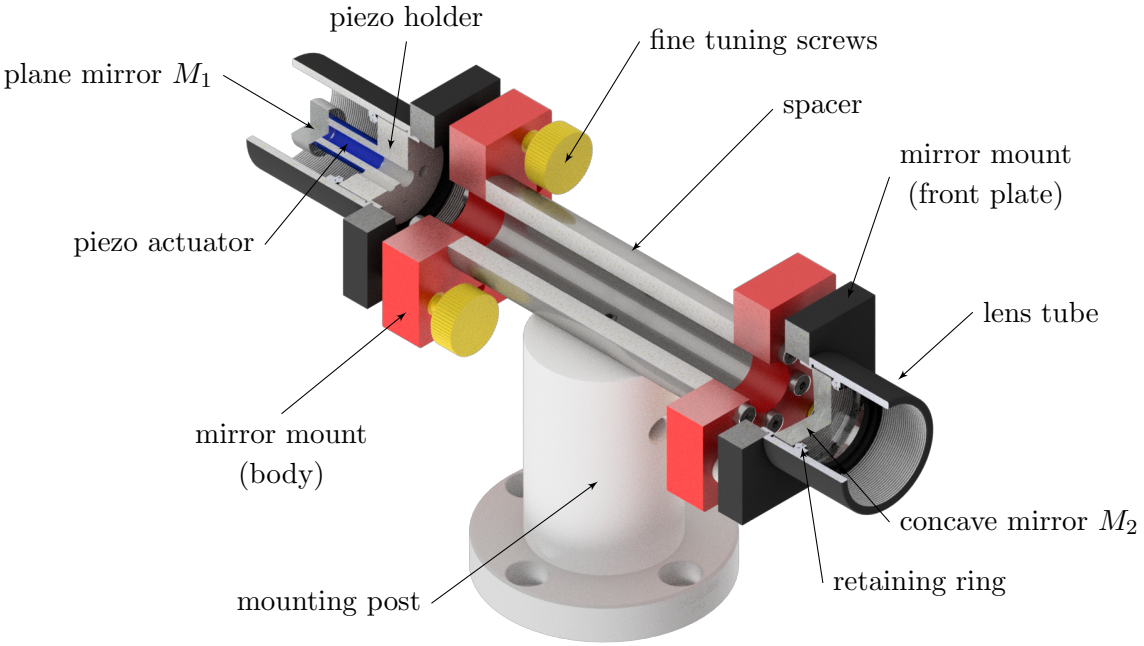

Fig. 4.1: Quarter cut through a rendered image of the self-built transfer cavity. The individual parts of the cavity are labelled within the figure.

4.2 Design and realization

The cavity, as depicted in Fig. 4.1, is designed in a plano-concave configuration of two commercially available mirrors. The plane mirror M_1 is a broadband laser mirror by Lens-Optics[12] with a diameter of 12.5 mm to cope with both laser wavelengths. It is made of a BK7 glass substrate and has a nominal reflectivity $\mathcal{R}_1 > 99.6\,\%$ in the range of 760 to 1064 nm due to the high reflectivity coating. The curvature of this mirror is $R_1 = \infty$. Mirror M_2 is a dielectric-coated concave mirror by Thorlabs[13] with a diameter of 25.4 mm and a focal length $f_2 = 100\,\text{mm}$. It has a curvature of $R_2 = -2f_2 = -200\,\text{mm}$. The average reflectivity over the whole coating range from 750 to 1100 nm is specified as $\mathcal{R}_2 > 99.0\,\%$.

The stability parameters of the two mirrors according to Eqn. (2.25) are $g_1 = 1$ and $g_2 = 0.2$, respectively. Therefore, the cavity is considered stable, as the inequality from Eqn. (2.24)

$$0 \leq g_1 g_2 = 0.2 \leq 1 \tag{4.1}$$

is fulfilled. A cavity with one mirror of curvature $R_1 = \infty$ is considered a special case of a spherical resonator [69]. Hence, all theoretical studies from Sec. 2.3 are applicable to the cavity at hand.

[12] Lens-Optics M760-1064/12.5 with HR760-1064 nm/0-45°, s+p-Pol. coating
[13] Thorlabs CM254-100-E03-SP (backside polished)

The concave mirror is mounted inside a lens tube[14] and fastened with a retaining ring. On the opposite side of the cavity, the plane mirror is glued onto a piezo ring actuator with epoxy resin. The piezo actuator itself is glued to a custom-made stainless steel piezo holder that comprises feed-throughs and a strain relief for the piezo cables. The whole assembly is built into another lens tube[15] and fixed in place with a retaining ring.

The front plates of two commercially available mirror mounts[16] are provided with threads[17] and the previously mentioned lens tubes are screwed into them. Both mirror mount bodies are provided with one through bore each, matching the inner diameter of the spacer tube. The two aluminium mirror mounts are screwed to a stainless steel tube[18] with an inner diameter of 13 mm and an outer diameter of 25 mm that serves as a spacer between the mirrors. In its center, the spacer is screwed onto a stainless steel mounting post[19]. Technical drawings of the parts are provided in appendix A.5.

The piezo actuator used in the cavity is a multilayer stack ring actuator[20] with six stacks and a nominal travel range of 11 µm. It can be operated in a voltage range from −20 to 100 V.

There are numerous advantages of this cavity design. The tilting of both mirrors with respect to the optical axis of the laser beam inside the cavity can be adjusted using the fine tuning screws on the mirror mounts. Moreover, by inserting additional retaining rings into the lens tubes, the longitudinal position of both the concave and the plane mirror can be altered and the free spectral range of the cavity can be modified. Moreover, the lens tubes containing the mirros can easily be dismantled. This proves to be useful for a rough adjustment of the laser beam through the cavity. More details on adjusting the cavity are given in appendix A.4. Furthermore, as the concave mirror is not glued into the cavity as in previous designs of the institute, it can simply be replaced by another mirror making it possible to alter properties such as the finesse of the cavity.

The presented design proves to be quite stable and the length of the cavity can actively be stabilized for over 24 hours. Apart from the spacer, all cavity parts are commerically available, which cuts production costs.

Moreover, several transfer cavities of the very design explained in this thesis are already recreated within the institute. Due to the arbitrarily adaptable components of the cavity and the modular design, a wide range of different properties can be achieved.

[14] Thorlabs SM1L10
[15] Thorlabs SM1L15
[16] Radiant Dyes MDI-2G-3000
[17] Done by the mechanics workshop of the Physics Institutes of the University of Stuttgart
[18] MiSUMi PIPS25-6-500
[19] turned down Thorlabs P75/M
[20] PI ceramic P-080.341

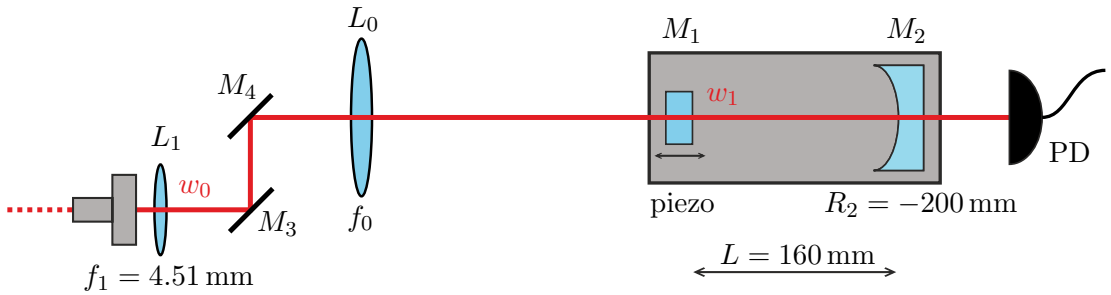

Fig. 4.2: Simplified schematic depiction of the optics around the transfer cavity with mirrors $M_{3,4}$ and lenses $L_{0,1}$. Inside the cavity, mirror M_1 is a plane mirror. The concave mirror M_2 has a curvature $R_2 = -200\,\mathrm{mm}$. The length of the cavity enclosed by the two mirrors is $L = 160\,\mathrm{mm}$. After the collimation lens L_1 with $f_1 = 4.51\,\mathrm{mm}$ the beam has a waist $w_0 = 430\,\mu\mathrm{m}$, the minimum waist on the plane mirror is $w_1 = 147\,\mu\mathrm{m}$ for $\lambda = 780\,\mathrm{nm}$. The focal length of lens L_0 is calculated to be $f_0 \approx 250\,\mathrm{mm}$. The transmission spectrum is measured with a photo diode (PD)

4.3 Mode-matching

In this section, the mode-matching of the incident laser beam and the cavity will be discussed in appropriate detail. Fundamental aspects have already been outlined in Sec. 2.3.3. To guarantee the best mode-matching of the cavity and incident laser beams, Eqn. (2.30) needs to be considered. The optical setup in front of the cavity is depicted in Fig. 4.2. After the polarization-maintaining optical fiber[21] with a mode field diameter of $2w_{\mathrm{MDF}} \approx 5\,\mu\mathrm{m}$, a lens L_1 with a focal length of $f_1 = 4.51\,\mathrm{mm}$ collimates the outcoupled laser beam. For a wavelength of $\lambda = 780\,\mathrm{nm}$, the collimated beam has a waist of $w_0 = 430\,\mu\mathrm{m}$. Two mirrors M_3 and M_4 are used to align the laser beam through the cavity. The position and the focal length f_0 of the second lens L_0 needs to be calculated in a way that the mode-matching conditions in Eqn. (2.30) are kept.

As a consequence of Eqn. (2.30), the curvature of the laser beam at the plane mirror needs to be infinitely large. This is the case if the minimum waist w_1 of the incident beam is at the position of the plane mirror M_1 at $z_1 = 0$. The concave mirror M_2 with a focal length $f_2 = 100\,\mathrm{mm}$ and a curvature $R_2 = -f_2/2 = -200\,\mathrm{mm}$ is at position $z_2 = z_1 + L = 160\,\mathrm{mm}$. Therefore, it is

$$R_2(L) = L + \frac{z_\mathrm{R}^2}{L}. \tag{4.2}$$

Inserting the Rayleigh length z_R from Eqn. (2.28) and solving for the waist w_1, one obtains

$$w_1 = \sqrt{\lambda/\pi\sqrt{LR_2 - L^2}}. \tag{4.3}$$

As a result, a waist $w_1 = 147\,\mu\mathrm{m}$ for $\lambda = 780\,\mathrm{nm}$ is necessary to fulfill the mode-matching conditions for both mirrors simultaneously.

[21] Thorlabs P3-780PM-FC-1

To calculate the correct focal length f_0 that focusses the collimated laser beam to the above calculated waist, it is appropriate to consider the lens L_0 and the following free-space propagation in the ray transfer matrix formalism (see Ref. [74] for a detailed derivation). Here, the lens L_0 is placed such that the mirror M_1 at position $z_1 = 0$ is in the focus of the lens and the waist w_1 of the beam is minimal at this very position. In this situation, the complex beam parameter

$$\frac{1}{q(z)} = \frac{1}{R(z)} + i\frac{1}{z_\mathrm{R}} \tag{4.4}$$

of the Gaussian beam is given by

$$\frac{1}{q'} = \frac{-1/f_0 + 1/q}{f_0/q}. \tag{4.5}$$

Since $z_1 = 0$ and consequently $R_1 = \infty$, Eqn. (4.4) simplifies to $q = -iz_\mathrm{R}$. Plugging q into Eqn. (4.5) and separating real and imaginary part one obtains

$$\frac{1}{q'} = \frac{1}{f_0} + i\frac{z_\mathrm{R}}{f_0^2}. \tag{4.6}$$

Reconsidering Eqn. (4.4), it is straight forward to identify

$$z'_\mathrm{R} = \frac{f_0^2}{z_\mathrm{R}}. \tag{4.7}$$

The focal length f_0 is then given by

$$f_0 = \sqrt{z_\mathrm{R} z'_\mathrm{R}} \overset{(2.28)}{=} \pi\frac{w_0 w_1}{\lambda}, \tag{4.8}$$

where z_R and z'_R are the Rayleigh lengths in front of and after the lens L_0, respectively. With the already calculated waists $w_0 = 430\,\mu\mathrm{m}$ and $w_1 = 147\,\mu\mathrm{m}$, the focal length of lens L_0 needs to be $f_0 \approx 254\,\mathrm{mm}$. Therfore, a lens with a focal legth of $f_0 = 250\,\mathrm{mm}$ is used in the experiment.

Similar calculations can be made for the second laser. As a matter of fact, the results for a wavelength of 1010 nm do not differ too much from the ones presented above for 780 nm. Hence, the mode-matching conditions for the photoionization laser are fulfilled with deviations below 10 %, if the mode-matching of the 780 nm laser is good and vice versa.

4.4 Characterization of the cavity

In this section, the transfer cavity will be characterized. To measure the free spectral range $\Delta\nu_\mathrm{FSR}$ and the finesse $\mathcal{F}$ of the self-built transfer cavity, the 780 nm laser is scanned over a range of around 10 GHz with a scan frequency of $\nu \approx 1\,\mathrm{Hz}$. The transmission spectrum of the cavity is measured with a photo diode.

Simultaneously, the same laser is used to perform Doppler-free saturation spectroscopy of the D_2-line of ^{87}Rb ($\lambda = 780.241\,\text{nm}$) in a vapor cell to calibrate a frequency reference for the measurements of the free spectral range of the cavity. The lamb dips of the transitions $|5S_{1/2}, F = 1\rangle \rightarrow |5P_{3/2}\rangle\,\text{CO}(F' = 1, 2)$ and $|5S_{1/2}, F = 2\rangle \rightarrow |5P_{3/2}, F' = 3\rangle$ are used to calibrate the frequency axis. The exact frequencies of said transitions are taken from Ref. [52]. CO denotes the cross-over resonance of two hyperfine states. A detailed description of the spectroscopy setup is given in Ref. [91]. Both the rubidium spectroscopy signal and the spectrum of the cavity are depicted in Fig. 4.3.

The free spectral range is determined by extracting the frequency differences of adjacent fundamental modes of the cavity (see Fig. 4.3). Due to non-linearities of the laser scan, individual free spectral ranges slightly differ from each other. Thus, the free spectral range is calculated as an average over all free spectral ranges. The measured and averaged value is

$$\Delta\nu_{\text{FSR}} = 928(65)\,\text{MHz}, \tag{4.9}$$

where the error is given by the standard deviation. Within tolerances, the free spectral range is quite close to the theoretical value of $\Delta\nu_{\text{FSR,theo}} = 937.5\,\text{MHz}$. The deviation of approximately 10 MHz corresponds to a 1.5 mm longer cavity and can be explained with mechanical tolerances of the cavity parts or the two layers of glue that stick both the plane mirror, the piezo actuator and the piezo holder together.

Pseudo-Voigt profiles

$$\mathcal{V}(\nu) = I_0 \cdot \left[\frac{\eta}{1 + \left(\frac{\nu - \nu_0}{\frac{1}{2}\nu_{\text{FWHM}}} \right)^2} + (1 - \eta) \cdot \exp\left[-\ln(2) \left(\frac{\nu - \nu_0}{\frac{1}{2}\nu_{\text{FWHM}}} \right)^2 \right] \right] + I_{\text{off}} \tag{4.10}$$

are fitted to the transfer cavity transmission maxima in Fig. 4.3 to obtain the full width at half maximum ν_{FWHM} of the individual transmission peaks for the 780 nm laser. A pseudo-Voigt fit accounts for both homogeneous and inhomogeneous broadening of the lines [82, 92]. In Eqn. (4.10) further fitting parameters are the amplitude I_0 of the transmission peaks, the center frequency ν_0 of a peak and an offset I_{off}. The balance of Lorentzian and Gaussian profile contributions in Eqn. (4.10) is determined by a weighting factor $\eta \in [0, 1]$.

The fitted values for ν_{FWHM} are averaged over all peaks and the mean value is

$$\nu_{\text{FWHM}} = 6.5(20)\,\text{MHz}. \tag{4.11}$$

According to Eqn. (2.23), the finesse of the cavity for 780 nm laser light is given by

$$\mathcal{F}_{780} = \frac{\Delta\nu_{\text{FSR}}}{\nu_{\text{FWHM}}} = 143(53), \tag{4.12}$$

where the error is determined with an error propagation.

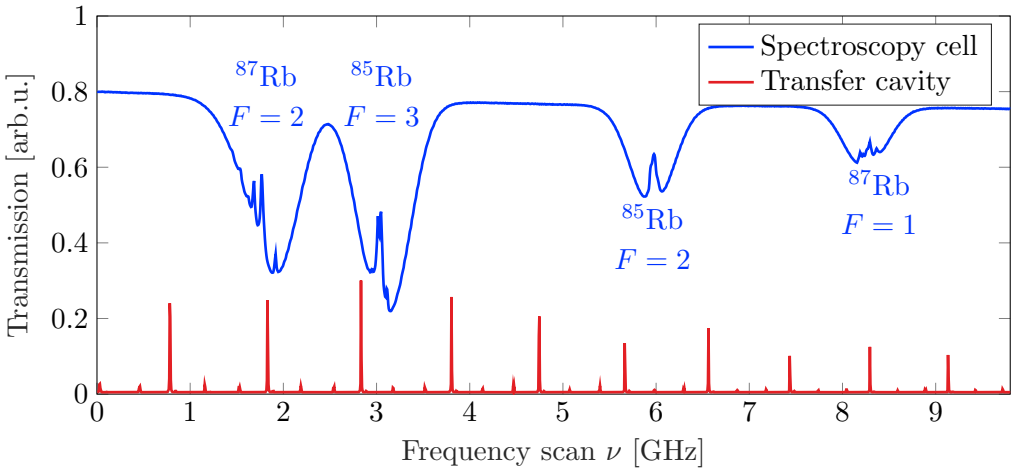

Fig. 4.3: Spectrum of the D_2-line of ^{87}Rb and transmission spectrum of the transfer cavity. The rubidium spectrum is acquired with Doppler-free saturation spectroscopy in a vapor cell. Contributions from the different hyperfine levels and the isotope ^{85}Rb are marked within the figure. The lamb dips of the atomic spectrum are used to calibrate a frequency standard to precisely measure the free spectral range of the transfer cavity. Over a scan range of 10 GHz ten transmission peaks can be seen. Between adjacent fundamental modes, Hermite-Gaussian modes with a negligible amplitude can be spotted. All data is taken over four averages and with a slow laser scan frequency of $\nu \approx 1$ Hz.

To also measure the finesse of the transfer cavity at 1010 nm, the photoionization laser is scanned at a similar scan frequency as the 780 nm laser and the spectrum of the cavity is measured with a photo diode. As the free spectral range of a resonator does not depend on the wavelength, the spectrum of the photoionization laser can be calibrated knowing $\Delta\nu_{\mathrm{FSR}}$ of the 780 nm laser. Afterwards, it is possible to also fit pseudo-Voigt profiles to the transmission peaks in the spectrum and obtain the average full width at half maximum of the cavity peaks. Eventually, this yields a finesse of

$$\mathcal{F}_{1010} = 371(41) \tag{4.13}$$

for the 1010 nm photoionization wavelength, which is higher than the finesse at 780 nm. This is due to the higher reflectivity of the cavity mirrors at infrared wavelengths compared to 780 nm.

Compared to the theoretical value of $\mathcal{F}_{\mathrm{theo}} > 447$ that is calculated with the minimal reflectivities $\mathcal{R}_{1,2}$ of the cavity mirrors, the finesse at both wavelengths is much smaller.

The deviation of the measured value compared to the theoretical calculations might arise from two different situations. In the process of gluing the plane mirror onto the piezo, epoxy resin particles could have outgased and sedimented down on the mirror, marginally reducing its reflectivity by roughly 1 to 1.5 %. The other reason could be an inaccurate mode-matching of the cavity and laser beam or slight misalignments in the whole transfer cavity setup.

4.4.1 Influence of the concave mirror

In a further analysis, the concave mirror of the cavity will be examined. Investigations have shown that especially the transmission of the concave mirror at 1010 nm is quite small compared to 780 nm. A batch of 13 concave mirrors of the same Thorlabs CM254-100-E03-SP (backside polished) product line are measured with respect to their individual transmission. The mean transmission is on the order of $\mathcal{T} \approx 10^{-5}\,\%$ at 0° incident light. Only one of the available mirrors has a much higher transmission of $\mathcal{T}_{1010} = 0.02\,\%$ at 1010 nm and $\mathcal{T}_{780} = 0.28\,\%$ at 780 nm and is used in the transfer cavity to allow for an applicable signal to noise ratio of the cavity transmission peaks of the photoionization laser.

To compensate for the ten times smaller transmission signal of the photoionization laser through the cavity compared to the 780 nm laser, the signal from the photo diode of the 1010 nm laser needs a pre-amplification by at least a factor of ten before it can be processed further.

Furthermore, an additional custom-made concave mirror has been created. A 60 nm layer of silver (Ag) was evaporated onto a BK7 glass sample followed by a 10 nm protective layer of magnesium flouride (MgF_2)[22]. The transmission of the silver mirror is measured to $\mathcal{T}_{1010} = 2.8\,\%$ and $\mathcal{T}_{780} = 3.9\,\%$, respectively. However, this mirror yields a much smaller finesse of the transfer cavity with $\mathcal{F}_{780} = 62(5)$ and $\mathcal{F}_{1010} = 116(8)$. As for the small finesse, the mirror is only used as a backup. Thanks to the modular design of the cavity, the concave mirror can be replaced at any time if a higher transmission is needed.

4.4.2 Degenerate transfer cavity

At first, a cavity with a length of 150 mm has been set up to realize a free spectral range of $\Delta\nu_{\mathrm{FSR}} = 1\,\mathrm{GHz}$. However, this length of the transfer cavity has led to the degeneracy of fundamental Gaussian modes and higher order Hermite-Gaussian modes.

With the optical properties of the setup as described in Sec. 4.3, especially with a waist of $w_1 = 147\,\mu\mathrm{m}$ at $z_1 = 0$, the resonance frequencies of the cavity according to Eqn. (2.31) and (2.32) have been

$$\begin{aligned}
\nu_{q,l,m} &= q\Delta\nu_{\mathrm{FSR}} + (l+m+1)\,\frac{1}{\pi}\left[\arctan\left(\frac{z_2}{z_\mathrm{R}}\right) - \arctan\left(\frac{z_1}{z_\mathrm{R}}\right)\right]\Delta\nu_{\mathrm{FSR}} \\
&= q\Delta\nu_{\mathrm{FSR}} + (l+m+1)\,\frac{1}{\pi}\left[\arctan\left(\frac{\lambda L}{\pi w_1^2}\right)\right]\Delta\nu_{\mathrm{FSR}} \\
&\approx \left(q + \frac{l+m+1}{3}\right)\Delta\nu_{\mathrm{FSR}}.
\end{aligned} \tag{4.14}$$

[22] Produced at the 1. Physics Institute at the University of Stuttgart

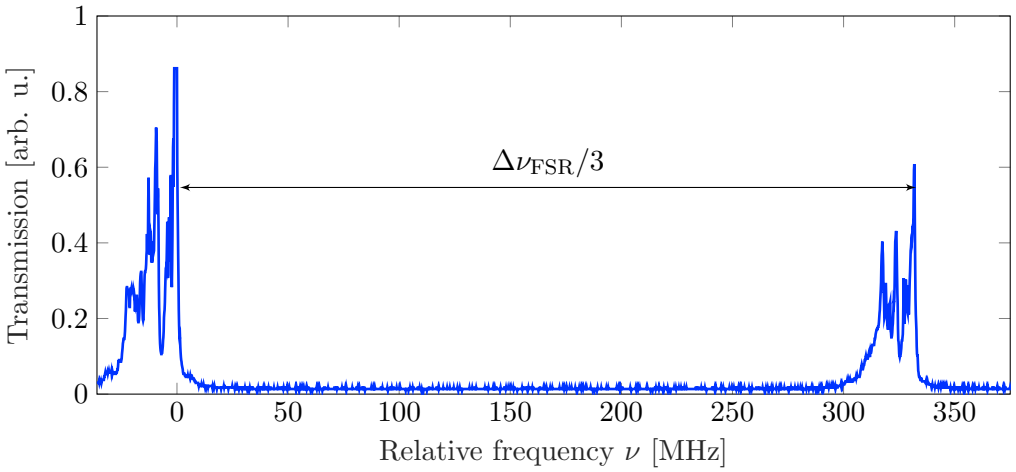

Fig. 4.4: Resonance frequencies of a degenerate cavity. The plot shows a section of roughly a third of a free spectral range with the Gaussian fundamental mode at $\nu = 0\,\mathrm{MHz}$. In the nearly degenerate spectrum, individual modes have been pushed apart for $\Delta\nu \approx 6\,\mathrm{MHz}$ by deliberately misaligning the cavity. Since locking the cavity has not been feasible, a 10 mm longer cavity has been built, lifting the degeneracy.

Transmitted Hermite-Gaussian modes with $l + m = 2$ have been detected with a CCD camera behind the transfer cavity. It can easily be calculated that the spacing $\Delta\nu$ of two modes in the cavity has been quite small. For instance, it has been

$$\Delta\nu = 2\Delta\nu_{\mathrm{FSR}} - \nu_{1,2,0} \approx 2\,\mathrm{MHz}. \tag{4.15}$$

The resonance frequency profile of this practically degenerate cavity is depicted in Fig. 4.4. As a consequence of the degeneracy, it has not been possible to lock the cavity and the length of the spacer has been increased by 10 mm to lift the degeneracy. The associated decrease in the free spectral range has no practical consequences for the use of the cavity.

4.5 Frequency and length stabilization of the lasers and the cavity

To perform a transfer lock from the 780 nm laser to the 1010 nm laser, three steps are required. Firstly, the 780 nm laser needs to be locked. Secondly the length of the transfer cavity needs to be stabilized using the locked 780 nm laser. Thirdly, the 1010 nm laser is locked to the cavity. In this section, the respective locking schemes of the two lasers and the cavity will be presented and the necessary electronic devices as well as the electronic circuits will be explained. Fig. 4.5 gives a schematic overview of the different feedback loops.

As a first step, the 780 nm Toptica DLpro laser is locked to a ULE cavity using the Pound-Drever-Hall technique [81, 93] (see red box in Fig. 4.5). The specific procedures to perform the frequency stabilization as well as the corresponding optical setup are described in Ref. [91]. Here, only a short summary is given. The 780 nm laser is scanned with a Toptica SC 110 module and the spectrum of the ULE is detected by a photo diode and fed to the Toptica Pound-Drever-Hall module PDD 110, where an error signal is produced. The error signal is sent to the FALC 110 module, which comprises a PID modul to produce a feedback signal. This signal is processed by the 780 nm laser and the feedback loop is closed.

Once the 780 nm laser is locked, it is possible to stabilize the cavity at a constant length. The key element in this stabilization circuit (blue box in Fig. 4.5) is a self-built PID controller[23]. The PID controller has two input connections, one for the signal from the photo diode and another for an external scan module. The two outputs provide a monitor signal of the input and an error signal as processed by the PID controller. A scan module[24] provides a triangular signal at a frequency $\nu_{\mathrm{Ramp}} = 1.5\,\mathrm{Hz}$. The voltage of the scan ramp can be guided through the PID to scan the cavity over multiple free spectral ranges. As the output voltage of the PID is dimensioned to a range from 0 V to 3.3 V, the signal is amplified by a piezo controller[25] that delivers a tenfold voltage gain. Right in front of the piezo actuator a 15 kHz low-pass filter can be installed to cut off high frequency noise that would otherwise give rise to instabilities within the feedback loop. A photo diode detects the transmission peaks of the cavity and is connected to a grounded 1 MΩ resistor to provide the PID controller with a sufficient photo voltage. To lock the cavity, a so-called side-lock is performed. For that, the input signal of the photo diode is shifted with an error offset voltage at the PID such that the slope of the transmission peak has a zero-crossing roughly at half of its maximum. Fig. 4.6 shows a zoom into one transmission peak and the point on which the cavity is locked. The PID adjusts the length of the cavity such that the error signal stays at the marked zero crossing in the figure.

Having successfully locked both the 780 nm laser and the transfer cavity, the frequency stabilization of the 1010 nm laser is next. The related schematics are depicted in the yellow box in Fig. 4.5. The amplitude of the Toptica scan control SC110 is set to zero. The trigger output of the SC110 module can be used as a modulation input (compare Ref. [94]). This

[23] The properties and the circuit of the PID can be found in appendix A.2
[24] Electronics Lab, Physical Insitute, University of Stuttgart: Scan control Elab 26/08
[25] PI E-610.00

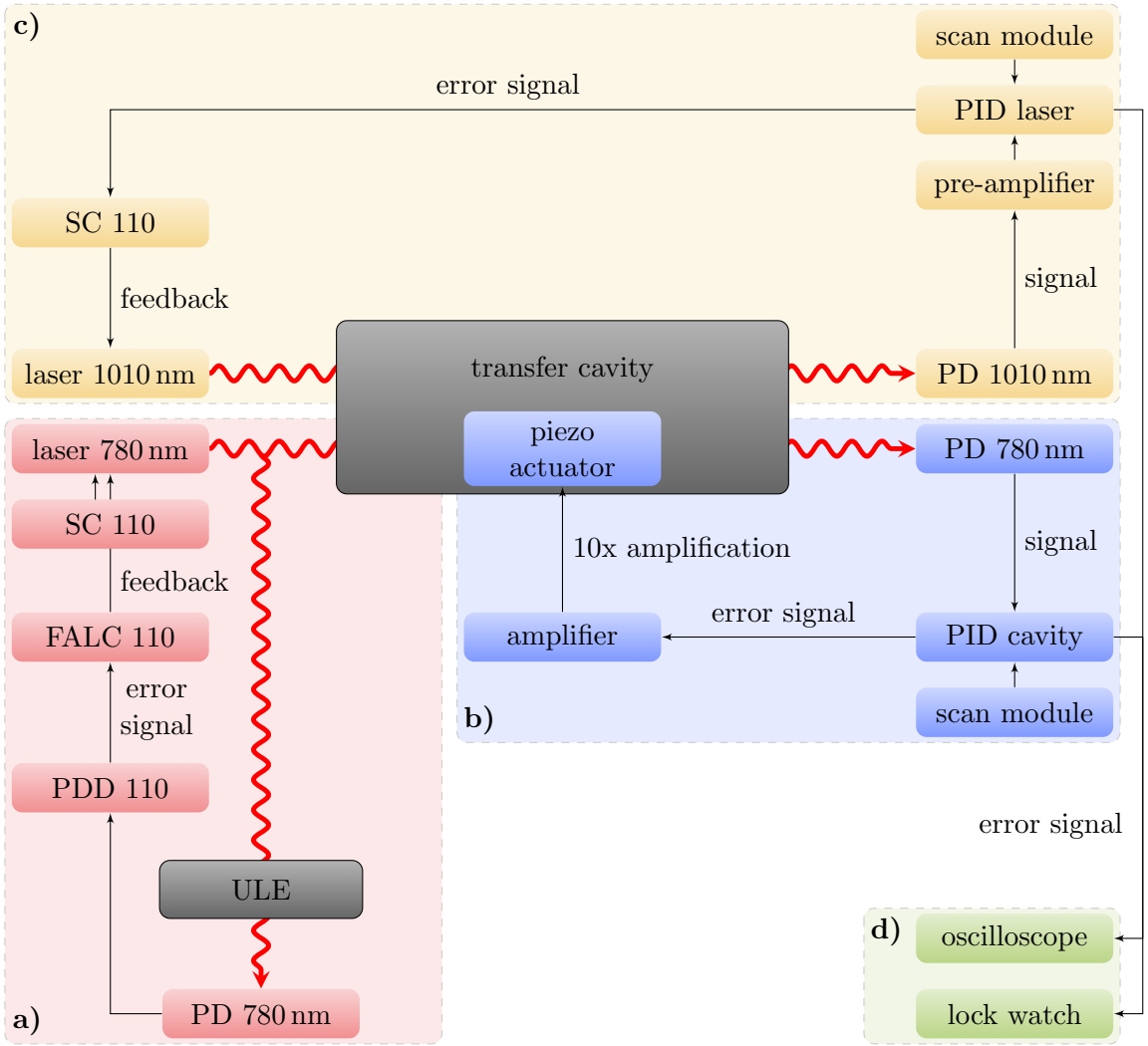

Fig. 4.5: Schematic chart of the transfer cavity and laser locking electronics. Different color boxes indicate different locking loops. **a)** Frequency stabilization of the 780 nm laser (red box): A ULE cavity is used to provide an absolute frequency reference for the 780 nm DLpro laser. The laser is scanned with a Toptica SC 110 module and the spectrum of the cavity is detected with a photo diode (PD). Using the Pound-Drever-Hall technique, an error signal is generated at the PDD 110 module and fed back to the laser via the FALC 110 module. **b)** Length stabilization of the transfer cavity (blue box): The length of the cavity is variied periodically with a triangular ramp voltage provided by the scan module. By the periodical enlargement and contraction of the piezo actuator, the length of the cavity is altered. The transmission peaks of the locked 780 nm laser are detected with a photo diode. A PID controller creates an error signal using the so-called side-lock technique. Before the output signal of the PID is forwarded to the piezo it is amplified by a factor of ten. **c)** Frequency stabilization of the 1010 nm laser (yellow box): The scan amplitude of the SC110 module is set to zero. The laser is scanned with a triangular voltage from the scan module. The transmitted light of the 1010 nm laser though the cavity is detected by a photo diode and pre-amplified due to the small signal height. The pre-amplifier signal is fed to the PID where an error signal is generated using the side-lock technique. Using an external input of the SC 110, the error signal is fed back to the 1010 nm laser closing the feedback loop. **d)** The PID error signals are monitored on oscilloscopes and a lock watch monitores the lock of the cavity and the photoionization laser.

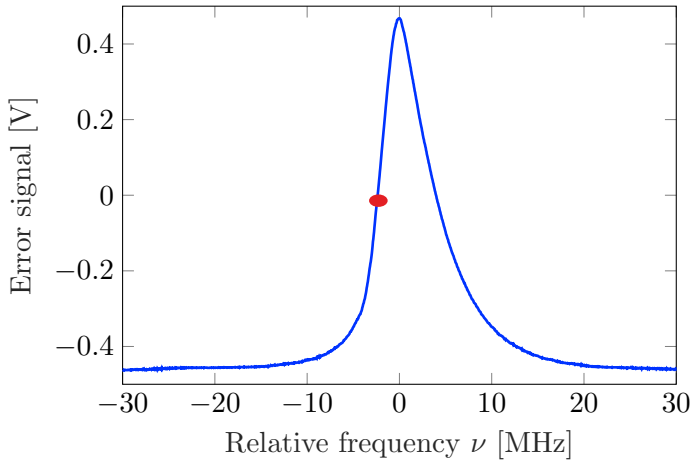

Fig. 4.6: Visualization of the so-called side-lock technique. The cavity transmission spectrum is shifted with an error offset voltage such that the slope of a transmission peak has a zero-crossing. The circle in the figure indicates the locking point at zero error signal. A PID controller regulates the length of the cavity or the frequency of the 1010 nm laser such that the error signal remains at its zero-crossing value.

solution is adopted to feed the error signal from the PID to the 1010 nm laser. The DLpro is scanned via the Elab 26/08 scan module and the cavity transmission peaks are detected by a photo diode provided with a 1 MΩ resistor. Due to the small transmission of the concave mirror at 1010 nm, the transmission signal is quite small and an additional pre-amplifier[26] is used to provide a 20 times higher signal for the PID controller. As with the cavity, a side-lock is performed to gain an error signal for the laser. The offset of the SC110 module can be used to chose the desired wavelength for the photoionization laser.

The monitor outputs of both PID controllers are connected to an oscilloscope to watch the transmission through the cavity and to control the respective locking processes. The signals are further monitored with lock watches, which provide optical feedback for the user and a TTL signal for the computer control if the cavity or laser is out of lock.

[26] Stanford Research Systems model SR560 low-noise pre-amplifier

5 Photoionization simulations

The photoionization scheme considered in this thesis is examined both in the experiment and in numerical simulations. Within this chapter, the photoionization simulations will be presented and some results are shown.

In the first section, the V-type photoionization scheme presented in Sec. 3.1 and the already developed theoretical treatment of a three-level system in Sec. 2.2.4 will be adapted and substantiated to lay a basis for the photoionization simulations. The fundamental concepts of this simulations will be demonstrated.

After the conceptual introduction into the photoionization simulations in the first section, the second section will present results from an exemplary simulation for the V-type photoionization of the $|40S_{1/2}\rangle$ Rydberg state. In the third section of this chapter, the inclusion of pulse shape effects originating from the rise and fall times of the AOMs used for switching the lasers will be discussed.

5.1 Photoionization simulation concepts

In this section, the concept of the V-type photoionization simulation of a rubidium Rydberg atom will be presented. A reconsideration of the Rydberg excitation and photoionization scheme from Fig. 3.1 shows that four levels in total have to be dealt with. For practical reasons, an additional notation of the respective states is used. The $|5S_{1/2}\rangle$ state is also referred to as the ground state $|g\rangle$, $|e\rangle$ denotes the excited $|6P_{3/2}\rangle$ state. The notation $|r\rangle$ will complement the $|nS_{1/2}\rangle$ Rydberg state and $|c\rangle$ is the continuum.

To obtain the time-dependent evolution of this four-level system, the Liouville-von-Neumann equation (2.9) needs to be solved. Since the ground state $|g\rangle$ is not adressed by any laser being used for the photoionization, it is neglected at first. Therefore, the photoionization process can be considered an effective V-type three-level system as presented in Sec. 2.2.4 and the Hamiltonian $\mathcal{H}_{\mathrm{AL}}$ as well as the Lindblad operator $\mathcal{L}(\rho)$ derived there can be used. Still, decays into the ground state cannot be neglected completely and will be reintroduced later.

For the following calculations, a couple of assumptions and simplifications are made and hence both operators $\mathcal{H}_{\mathrm{AL}}$ and $\mathcal{L}(\rho)$ need to be modified for the simulations at hand:

1. There are no Rabi oscillations between the excited state $|e\rangle$ and the continuum $|c\rangle$. This is comprehensible as the electron of the photoionized atom is not bound any longer. As a consequence, the contributions from $\Omega_{23}^{(*)} = \Omega_{ec}^{(*)}$ in $\mathcal{H}_{\mathrm{AL}}$ vanish. As discussed later, the transition into the continuum is treated as a decay.

2. The Rydberg state $|r\rangle$ is chosen to be the start state of the simulation and its energy $\mathcal{E}_r$ is set to zero for this purpose. Moreover, $\Delta_{23} = \Delta_{ec}$ is set to zero, too, as it is not reasonable to define a detuning for transitions from the excited state $|e\rangle$ into the continuum.

This yields a new atom-light interaction Hamiltonian

$$\mathcal{H}_{\mathrm{AL}} = \hbar \begin{pmatrix} 0 & \frac{1}{2}\Omega_{re} & 0 \\ \frac{1}{2}\Omega_{re}^{*} & -\Delta_{re} & 0 \\ 0 & 0 & 0 \end{pmatrix} \tag{5.1}$$

for the simulations, whose only contributions arise from the coherent coupling between the Rydberg state and the excited state as well as from the detuning of the laser that drives said transition.

3. With the same argument as before, the continuum does not decay into any level, leading to $\Gamma_{31} = 0$ as well as the elimination of all matrix elements involving $\rho_{23}^{(*)} = \rho_{ec}^{(*)}$ in $\mathcal{L}(\rho)$.

4. The Rydberg state has a comperatively long lifetime [4]. On the timescale, on which the experiment takes place, the decay of the Rydberg state can be neglected. Accordingly, $\Gamma_{12}\rho_{22} = \Gamma_{re}\rho_{ee}$ is set to zero.

5. The photoionization transition $|e\rangle \to |c\rangle$ is treated as a laser-induced decay with

$$\Gamma_{ec} = \frac{\sigma \lambda_{ec} I_{ec}}{hc}, \tag{5.2}$$

where λ_{ec} is the wavelength of the photoionization laser, σ is the photoionization cross section of this transition and I_{ec} the photoionization laser intensity [88, 95, 96]. For the ionization processes studied in this thesis, the photoionization cross section is on the order of several Mb $= 10^{-22}\,\mathrm{m}^2$.

Finally, the modified Lindblad operator can be identified as

$$\mathcal{L}(\rho) = \begin{pmatrix} 0 & -\frac{1}{2}\Gamma\rho_{re} & 0 \\ -\frac{1}{2}\Gamma\rho_{er} & -\Gamma\rho_{ee} & 0 \\ 0 & 0 & \Gamma\rho_{ee} \end{pmatrix}, \tag{5.3}$$

where all remaining decays are bundled together in Γ. At this point it is reasonable to reconsider the so far neglected decays into the ground state by decomposing $\Gamma = \Gamma_{ec} + \Gamma_{eg}$ into one contribution Γ_{eg} of decay from $|e\rangle$ to $|g\rangle$ and another Γ_{ec} from $|e\rangle$ to $|c\rangle$. In the

Lindblad operator in Eqn. (5.3), the off-diagonal elements represent the decay of coherence between $|r\rangle$ and $|e\rangle$ and the diagonal element $-\Gamma\rho_{ee}$ describes the decay of the population from the excited state into both the continuum and the ground state. The fraction N_c of population that decays only into the continuum can simply be calculated with

$$N_c = \frac{\Gamma_{ec}}{\Gamma_{ec} + \Gamma_{eg}}. \tag{5.4}$$

Analogously, the branching ratio $N_g = \Gamma_{eg}/(\Gamma_{ec} + \Gamma_{eg})$ gives the population in the ground state. The constant decay rate from the $|6P_{3/2}\rangle$ state into the ground state is determined by the life time $\tau_{6P_{3/2}} = 112\,\text{ns}$ of the excited state and is given by $\Gamma_{eg} = 2\pi \times 1.42\,\text{MHz}$ [83].

The Liouville-von-Neumann equation (2.9) is solved using the Hamiltonian from Eqn. (5.1) and the Lindblad operator from Eqn. (5.3). The results are the optical Bloch equations

$$\begin{aligned}
\frac{\partial}{\partial t}\rho_{rr}(t) &= \frac{i\Omega_{re}}{2}\left(\rho_{re}(t) - \rho_{er}(t)\right), \\
\frac{\partial}{\partial t}\rho_{re}(t) &= -\left(i\Delta_{re} + \frac{\Gamma}{2}\right)\rho_{er}(t) + \frac{i\Omega_{re}}{2}\left(\rho_{rr}(t) - \rho_{ee}(t)\right), \\
\frac{\partial}{\partial t}\rho_{rc}(t) &= -\frac{i\Omega_{re}}{2}\rho_{ec}(t), \\
\frac{\partial}{\partial t}\rho_{er}(t) &= \left(i\Delta_{re} - \frac{\Gamma}{2}\right)\rho_{er}(t) - \frac{i\Omega_{re}}{2}\left(\rho_{rr}(t) - \rho_{ee}(t)\right), \\
\frac{\partial}{\partial t}\rho_{ee}(t) &= -\Gamma\rho_{ee}(t) - \frac{i\Omega_{re}}{2}\left(\rho_{re}(t) - \rho_{er}(t)\right), \\
\frac{\partial}{\partial t}\rho_{ec}(t) &= i\Delta_{re}\rho_{ec}(t) - \frac{i\Omega_{re}}{2}\rho_{rc}(t), \\
\frac{\partial}{\partial t}\rho_{cr}(t) &= \frac{i\Omega_{re}}{2}\rho_{ce}(t), \\
\frac{\partial}{\partial t}\rho_{ce}(t) &= -i\Delta_{re}\rho_{ce}(t) + \frac{i\Omega_{re}}{2}\rho_{cr}(t), \\
\frac{\partial}{\partial t}\rho_{cc}(t) &= \Gamma\rho_{ee}(t).
\end{aligned} \tag{5.5}$$

The Rabi frequency Ω_{re} is given by

$$\Omega_{re} = \frac{\mu_{re}E_{re}}{\hbar}, \tag{5.6}$$

with the dipole matrix element $\mu_{re} = \langle r|d|e\rangle$ and the electric field component

$$E_{re} = \sqrt{\frac{2P_{re}}{c\epsilon_0\pi w_{re}^2}} \tag{5.7}$$

of the Rydberg deexcitation laser in the direction of the dipole moment. Here, P_{re} is the power of the Rydberg deexcitation laser and w_{re} is its waist. The mean intensity I_{ec} of the photoionization laser is given by

$$I_{ec} = \frac{P_{ec}}{\pi w_{ec}^2}. \tag{5.8}$$

Tab. 5.1: Simulation parameters for the cw photoionization simulation. The parameters are chosen such that they reflect typical experimental conditions, which leads to a photoionization time of $t_{\mathrm{PI}} = 17\,\mathrm{ns}$. The corresponding plot is shown in Fig. 5.1.

Parameter	Symbol	Numeric value	Comment
Rydberg state	$\|r\rangle$	$\|40S_{1/2}\rangle$	–
Deexcitation laser waist	w_{re}	$3.0\,\mu\mathrm{m}$	–
Deexcitation laser power	P_{re}	$1.4\,\mathrm{mW}$	–
Photoionization laser waist	w_{ec}	$3.0\,\mu\mathrm{m}$	–
Photoionization laser power	P_{ec}	$1000\,\mathrm{mW}$	–
Photoionization laser wavelength	λ_{ec}	$1010.000\,\mathrm{nm}$	cw
Intermediate detuning	Δ_{re}	$2\pi \times 0\,\mathrm{MHz}$	resonant case
Photoionization cross section	σ	$15 \times 10^{-22}\,\mathrm{m}^2$	taken from Ref. [97]

The dipole matrix element in Eqn. (5.6) depends on the overlap of the wavefunctions of the excited and the Rydberg state. Since the hyperfine structure of the $|6P_{3/2}\rangle$ excited state can be resolved with the lasers used in the experiment, a suitable basis is the $|F, m_F\rangle$ basis. This looks different for the Rydberg state, where the $|J, m_J\rangle$ basis is the most preferable basis. For the calculation of the dipole matrix element, Eqn. (A.5) is used. A detailed derivation is given in appendix A.1 and the radial matrix element is extracted from an institute-internal database. As outlined in Sec. 3.1, the transition $|r\rangle \rightarrow |e\rangle$ is adressed with σ^--polarized light of the 1020 nm laser. The optical Bloch equations (5.5) are solved with Matlab using an explicit Runge-Kutta method of fourth order.

5.2 Simulations of a V-type photoionization of the $|40S_{1/2}\rangle$ Rydberg state

The simulation parameters for an exemplary simulation starting in the $|40S_{1/2}\rangle$ Rydberg state are summarized in Tab. 5.1 and the simulation result is shown in Fig. 5.1. The Rabi frequency Ω_{re} of the Rydberg deexcitation is chosen such that the ionization time is as short as possible for a given decay rate Γ_{ec} into the continuum. For this and all further simulations, the photoionization time t_{PI} is defined as the period from switching on the Rydberg deexcitation laser until 90 % of the population reaches the continuum. Any dephasing mechanisms are neglected in all simulations if not mentioned otherwise.

The simulation result in Fig. 5.1 shows that a photoionization time of $t_{\mathrm{PI}} = 17\,\mathrm{ns}$ for the $|40S_{1/2}\rangle$ state can be reached assuming realistic experimental conditions. Here, the Rabi frequency of the Rydberg deexcitation laser is $\Omega_{re} = 2\pi \times 54.7\,\mathrm{MHz}$ and the decay rate into the continuum is $\Gamma_{ec} = 2\pi \times 42.9\,\mathrm{MHz}$.

Since $\Omega_{re} \sim 1/w_{re}$ and $I_{ec} \sim 1/w_{ec}^2$, the rather small beam waist in the focus of the deexcitation and the photoionization laser has a wide influence on the outcome of the photoionization

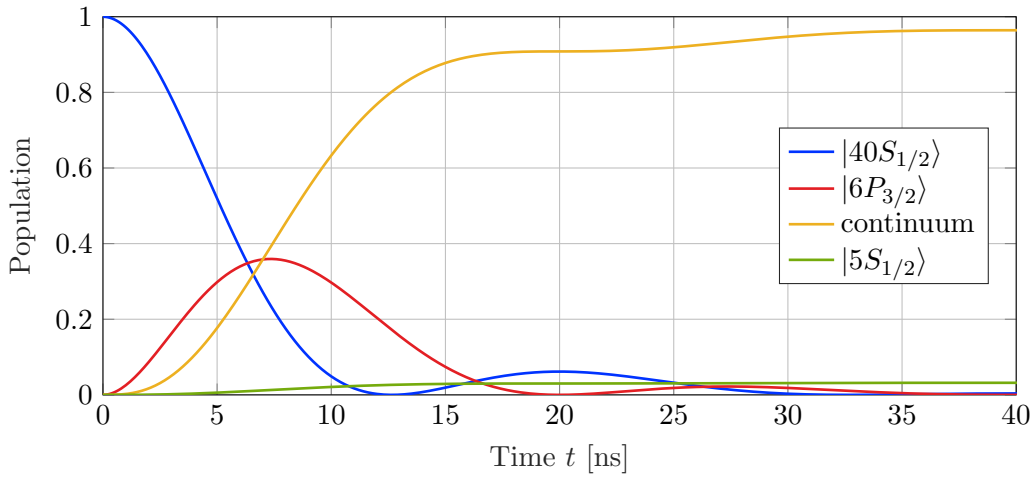

Fig. 5.1: Exemplary simulation of the V-type photoionization of a ^{87}Rb atom starting in the $|40S_{1/2}\rangle$ Rydberg state. With the parameters given in Tab. 5.1 a photoionization time of $t_{\mathrm{PI}} = 17\,\mathrm{ns}$ can be achieved.

time t_{PI}. Although the aspheric lens in front of the science chamber has a numerical aperture of NA ≈ 0.3, which translates to a minimum waist of $w_{\mathrm{min}} = \lambda/(\pi \cdot \mathrm{NA}) \approx 1\,\mu\mathrm{m}$ [74] for the infrared laser, a more conservative value of 3 µm for the waist of both beams is chosen for the exemplary simulation.

5.3 Consideration of the AOM rise and fall time

In the previous sections, the working principle of the photoionization simulation has been outlined and an exemplary simulation has been perfomed. Here, an extension of the simulation will be presented, which implements the rise times of the AOMs that switch the 1010 nm and 1020 nm laser on and off. The rise times of the AOMs currently used in the experiment are on the order of 50 ns and the correct pulse shape of the rising and falling edge is also accounted for in the simulation.

Performing a simulation with the exact same parameters as given in Sec. 5.2 and additionally considering the rise times of the AOMs leads to a prolonged photoionization time of $t_{\mathrm{PI}} = 41\,\mathrm{ns}$ for a photoionization starting in the $|40S_{1/2}\rangle$ Rydberg state. The time-dependent population of the involved atomic levels is illustrated in Fig. 5.2.

To reach a photoionization time as short as possible, the ratio Γ_{ec}/Ω_{er} of the laser-induced decay into the continuum and the Rabi frequency of the Rydberg deexcitation transition plays an important role. Fig. 5.3 depicts the dependence of the photoionization time as a function of said ratio. For a value of $\Gamma_{ec}/\Omega_{er} \approx 1.12$, the photoionization time for the specific set of parameters defined in Tab. 5.1 can be reduced to 37.6 ns. This requires a photoionization laser power of 1.5 W.

Yet, to reach photoionization times $t_{\mathrm{PI}} < 10\,\mathrm{ns}$, which is necessary for a diabatic photoionization process, more photoionization power and faster switching of the laser beams is required. The latter, for example, can be achieved using a Pockels cell.

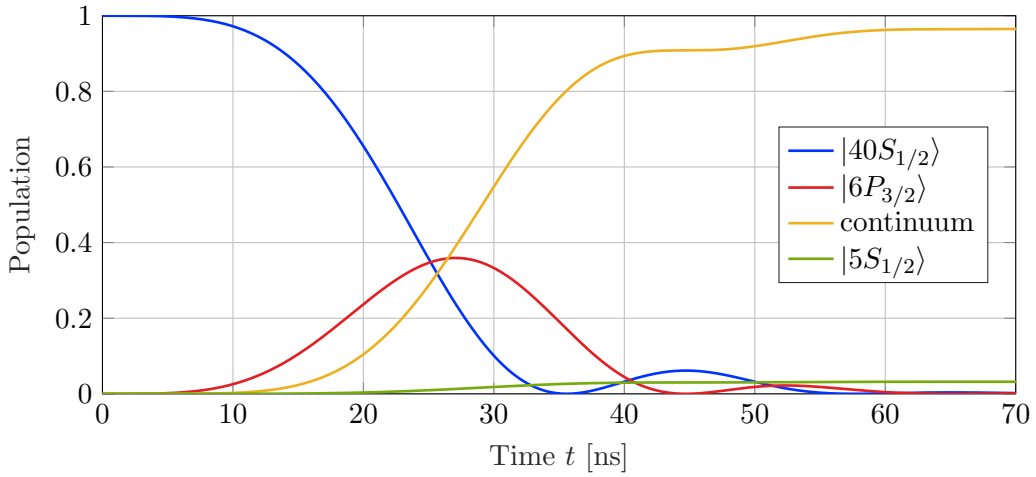

Fig. 5.2: Results for the simulation of a V-type photoionization scheme with the $|40S_{1/2}\rangle$ Rydberg state as a starting state. The parameters used are the same as in the simulation depicted in Fig. 5.1, only the rise times of the laser switching AOMs with around 50 ns are considered additionally, leading to a longer photoionization time of $t_{\mathrm{PI}} = 41\,\mathrm{ns}$. In the simulation, the Rabi frequency is $\Omega_{er} = 2\pi \times 54.7\,\mathrm{MHz}$, and the decay rate into the continuum is given by $\Gamma_{ce} = 2\pi \times 42.9\,\mathrm{MHz}$.

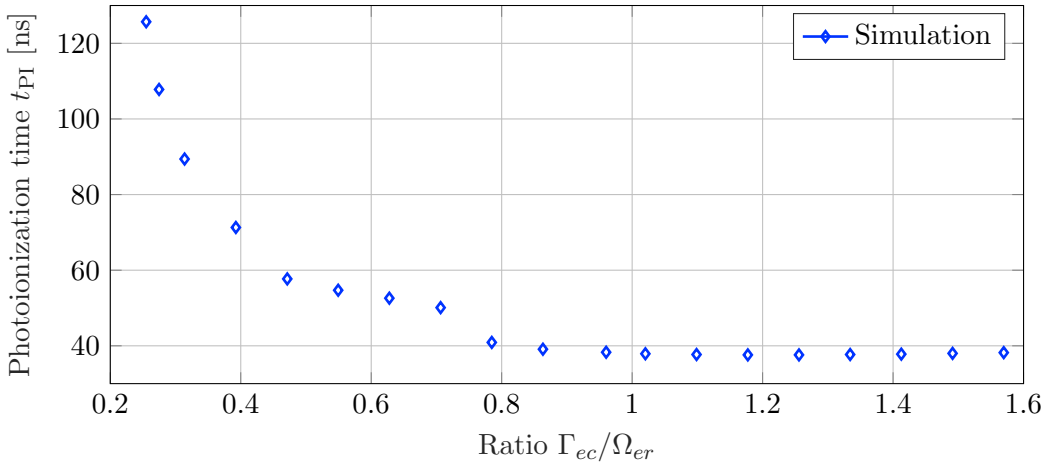

Fig. 5.3: Illustration of the photoionization time t_{PI} as a function of the ratio Γ_{ec}/Ω_{er} of the laser-induced decay into the continuum and the Rabi frequency of the Rydberg deexcitation transition. For a value of $\Gamma_{ec}/\Omega_{er} \approx 1.12$ the minimum photoionization time is $t_{\mathrm{PI}} = 37.6\,\mathrm{ns}$. In the simulation, the Rabi frequency of the Rydberg deexcitation laser is kept constant and has a value of $\Omega_{er} = 2\pi \times 54.7\,\mathrm{MHz}$.

6 Experimental results

In this chapter, the experiments performed with the photoionization laser system will be described and evaluated. All experiments have been performed in the lab of the Superatoms group at the institute, and all lasers except for the photoionization laser have been provided by them. The first section of this chapter will deal briefly with their experimental procedure and will outline some of the physical parameters that have been used within the experiment. Preparatory measurements of the photoionization efficiency as well as measurements of the Rabi frequency of the Rydberg deexcitation laser will be presented. Moreover, further simulations and measurements have been carried out to gain insight into the ac Stark shift of both the Rydberg state and the intermediate state. The preperative deliberations and measurements will be used to evaluate the photoionization cross section. A discussion of the experimental results will conclude the chapter.

In addition to the experiments and results presented in this chapter, the photoionization laser system has been used to observe the Rydberg blockade induced by a single ion [1].

6.1 Experimental procedure

The experimental setup of the Superatom experiment is described in Ref. [98]. In the presented measurements about 1.2×10^5 ground state, ^{87}Rb atoms are prepared in a thermal cloud within a crossed-beam optical dipole trap. The typical peak density of the cloud is on the order of $2.5 \times 10^{13}\,\mathrm{cm}^{-3}$ and the temperature of the sample is around 1 µK.

One single ground state atom is excited to the $|51S_{1/2}\rangle$ Rydberg state using an inverted scheme with a 420 nm and a 1015 nm laser (compare Sec. 3.1). This two-photon excitation is realized within a 500 ns long pulse, and the two lasers counter-propagate in order to reduce the Doppler broadening of atomic lines [82]. The intermediate detuning is set to $\Delta = 160\,\mathrm{MHz}$ and the 1015 nm Rydberg excitation laser has a waist of around 2 µm to control the spatial position of the Rydberg atom.

During a 200 ns long V-type photoionization pulse, the Rydberg atom gets deexcited with the 1015 nm laser to the $|6P_{3/2}\rangle$ intermediate state and the co-propagating photoionization laser with a wavelength $\lambda = 1010.186\,\mathrm{nm}$, and a waist $w = 2\,\mu\mathrm{m}$ produces a low-energy ion with an excess kinetic energy $\mathcal{E}_{\mathrm{ion}} = 0.84\,\mathrm{neV} = 9.7\,\mu\mathrm{K}$ above the ionization threshold of ^{87}Rb. A more detailed description of the Rydberg excitation and V-type photoionization scheme can be found in Sec. 3.1.

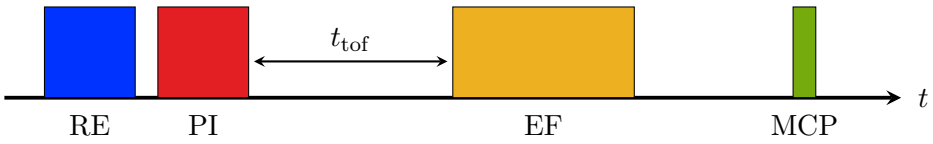

Fig. 6.1: Experimental pulse sequence for the measurement of the photoionization efficiency. A Rydberg atom gets excited to the $|51S_{1/2}\rangle$ state (RE) within a 500 ns pulse. Next to a short waiting period, a 200 ns long V-type photoionization pulse is applied (PI). After a time $t_{\mathrm{tof}} \approx 7\,\mu\mathrm{s}$, the produced ion is accelerated to the detector during a 5 µs long electric field pulse (EF). The detection of the ion takes place at the MCP. For the experiments in this thesis, this cycle is repeated 500 times within one thermal cloud. The timeline in the figure is not to scale.

After the photoionization, the generated ion propagates in the vicinity of the ionization region for some time of flight t_{tof}. An electric exctraction field of $E = 1.5\,\mathrm{V/cm}$ is applied for 5 µs to accelerate the ion towards a microchannel plate detector (MCP).

The experimental pulse sequence including the Rydberg excitation, the V-type photoionization, the electric field pulse and the detection on the MCP is summarized in Fig. 6.1. Usually, this sequence is repeated around 500 times in one thermal cloud in order to gain statistics.

To normalize the count rate of the MCP detector, only the Rydberg excitation pulse is carried out and an electric field of $E = 115\,\mathrm{V/cm}$ for the duration of 15 µs is employed to fieldionize the Rydberg atom. The count rate on the detector is divided by the amount of repetitions of the experimental cycle yielding a mean count rate of the MCP. This mean count rate incorporates any decay of the Rydberg state within the pulse sequence. Moreover, the mean count rate also includes the decay of the $|6P_{3/2}\rangle$ state that occurs during the Rydberg excitation. This normalization procedure allows to state a photoionization efficiency in the next section, without having to account for the aforementioned decays and the Rydberg excitation efficiency afterwards.

6.2 Measurement of the photoionization efficiency

In this section, the results of the photoionization efficiency measurement will be presented and briefly discussed. To later determine the photoionization cross section σ for the transition from the $|6P_{3/2}\rangle$ state into the continuum with the method presented in Sec. 6.7, a profound understanding of the laser power-dependent behavior of the photoionization rate is essential.

Fig. 6.1 depicts the pulse sequence for the measurement, which is performed in a thermal cloud with approximately 1.2×10^5 atoms. After the Rydberg excitation to the $|51S_{1/2}\rangle$ state, the subsequent V-type photoionization, and a time of flight $t_{\mathrm{tof}} = 7\,\mu\mathrm{s}$ of the ion, an

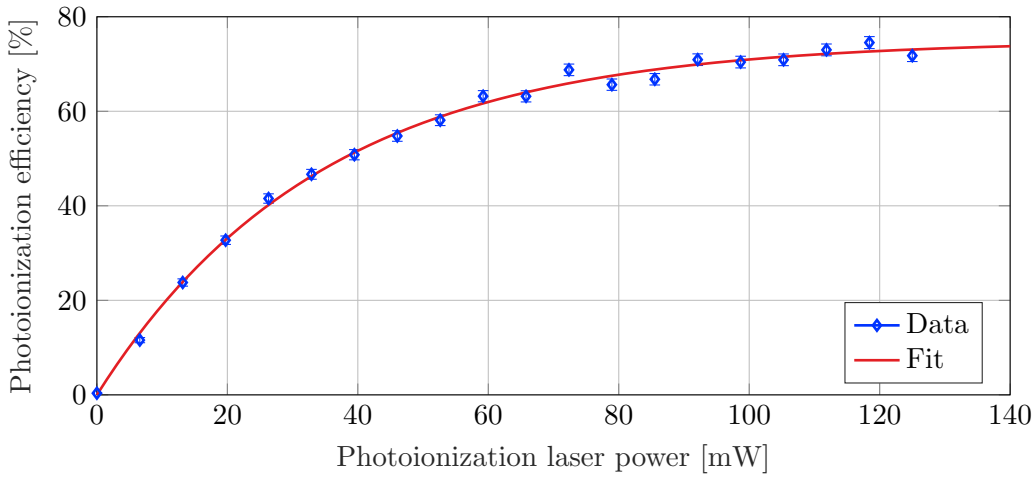

Fig. 6.2: Photoionization efficiency as a function of the laser power of the 1010.186 nm photoionization laser. For high powers the efficiency saturates at about 75 %. The error bars are given by the standard deviation of the mean ion count.

electric field ionization pulse accelerates the produced ions to the MPC to detect them. The described experimental cycle is repeated 500 times in each thermal cloud.

The photoionization efficiency is determined through the mean ion count on the detector divided by the mean count rate of the MCP (see Sec. 6.1 for the normalization of the MCP) and plotted as a function of the photoionization laser power in Fig. 6.2. The mean ion count for each power is an average value out of 25 experimental cycles. An exponential function is fitted to the obtained data indicating a saturation efficiency of 75.0(16) %.

The photoionization efficiency is limited by several factors such as the finite photoionization cross section σ, the shift of the $|6P_{3/2}\rangle$ intermediate state due to the ac Stark effect (see Sec. 2.2.5), the photoionization pulse length and laser power of the Rydberg deexcitation laser. Moreover, it is possible that the lasers used in the experiment couple to different substates of the $|6P_{3/2}\rangle$ level apart from the desired $F = 3, m_F = 3$ hyperfine substate due to some misalignments of the laser polarizations.

6.3 Rabi frequency measurement and waist determination

In order to determine the waist of the Rydberg deexcitation laser, the frequency Ω of the Rabi oscillations between the $|51S_{1/2}\rangle$ and the $|6P_{3/2}\rangle$ state are measured.

For this purpose, Rydberg atoms are excited with the previously outlined excitation scheme from Fig. 6.1. However, the photoionization laser is kept turned off. The pulse length of the PI segment is variable and equals the Rydberg deexcitation duration. The Rydberg atoms get deexcited by the 1015 nm laser with a power of $P = 2.2$ mW for a certain deexcitation

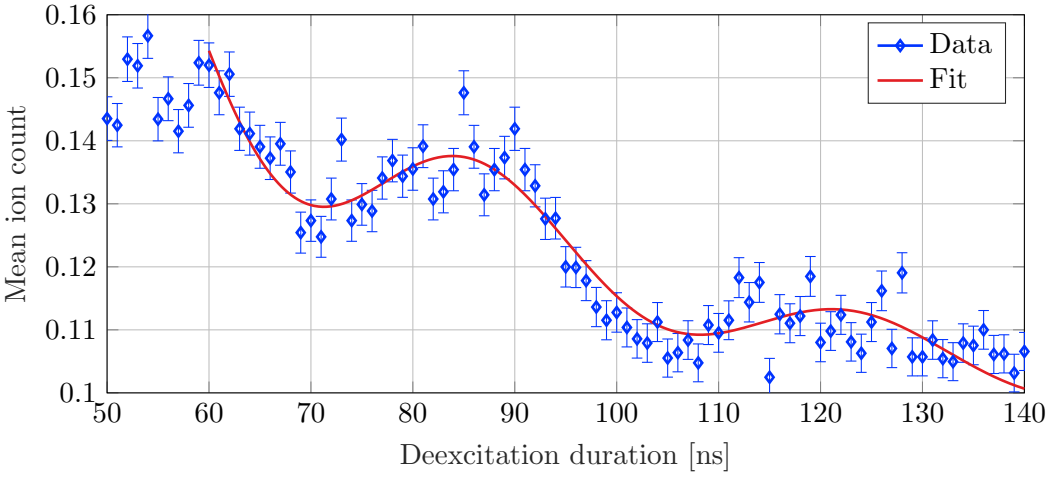

Fig. 6.3: Measurement for the determination of the Rydberg deexcitation laser Rabi frequency for the transition $|51S_{1/2}\rangle \rightarrow |6P_{3/2}\rangle$. The mean ion count is plotted as a function of the Rydberg deexcitation duration. A fit to the data results in a Rabi frequency of $\Omega = 26.8(14)\,\mathrm{MHz}$.

duration. After that, the atoms are ionized with the electric field pulse and the produced ions are detected on the MCP.

Fig. 6.3 shows the mean ion count on the MCP as a function of the deexcitation duration of the Rydberg atoms. Since the AOM that switches the Rydberg deexcitation laser has a rise time of around 40 ns, the measurement is performed for deexcitation durations larger than 50 ns.

The Rabi frequency Ω is extracted by fitting the product of an exponential function and a cosine to the data in the figure. Although only two Rabi oscillations are visible, the fit delivers satisfactory results and yields a Rabi frequency $\Omega = 26.8(14)\,\mathrm{MHz}$. Using Eqn. (5.7) and (5.8) and solving for the waist, one obtains $w = 7.3(3)\,\mu\mathrm{m}$. The necessary dipole matrix elements for the calculations have been taken from an institute-internal database.

6.4 Simulation of the ac Stark shift

Since the photoionization laser is operated at high powers and the laser beam is focused to a few microns, high intensities occur and the ac Stark effect needs to be considered in the evaluation of the experiment.

In Sec. 2.2.5 the ac Stark shift is presented and an example for a two-level system has been given. Here, calculations are expanded to a considerable amount of atomic levels $|j\rangle$. Before they are carried out for atomic levels in ^{87}Rb, the theoretical treatment from Sec. 2.2.5 is continued and specified. Starting from Eqn. (2.18), it is convenient to choose the energy of one state $|i\rangle$ such that $\mathcal{E}_i^0 = 0$. Additionally, Eqn. (2.18) can be rewritten in terms of wavelengths using the relation $\omega = 2\pi\nu = 2\pi c/\lambda$.

Making use of Eqn. (2.17), one obtains

$$\Delta\mathcal{E}_i = -\frac{|\mathbf{E}_0|^2}{2\pi\hbar c}\sum_j |\boldsymbol{\mu}_{ij}|^2 \left[\left(\frac{1}{\lambda_j}-\frac{1}{\lambda_\mathrm{L}}\right)^{-1}+\left(\frac{1}{\lambda_j}+\frac{1}{\lambda_\mathrm{L}}\right)^{-1}\right], \tag{6.1}$$

where $\boldsymbol{\mu}_{ij} = \langle i|\,\mathbf{d}\,|j\rangle$ is the dipole matrix element of the transition between atomic levels $|i\rangle$ and $|j\rangle$. Finally, the ac Stark shift can be expressed in terms of the light field intensity I using the relation $|\mathbf{E}_0|^2 = I/(2\epsilon_0 c)$ from Ref. [58]. The ac Stark shift of level $|i\rangle$ in units of frequencies is then given by

$$\Delta\nu_i = -\frac{I}{8\pi^2\hbar^2c^2\epsilon_0}\sum_j |\mu_{ij}|^2 \left[\left(\frac{1}{\lambda_j}-\frac{1}{\lambda_\mathrm{L}}\right)^{-1}+\left(\frac{1}{\lambda_j}+\frac{1}{\lambda_\mathrm{L}}\right)^{-1}\right], \tag{6.2}$$

emphasizing the linear intensity dependence.

In the simulations, the ac Stark shifts for the intermediate state $|6P_{3/2}, F=3, m_F=3\rangle$ and the Rydberg state $|51S_{1/2}, m_{J'}=1/2\rangle$ are calculated individually. The simulations are performed with σ^--polarized light (which is the laser polarization used in the experiment) at a wavelength of $\lambda_\mathrm{L} = 1010.186\,\mathrm{nm}$. The mean laser intensity is $I \approx 1\times10^{10}\,\mathrm{W/m^2}$, assuming an input power of 125 mW (see Eqn. (5.8)) focused down to a waist of 2 µm. Calculations are done in the $|J, m_J; J', m_{J'}\rangle$ basis, since the hyperfine splitting of many atomic levels cannot be resolved with the lasers used in the experiment, and the photoionization laser is far detuned to atomic resonance frequencies. Besides, by the choice of this basis and the associated consideration of $m_{J^{(\prime)}}$ levels, contributions from the scalar, vector and tensor ac Stark shift are covered in the simulations [67, 99].

To obtain the ac Stark shift of the $|6P_{3/2}, m_J=3/2\rangle$ state in the $|J, m_J; J', m_{J'}\rangle$ basis, only the transitions allowed by dipole selection rules to the $|nS_{1/2}, m_{J'}=1/2\rangle$, $|nD_{3/2}, m_{J'}=1/2\rangle$ and $|nD_{5/2}, m_{J'}=1/2\rangle$ states are considered for principal quantum numbers $n\in[5,200]$. In the simulation, the $|6P_{3/2}\rangle$ state is treated as the state with zero energy. The wavelengths and dipole matrix elements necessary for the simulation have been taken from an institute-internal database. Analogously, the shift for the $|51S_{1/2}, m_{J'}=1/2\rangle$ Rydberg state is simulated. Due to the σ^- laser polarization, only transitions to $|nP_{3/2}, m_J=3/2\rangle$ states with $n\in[5,200]$ are taken into account.

The simulation results of the ac Stark shift are depicted in Fig. 6.4. There, the total ac Stark shift is plotted as a function of the energetically highest state considered in the sum of Eqn. (6.2). The plot is limited to states with high principal quantum numbers close to the ionization threshold. The results show that only the contributions from the $|51S_{1/2}\rangle \rightarrow |nP_{3/2}\rangle$ transitions converge for $\mathcal{E}\rightarrow 0\,\mathrm{eV}$ to a value of 22.5 MHz. Fitting an exponential function to the simulated total ac Stark shift values of the $|51S_{1/2}\rangle \rightarrow |nP_{3/2}\rangle$ transition, one can predict the behavior for Rydberg states with principal quantum numbers $n>200$, yielding a total ac Stark shift of the $|51S_{1/2}\rangle$ level of $\Delta\nu_{51S_{1/2}} = 22.6\,\mathrm{MHz}$. A brief discussion of this value is carried out in Sec. 6.5.

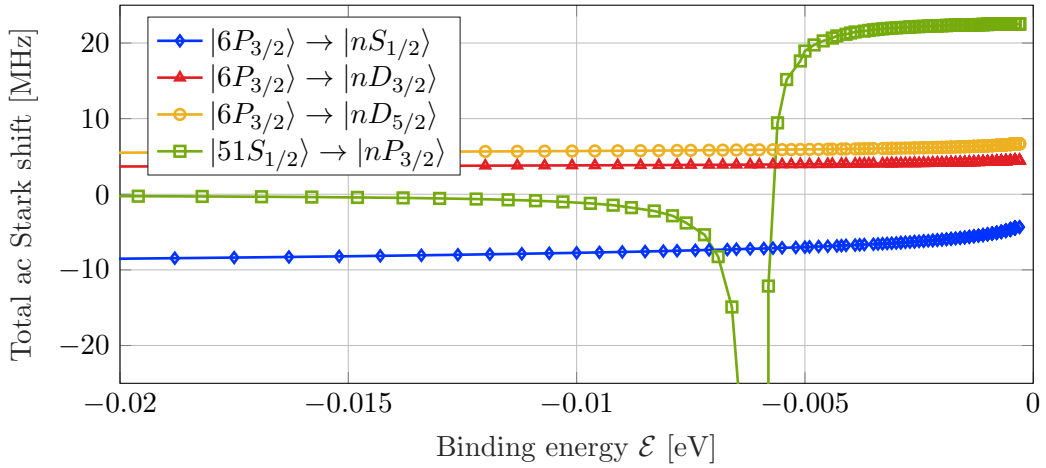

Fig. 6.4: Total ac Stark shift for all dipole-allowed transition from the $|51S_{1/2}\rangle$ and $|6P_{3/2}\rangle$ states adressed with σ^--polarized light. The simulation is performed with a photoionization laser power of 125 mW and a waist of 2 µm yielding an intensity of approximately $1 \times 10^{10}\,\mathrm{W/m^2}$. The plot shows four different contributions to the ac Stark shift. The shift of each data point in a data set represents the sum of all shifts of lower-lying states such that one data point always indicates the total ac Stark shift up to the respective state. The plot only shows contributions of states close to the ionization threshold. Contributions from transitions from the $|6P_{3/2}\rangle$ state do not seem to converge for $\mathcal{E} \rightarrow 0\,\mathrm{eV}$. Contributions to the ac Stark shift of the $|6P_{3/2}\rangle$ mostly originate from low-lying states around $n = 6$. However, for energies close to the ionization threshold, the shift increases. This might be due to contributions from the continuum and will be discussed in Sec. 6.8. The figure also points out that the shift of the $|51S_{1/2}\rangle$ arises mainly due to contributions from the states $|44P_{3/2}\rangle$ to $|58P_{3/2}\rangle$. Close to the $|51S_{1/2}\rangle$ Rydberg state, the ac Stark shift is particularly high. This is due to the large overlap of the respective wavefunctions represented by high dipole matrix elements in that region. Low-lying states do not have a significant influence to the shift. For instance, the contribution of the $|6P_{3/2}\rangle$ state to the ac Stark shift of the Rydberg state is only on the order of 45 kHz.

Unfortunately, contributions from transitions starting from the intermediate $|6P_{3/2}\rangle$ state do not converge in this simulation. Possible reasons are contributions from the continuum [2], as the 1010 nm laser drives transitions from said intermediate state into the continuum. As a consequence, the simulated value of the ac Stark shift $\Delta\nu_{6P_{3/2}} = 6.8\,\mathrm{MHz}$ cannot provide a reliable statement. To gain robust data on this ac Stark shift, a further experimental analysis is necessary. The experiment and the results obtained are presented in Sec. 6.6.

All simulations contain uncertainties due to the dipole matrix elements. Since no uncertainties of the dipole matrix elements are available, a quantitative value of the simulation uncertainty is not specified. As mentioned above, the influence continuum is not considered in the simulations, hence no simulation inaccuracies are given for that. However, it would be interesting to include the continuum in the ac Stark shift simulations in a further analysis. Only pure light polarizations are considered in the simulations.

6.5 The ponderomotive potential

In a classical picture, a free electron with mass m_e and charge e placed inside a high-intensity laser beam with light frequency ω_L undertakes a sinusodial motion due to the oscillating electric field. The time-averaged kinetic energy of this process is called the ponderomotive potential [100–102], which is given by

$$\mathcal{E}_\mathrm{pm}(\omega_\mathrm{L}) = \frac{e^2\mathbf{E}^2}{4m_e\omega_\mathrm{L}^2}. \tag{6.3}$$

The frequency shift related to the ponderomotive potential in Eqn. (6.3) is calculated and expressed in terms of the quantities wavelength λ_L and mean laser intensity I. This yields an intensity-dependent ponderomotive potential of

$$\Delta\nu_\mathrm{pm} = \frac{e^2\lambda_\mathrm{L}^2 I}{8\pi^2 m_e \epsilon_0 h c^3}. \tag{6.4}$$

For the wavelength and intensity as specified in Sec. 6.4, the ponderomotive potential of a free electron is given by $\Delta\nu_\mathrm{pm} = 22.9\,\mathrm{MHz}$, which is comparable to the numerical value obtained in the ac Stark shift simulations for the $|51S_{1/2}\rangle$ state. The assumption that the ac Stark shift for high-lying Rydberg states converges to the ponderomotive potential of a free electron is supported by the fact that ac Stark shift simulations for the $|101S_{1/2}\rangle$, $|151S_{1/2}\rangle$, and $|171S_{1/2}\rangle$ Rydberg state all deliver the result $\Delta\nu_{nS_{1/2}} \to \Delta\nu_\mathrm{pm}$. Since the $|51S_{1/2}\rangle$ Rydberg state has an energy close to the ionization threshold, it is valid to compare at least the order of magnitude of the ponderomotive potential to the ac Stark shift of the Rydberg state. In the context of this consistency check, the simulation results for the $|51S_{1/2}\rangle$ state seem to be quite accurate.

6.6 Measurement of the intermediate state detuning

Due to the non-converging behavior of the ac Stark shift of the $|6P_{3/2}\rangle$ state in the simulations in Sec. 6.4, measurements are performed to gain more reliable data. In the following, the experimental procedure of the measurement is described and the results are presented. However, only the differential ac Stark shift containing contributions from the $|5S_{1/2}\rangle$ ground state can be measured. The consequences are discussed later in this section.

For the measurement, a two-photon excitation scheme in ladder-configuration is used. The lower transition from the $|5S_{1/2}\rangle$ ground state to the $|6P_{3/2}\rangle$ intermediate state in ^{87}Rb is driven by the 420 nm laser. The 1010 nm photoionization laser drives the upper transition from the intermediate state into the continuum.

The 420 nm laser is tuned in resonance with the $|5S_{1/2}\rangle \to |6P_{3/2}\rangle$ transition by setting the intermediate state detuning Δ (see Sec. 3.1) to zero. This can be achieved by changing

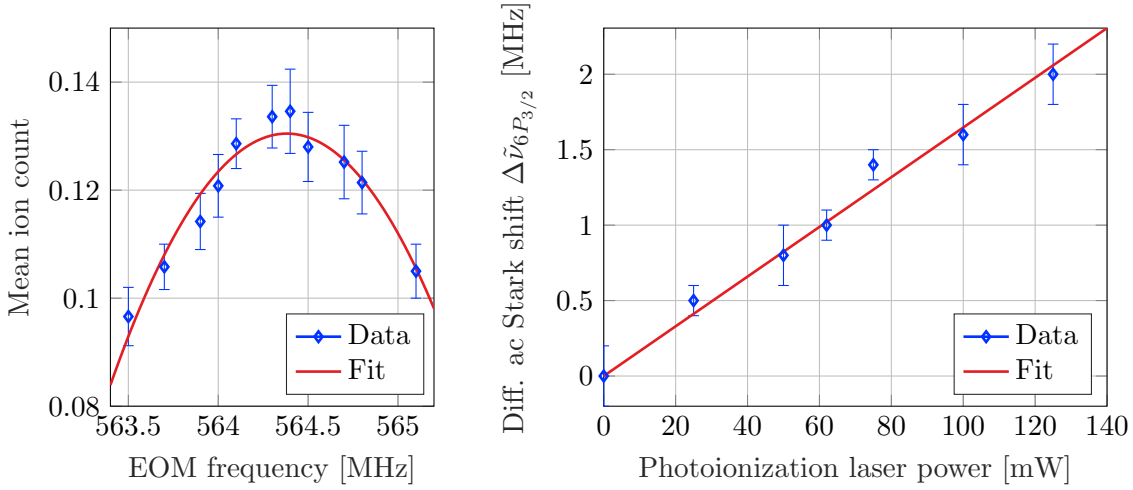

Fig. 6.5: Results of the intermediate state detuning measurement. Left: For a photoionization laser power of 75 mW the spectrum of the $|5S_{1/5}\rangle \rightarrow |6P_{3/2}\rangle$ transition resonance is measured by detuning the EOM frequency of the 420 nm laser lock. A parabola is fitted to the data to extract the frequency of the maximum mean ion count. Right: The differential ac Stark shift of the $|6P_{3/2}\rangle$ state plotted as a function of the photoionization laser power. The value at zero power is determined via the atom loss due to heating of the 420 nm laser at the resonance frequency of 565 MHz. For a total photoionization power of 125 mW the measured differential ac Stark shift is $\Delta\tilde{\nu}_{6P_{3/2}} = 2.0(4)$ MHz. The error bars in the left plot are given by the standard deviation of the mean ion count, in the right plot they are determined by the fit error of the parabola.

the frequency of the cavity sideband in the ULE cavity, on which the laser is frequency-stabilized[27]. The sideband itself is modulated by an EOM using the Pound-Drever-Hall technique [98].

The wavelength of the photoionization laser is set to 1010.186 nm to photoionize the atoms out of the $|6P_{3/2}\rangle$ intermediate state. The produced ions with an excess kinetic energy $\mathcal{E}_{\text{ion}} = 0.84$ neV above the ionization threshold of ^{87}Rb are detected on the MCP. As in the measurement of the photoionization efficiency in Sec. 6.2, the experiment is performed in a thermal cloud with around 1.2×10^5 atoms and a density of around $2.5 \times 10^{13}\,\text{cm}^{-3}$.

At first, the resonance frequency of the 420 nm laser is determined. Therefore, the atom loss of the thermal cloud is measured as a function of the EOM frequency. During this process, the photoionization laser is not turned on. For frequencies close to the resonance, more atoms get heated by the 420 nm laser leading to a high atom loss. The highest atom loss and thus the resonance occurs at an EOM frequency of 565 MHz. Once the resonance is found, the power of the 420 nm laser is reduced to minimize heating of the thermal cloud and photoionizations via two-photon processes of the 420 nm laser [81].

The photoionization laser is turned on and for six different laser powers the differential

[27] Actually, a 840 nm laser is frequency-stabilized to the ULE cavity and the light at 420 nm is generated by second harmonic generation (SHG) only afterwards.

shift of the $|5S_{1/2}\rangle \rightarrow |6P_{3/2}\rangle$ transition resonance due to the ac Stark effect is measured by shifting the EOM frequency. An exemplary measurement of the EOM resonance shift for a photoionization laser power of 75 mW is shown in the left part of Fig. 6.5. The ions detected by the MCP are plotted as a function of the EOM frequency detuning. To obtain the mean ion count, the fraction of ions that are produced within 500 photoionization cycles with pulse length 200 ns are counted and both the average and the standard deviation over 5-7 experimental runs are taken. By fitting a parabola to the data the differential frequency shift of the $|5S_{1/2}\rangle \rightarrow |6P_{3/2}\rangle$ transition resonance is obtained.

To obtain the differential ac Stark shift with respect to the resonance frequency of the $|5S_{1/2}\rangle \rightarrow |6P_{3/2}\rangle$ transition, the frequency shifts are normalized with the resonance frequency of the EOM at 565 MHz and multiplied by a factor of 2 to account for the fact that the light of the 420 nm laser is frequency-doubled from a 840 nm laser. The results are shown in Fig. 6.5 (right). There, the measured differential ac Stark shift of the transition is plotted as a function of the photoionization laser power. A linear fit to the data reveals a shift of 16.5(10) kHz/mW. For a photoionization power of 125 mW focused to 2 µm, the differential ac Stark shift taken from the data is $\Delta\tilde{\nu}_{6P_{3/2}} = 2.0(4)$ MHz. The error bars are determined by the fit errors of the parabolae in Fig. 6.5 (left).

As mentioned before, the 420 nm laser couples the $|5S_{1/2}\rangle$ ground state and the $|6P_{3/2}\rangle$ intermediate state resonantly, and thus the measurement result $\Delta\tilde{\nu}_{6P_{3/2}} = 2.0(4)$ MHz is only a differential shift that additionally includes the ac Stark shift of the $|5S_{1/2}\rangle$ ground state. The ac Stark shift of the ground state can easily be determined with the simulation presented in Sec. 6.4 yielding a fast-converging value of $\Delta\nu_{5S_{1/2}} = -37.5$ MHz. This value agrees with calculations based on Ref. [65]. With the simulated value for the ground state and the measured differential ac Stark shift, one can calculate the shift of the $|6P_{3/2}\rangle$ state, which leads to a value of $\Delta\nu_{6P_{3/2}} = -35.5$ MHz.

The simulation for the ground state ac Stark shift and the experimental results show that the photoionization laser leads to a red shift of the $|6P_{3/2}\rangle$ state. In contrast, the $|51S_{1/2}\rangle$ state experiences a blue shift that is compliant with the results of the simulation and the ponderomotive potential calculation.

The ac Stark shift simulations, the calculations of the ponderomotive potential and the measurements of the intermediate state detuning draw a comprehensive picture of the influence of the photoionization laser onto the atom, as far as the ac Stark shift is concerned. For a photoionization laser power of 125 mW, all previous considerations result in an ac Stark shift of

$$\Delta\nu_{\mathrm{ac}} = \Delta\nu_{51S_{1/2}} - \Delta\nu_{6P_{3/2}} \approx 58\,\mathrm{MHz}. \tag{6.5}$$

Here, the simulated value of the $|51S_{1/2}\rangle$ Rydberg state from Sec. 6.4 is used and the experimental value of the $|6P_{3/2}\rangle$ intermediate state, rectified by the simulated ground state shift, is taken. In this result, the uncertainty of the experimental value of the ac Stark shift is omitted due to the unknown uncertainties in the simulated values (see Sec. 6.4). The ac

Stark shift from Eqn. (6.5) as a function of the photoionization laser power is then given by

$$\Delta\nu_{\mathrm{ac}}(P) = 0.464\,\frac{\mathrm{MHz}}{\mathrm{mW}} \times P. \tag{6.6}$$

6.7 Evaluation of the photoionization cross section

To be able to determine the timescale of the V-type photoionization, it is essential to know precisely the photoionization cross section σ for the transition from the $|6P_{3/2}\rangle$ state into the continuum. There are theoretical calculations for the cross section [103] and experimental results by different groups [97, 104, 105]. However, there are no measurements of the photoionization cross section for energies directly over the ionization threshold. This is why a method of determining the photoionization cross section σ for an ionization directly above the ionization threshold will be presented in this section.

The basis for this evaluation is the measurement of the photoionization efficiency as a function of the photoionization laser power described in Sec. 6.2. Necessary parameters such as the waist $w = 7.3(3)\,\mu\mathrm{m}$ of the Rydberg deexcitation laser or the ac Stark shift with $\Delta\nu_{\mathrm{ac}}/P = 0.464\,\mathrm{MHz/mW}$ are determined in Sec. 6.3 and 6.6, respectively. Further parameters required for the determination of σ are shown in Tab. 6.1.

To obtain the value of the photoionization cross section σ, the experimental values for the photoionization efficiency are compared to a numerical simulation that reflects the experimental conditions. The simulation is based on the experimental parameters given in Tab. 6.1 and considers the measured rise times of the AOMs of the deexcitation and the photoionization laser with 40 ns and 52 ns, respectively. In an iterative process, the value for the photoionization cross section in the simulation is changed until the simulation result for one value of the photoionization power matches the photoionization efficiency in Fig. 6.2. This process is repeated for all photoionization laser powers.

The measurement uncertainties from the photoionization efficiency measurement directly translate into uncertainties of the cross section. The latter are detemined by executing the evaluation of the cross section again with a photoionization efficiency that also contains the efficiency uncertainty given by the statistical deviation of the the mean ion count. This results in inaccuracies on the order of $0.1 \times 10^{-22}\,\mathrm{m}^2$. Moreover, measurement and fit inaccuracies in the determination of the Rydberg deexcitation laser waist are considered in the same fashion and also have a small influence on the cross section of approximately $0.1 \times 10^{-22}\,\mathrm{m}^2$. The most significant contribution in the evaluation originates from uncertainties in the photoionization laser waist. The not exactly known waist $w = 2\,\mu\mathrm{m}$ contains an estimated uncertainty of $\pm 0.2\,\mu\mathrm{m}$, yielding a deviation of approximately $0.8 \times 10^{-22}\,\mathrm{m}^2$. Variations in the photoionization laser power over the whole measurement, electric field drifts and stray fields during the measurement as well as broadening mechanisms are not considered in the error analysis. Assuming uncorrelated uncertainties, it is appropriate to add the individual

Tab. 6.1: Simulation parameters for the photoionization starting in the $|51S_{1/2}\rangle$ Rydberg state. The parameters resemble the experimental parameters outlined in this chapter.

Parameter	Symbol	Numeric value	Comment
Rydberg state	$\|r\rangle$	$\|51S_{1/2}\rangle$	–
Deexcitation laser waist	w_{re}	7.3 µm	–
Deexcitation laser power	P_{re}	3.5 mW	500 ns pulse
Photoionization laser waist	w_{ec}	2.0 µm	–
Photoionization laser power	P_{ec}	$0 - 125$ mW	200 ns pulse
Photoionization laser wavelength	λ	1010.186 nm	–
Intermediate detuning	Δ/P_{ec}	$2\pi \times 0.464$ MHz/mW	ac Stark shift

contributions up to gain a conservative estimate of the total uncertainty. This results in a value of $\Delta\sigma \approx 1.0 \times 10^{-22}\,\mathrm{m}^2$.

Fig. 6.6 shows the results for the photoionization cross section σ as a function of the photoionization laser power for three different situations. The first situation reflects the actual measurement and considers the ac Stark shift with $\Delta\nu_{\mathrm{ac}}/P = 0.464\,\mathrm{MHz/mW}$. A least squares fit reveals a power dependence of the cross section according to

$$\sigma(P) = 0.14(1) \times 10^{-22}\,\frac{\mathrm{m}^2}{\mathrm{mW}} \times P + 7.0(8) \times 10^{-22}\,\mathrm{m}^2. \tag{6.7}$$

This behavior is unexpected since the photoionization cross section should be independent of the laser power. For a laser power of 125 mW the evaluated photoionization cross section result is $23.8(10) \times 10^{-22}\,\mathrm{m}^2$. This value is much higher than the literature value of $\sigma = 15(4) \times 10^{-22}\,\mathrm{m}^2$ taken from Ref. [97] and smaller for low photoionization laser powers.

Two further evaluations are shown in Fig. 6.6. The evaluations correspond to a model neglecting the ac Stark shift and to a model including both the ac Stark shift and the dephasing of the Rydberg deexcitation transition. The former analysis without regarding the ac Stark shift shows the same non-constant behavior of the photoionization cross section as before. Yet, the slope is negative and much smaller.

However, the inclusion of a dephasing rate in addition to the ac Stark shift yields a photoionization cross section, which is independent of the photoionization laser power. As reasoned in the following, a dephasing of the Rydberg deexcitation transition is realistic and probably induced by the photoionization laser. In all previous considerations, a mean value for the ac Stark shift has been presumed. The ac Stark shift, however, is an intensity-dependent effect and the intensity profile of the lasers in the experiments is best described by a Gaussian function. This leads to a dephasing mechanism, which is assumed to depend linearly on the photoionization laser power. The simulation shows that a dephasing rate of $\gamma = 0.28\,\mathrm{MHz/mW} \times P$ yields a constant cross section. This dephasing value of γ is not unrealistic, since it is on the order of half the peak potential depth

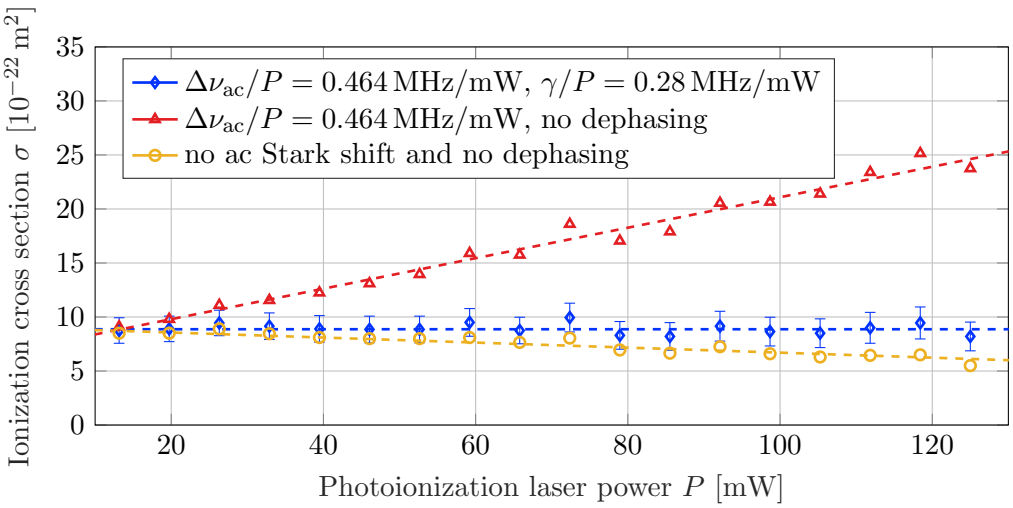

Fig. 6.6: Evaluation of the photoionization cross section σ for an ionization from the $|6P_{3/2}\rangle$ state for different photoionization powers at a wavelength of 1010.186 nm. The results are shown for model including an ac Stark shift of $\Delta\nu_{ac}/P = 0.464\,\text{MHz/mW}$ (triangles), for an evaluation without any shifts (circles) and for the case where a dephasing of the Rydberg deexcitation transition is taken into account with a rate of $\gamma/P = 0.28\,\text{MHz/mW}$ in addition to the ac Stark shift. Here, the cross section exhibits practically no power dependence (circles). The error bars for the former two evaluations are not shown for reasons of clarity. The dashed lines represent the linear fit functions.

created by the photoionization laser. The described model leads to an intensity-independent photoionization cross section and to a fit value of $\sigma = 8.9(10) \times 10^{-22}\,\text{m}^2$ in the latter comparison evaluation.

The aforementioned dephasing effect could be included in the simulations by averaging over position-dependent detunings within the excitation volume. The implementation of this effect might be subject of further research.

6.8 Discussion of the results

Recalling the evaluation results of the photoionization cross section from the previous section, several points warrant a closer examination. Above all, the photoionization cross section of $8.9(10) \times 10^{-22}\,\text{m}^2$ extracted with the described model is roughly by a factor 2 smaller than the literature value of $\sigma = 15(4) \times 10^{-22}\,\text{m}^2$ given in Ref. [97]. This smaller value of the photoionization cross section cannot be explained entirely with the data taken in measurements and with the previously outlined theory. In the following, possible explanations will be presented.

The excitation bandwidth of both lasers involved in the V-type photoionization scheme is not taken into account in the simulations, and therefore might play a role. Furthermore, the density shift on the order of 1 MHz for a density of around $2.5 \times 10^{13}\,\text{cm}^{-3}$ is not considered in the analysis. Still, it is presumed that those effects do not fully explain a factor of 2.

One possible reason for photoionization cross section σ being half as large as expected might be that the photoionization laser hits a so-called Cooper minimum in the continuum. This needs to be briefly adressed in the following. The photoionization cross section is a function of the oscillator strength distribution. A non-negligible amount of the oscillator strength distribution lies in the continuum [2]. However, the oscillator strength distribution is not constant over the whole energy spectrum of the continuum and a minimum referred to as the Cooper minimum can occur. In all alkali metals except for lithium, the Cooper minimum appears shortly across the ionization threshold. Its position is a function of the electronic continuum wavefunctions and it leads to a lower value of the photoionization cross section [106–108].

A method on how to calculate the oscillator stength distribution for transitions into the continuum is given in Ref. [109]. To experimentally check if a Cooper minimum is hit with the 1010 nm laser, the experimental procedures described in Ch. 6 can simply be repeated at different wavelengths, for instance to map out the oscillator strength distribution above the ionization limit.

It might be interesting to determine the photoionization cross section in an alternative way compared to the ansatz presented in this work. For instance, the flourescence signal detected from trapped atoms inside a magneto-optical trap (MOT) can be measured. By comparing the resulting loss rates of the MOT with and without radiation by a photoionization laser being present, the photoionization cross section can be extracted, as presented in Refs. [88, 110–113].

In another way, the ionization cross section can be determined by using a two-step photoionization process as presented in Ref. [114] for lithium or in Ref. [115] for rubidium. With this so-called saturation technique, atoms get excited from the ground state to an intermediate state such that the transition is saturated and the populations of both states become nearly equal. From the intermediate state, the atoms get photoionized during a high intensity laser pulse with reproducible shape and a well-defined pulse energy. The number of produced ions is measured as a function of the photoionization laser energy and an exponential fit delivers the photoionization cross section[28].

These two methods could be used to obtain a comparison value for the photoionization cross section and to double-check the accuracy of the method described in this thesis. Especially the saturation technique can readily be implemented in the experiments at the institute and can easily be measured.

It is suggested to perform further measurements in a similar way as presented in Sec. 6.6 to gain full experimental knowledge of the ac Stark shift, especially of the Rydberg state. This

[28] At this point it is in order to mention that the Rydberg deexcitation transition used for the measurement of the photoionization efficiency is not saturated and due to the dephasing a similar population in the Rydberg and intermediate state can hardly be reached. Hence, it is not reasonable to determine the photoionization cross section with the saturation method, although all necessary parameters for the exponential fit are sufficiently known.

knowledge is necessary, since the optical setup of the 1020 nm laser system, especially as far as the installation of the AOMs is concerned, depends on the intensity-dependent shift of the transitions adressed by the laser.

To conclude, the experiments performed in the scope of this thesis and the results presented in this chapter provide a profound overview of the production of slow ions utilizing a V-type photoionization scheme. Many effects associated with this new photoionization process are studied and an approach how to tackle the arising problems is given. A value of the photoionization cross section of $\sigma = 8.9(10) \times 10^{-22}\,\mathrm{m}^2$ is determined.

7 Summary and Outlook

In this thesis, the implementation of a V-type photoionization scheme to create cold ions from rubidium Rydberg atoms has been presented. The V-type photoionization scheme utilizes a laser with 1020 nm wavelenth, which deexcites Rydberg atoms into the $|6P_{3/2}\rangle$ intermediate state. A second laser with a wavelength around 1010 nm, tuned close to the ionization threshold, photoionizes the ^{87}Rb atom producing a low-energy ion.

The optical setup that has been established comprises a Toptica DLpro laser at a wavelength of 1010 nm, a self-built transfer cavity to stabilize the aforementioned laser and a self-built tapered amplifier to obtain laser powers on the order of 1 W.

A novel, and modular cavity design including active length-stabilization to allow for a transfer lock from a frequence stable 780 nm laser to the 1010 nm photoionization laser has been presented and realized. The free spectral range of the cavity has been measured to be 928(65) MHz and its finesse has been determined, leading to values of 143(53) for the former wavelength and 371(41) for the latter wavelength.

Simulations of the V-type photoionization scheme have been perfomed in order to achieve an understanding of the photoionization timescale. For a photoionization starting in the $|40S_{1/2}\rangle$ Rydberg state, a minimum photoionization time of 41 ns has been simulated, regarding the rise times of the AOMs used in the setup and assuming parameters based on the actual experiment.

Additional measurements and simulations have been performed to determine the photoionization cross section of the transition from the $|6P_{3/2}\rangle$ state into the continuum. The measurement of the power-dependent photoionization efficiency has been combined with the photoionization simulations resulting in a photoionization cross section of $8.9(10) \times 10^{-22}\,\mathrm{m}^2$ close to the ionization threshold. The ac Stark shift of the transition between the $|51S_{1/2}\rangle$ Rydberg state and the intermediate $|6P_{3/2}\rangle$ state imparted by the high intensity photoionization laser has been calculated and included into the photoionization simulations. A total ac Stark shift of 58 MHz has been determined for a photoionization laser intensity around $1 \times 10^{10}\,\mathrm{W/m^2}$.

The photoionization laser system set up in the scope of this thesis has also been used to analyze the Rydberg blockade induced by a single ion. In addition, cold ions produced via photoionization have be applied to sense electric fields in atomic physics experiments down to the level of µV/cm on a single-ion basis [1].

Exciting new measurements can be performed utilizing the generation of ultracold ions with a V-type photoionization scheme at a fast repetition rate. It will be interesting to perform analogous measurements to the ones presented in Ref. [1] in a Bose-Einstein condensate, and to study transport properties of cold charged particles at high atomic densities [116].

To characterize the spatial resolution of the ion microscope [50] in the experimental setup and to calibrate the magnification, the photoionization laser will be used to create an optical lattice with a variable lattice period. The necessary setup of this so-called accordion-type lattice is described inRef. [117].

With the whole experimental apparatus being operative, it will be possible to initially observe cold ion-atom interactions in the Rb^+-Rb-system with high spatial and temporal resolution. After the implementation of the lithium laser systems and the lithium oven, the ion-atom interaction studies will be extended to the Li^+-Li system, and pushed to the so far unexplored, ultracold quantum regime [38].

The research conducted in this master thesis has proven, that the V-type photoionization scheme is a versatile new instrument that allows for a wide range of possible applications in the future exploration of new phenomena in the field of Rydberg physics.

A Appendix

A.1 Derivation of the $\langle F, m_F| \mathbf{d} |J', m_{J'}\rangle$ matrix element

In order to describe dipole transitions from a $|F, m_F\rangle$ state into a $|J', m_{J'}\rangle$ state correctly, one has to calculate the dipole matrix element $\langle F, m_F| \mathbf{d} |J', m_{J'}\rangle$. In the following, a detailled derivation is given.

The total atomic angular momentum $\mathbf{F} = \mathbf{J} + \mathbf{I}$ is a sum of the overall angular momentum of the electron $\mathbf{J}$ and the nuclear spin $\mathbf{I}$. By inserting the unity matrix $\mathbb{1}$ one can write

$$\langle F, m_F| \mathbf{d} |J', m_{J'}\rangle = \sum_{\substack{m_I, m_J \\ m_I + m_J = m_F}} \underbrace{\langle F, m_F | J, m_J; I, m_I\rangle}_{\text{CGC}} \langle J, m_J; I, m_I| \mathbf{d} |J', m_{J'}\rangle \tag{A.1}$$

identifying a Clebsch–Gordan coefficient (CGC) in the sum that is related to Wigner 3-j symbols [58] as follows

$$\langle F, m_F | J, m_J; I, m_I\rangle = (-1)^{J-I+m_F} \sqrt{2F+1} \begin{pmatrix} J & I & F \\ m_J & m_I & -m_F \end{pmatrix}. \tag{A.2}$$

To further evaluate the sum, dipole selection rules and the construction of m_F can be used. It is $m_J = m_{J'} + q$ for non-vanishing Wigner 3-j symbols and $m_J + m_I = m_F$. Combining both terms, one yields $m_I = m_F - m_{J'} - q$. The parameter $q = \{-1, 0, +1\}$ labels the three different polarizations $\{\sigma^+, \pi, \sigma^-\}$ of light [78]. Now, m_I and m_J are expressed by known quantities and are fixed. Hence, the sum over m_I and m_J is obsolete and the matrix element becomes

$$\begin{aligned} \langle F, m_F| \mathbf{d} |J', m_{J'}\rangle &= (-1)^{J-I+m_F} \sqrt{2F+1} \\ &\times \begin{pmatrix} J & I & F \\ m_{J'} + q & m_F - m_{J'} - q & -m_F \end{pmatrix} \langle J, m_J| \mathbf{d}_q |J', m_{J'}\rangle . \end{aligned} \tag{A.3}$$

As depicted in Eqn. (2.36), the matrix element $\langle J, m_J| \mathbf{d}_q |J', m_{J'}\rangle$ decomposes into another Clebsch-Gordan coefficient and a reduced dipole matrix element. Evaluating said Clebsch-Gordan coefficient in the same fashion as in Eqn. (A.2) and putting it into Eqn. (A.3), one obtains

$$\begin{aligned} \langle F, m_F| \mathbf{d} |J', m_{J'}\rangle &= (-1)^{J'+J-I-1+m_F+m_{J'}+q} \sqrt{(2F+1)(2J+1)} \\ &\times \begin{pmatrix} J & I & F \\ m_{J'} + q & m_F - m_{J'} - q & -m_F \end{pmatrix} \begin{pmatrix} J' & 1 & J \\ m_{J'} & q & -m_{J'} - q \end{pmatrix} \\ &\times \langle J \| \mathbf{d} \| J' \rangle . \end{aligned} \tag{A.4}$$

The full dipole matrix can be calculated using the expressions for the reduced dipole matrix elements $\langle J\|\mathbf{d}\|J'\rangle$ and $\langle L\|\mathbf{d}\|L'\rangle$ as well as the radial matrix element $\boldsymbol{\mu}_{\mathrm{rad}} = \langle nL|\, e\mathbf{r}\,|n'L'\rangle$ in Eqns. (2.37)–(2.39), respectively. The final result for the dipole matrix element $\langle F, m_F|\,\mathbf{d}\,|J', m_{J'}\rangle$ is then given by

$$\begin{aligned}\langle F, m_F|\,\mathbf{d}\,|J', m_{J'}\rangle = (-1)^{J'+J-I-1+m_F+m_{J'}+q}&\sqrt{(2F+1)(2J+1)}\\ &\times \begin{pmatrix} J & I & F \\ m_{J'}+q & m_F-m_{J'}-q & -m_F \end{pmatrix}\begin{pmatrix} J' & 1 & J \\ m_{J'} & q & -m_{J'}-q \end{pmatrix}\\ &\times (-1)^{J'+L+1+S}\sqrt{(2J'+1)(2L+1)}\begin{Bmatrix} L & L' & 1 \\ J' & J & S \end{Bmatrix}\\ &\times (-1)^{-L}\sqrt{2L'+1}\begin{pmatrix} L & 1 & L' \\ 0 & 0 & 0 \end{pmatrix}\\ &\times \boldsymbol{\mu}_{\mathrm{rad}}.\end{aligned} \tag{A.5}$$

A.2 PID circuit and modifications

Fig. A.1 shows the schematic of the PID controller that is used to lock the transfer cavity to a transmission peak of the 780 nm laser. The PID circuit is based on the institute's standard PID controller design and is modified such that the controller processes an input voltage in the range of $\pm 10\,\mathrm{V}$ and maps it to an output voltage of $0 - 3.3\,\mathrm{V}$. This is necessary to protect the piezo actuator from negative voltages and to allow for the side-lock technique with a positive error signal. More details on the circuit are given in the caption of the figure.

The PID contoller used to lock the photoionization laser on the transfer cavity is also based on the institute's standard PID design. However, only two small changes are made. Based on the current version V3.2, the integrator capacitance is changed to $C_{\mathrm{I}} = 1\,\mu\mathrm{F}$ and the slow output capacitance is changed to $C_{\mathrm{CSL}} = 4.7\,\mathrm{pF}$ to allow for a sufficient control bandwidth.

A.3 TA controller settings and protection circuit

The relevant controller settings for the TED 8020 and the LDC 8080 module inside the Thorlabs ITC 8052 Pro8000 controller, that drive the self-built tapered amplifier (TA), are listed in Tab. A.1.

In Fig. A.2 the schematic of the TA protection circuit is shown. The circuit prevents the TA from being supplied with the wrong current polarity and serves as an overvoltage protection.

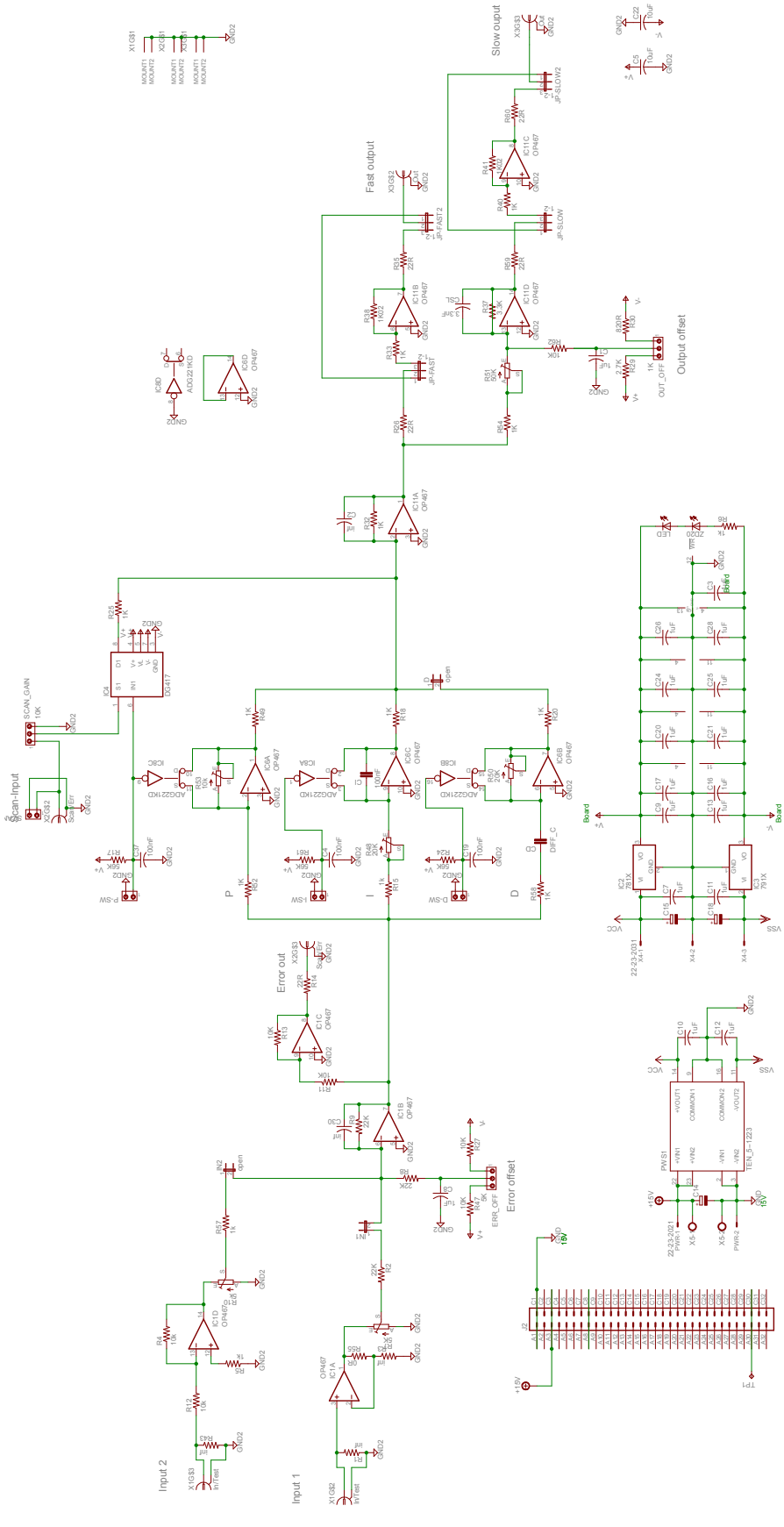

Fig. A.1: Circuit of the PID controller utilized to lock the transfer cavity. In contrast to the standard design, resistors R_2, R_8 and R_9 as well as R_{29} and R_{30} are changed such that the error offset can be adjusted in between $\pm 2\,\mathrm{V}$ and the output offset can be shifted from $2.5\,\mathrm{V}$ to $7.5\,\mathrm{V}$. Additionally, the resistance of the output offset poti is changed to $1\,\mathrm{k\Omega}$. Resistor R_{28} is removed and a direct connection including a new resistor $R_{62} = 10\,\mathrm{k\Omega}$ to pin 13 of OP467 is soldered. For the cavity lock, the slow output is used. Its bandwidth is 14.6 kHz, caused by $C_{\mathrm{CSL}} = 3.3\,\mathrm{nF}$ and $R_{37} = 3.3\,\mathrm{k\Omega}$. The IC buffer just before the output connection is removed completely. Setting the poti R_{51} to a value of $39\,\mathrm{k\Omega}$ allows for the aforementioned mapping to only positive output powers in the range of $0 - 3.3\,\mathrm{V}$.

Tab. A.1: Relevant parameters for the operation of the self-built TA used in the optical setup presented in Sec. 3.2. The control unit used to drive the TA is a Thorlabs ITC 8052 Pro8000 controller.

Module	Property	Parameter	Unit
Temperature controller TED 8020	T_S	22.500	°C
	`TEC`	`ON`	–
	`Twin`	`OFF`	–
	I_{lim}	2.000	A
	`Psh`	57.8	%
	`Ish`	25.0	%
	`Dsh`	4.0	%
	`Ishare`	`ON`	–
	`Temperature control`	`Thermistor`	–
	R_0	10.00	kΩ
	T_0	25.00	°C
	B	3988.0	kΩ
Laser diode controller LDC 8080	I_{LD}	5.800	A
	I_{lim}	5.990	A
	`Mode`	`Iconst`	–
	`LDPOL`	`AG`	–

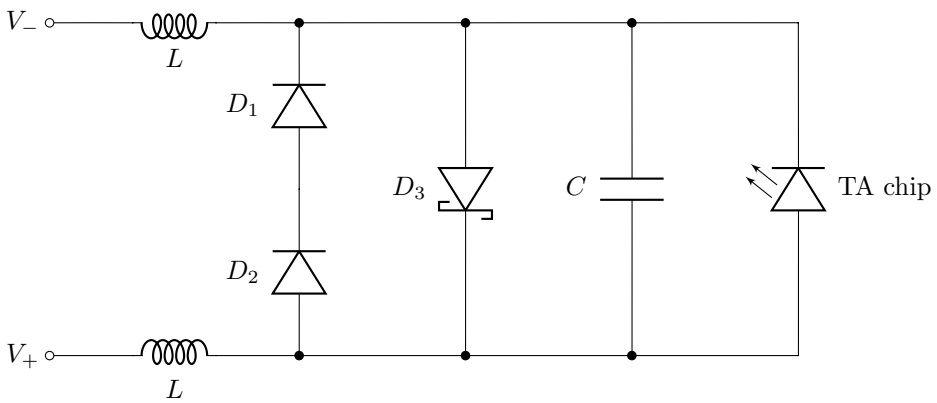

Fig. A.2: Schematic of the TA protection circuit. The two diodes D_1 and D_2 protect the circuit from overvoltage, the Schottky diode D_3 ensures that a wrong polarity of the input voltage $V_\pm$ does not damage the TA chip and the coils with inductivity L and the bipolar capacitor with capacitance C form a low-pass filter.

A.4 Coupling of the transfer cavity

This section gives a brief summary on how a laser is coupled into the cavity. Both lens tubes of the transfer cavity are not mounted at the beginning of the coupling procedure. Referring to the notation of the optical elements in Fig. 4.2, the lens L_0 is also not in the setup at the beginnig.

At first, two irides are mounted on the mirror mounts of the cavity and the mirrors M_3 and M_4 are used to adjust the incident laser beam such that the transmission through the nearly-closed irides reaches a maximum value.

The irides are removed and the concave mirror M_2 is mounted at its designated position. The aim is to couple the reflection of the mirror back into the polarization-maintaining single mode fiber. To find the correct position of the mirror, the set screws of the mirror mount are adjusted to a maximum power reflection into the fiber. After the fiber, the power of the reflected light is measured with a power meter, for instance at the second beam splitter in the optical setup, see Fig. 3.2. Due to the curvature of the mirror, only a small amount of light is actually coupled back into the fiber. Once the maximal power is reflected from the mirror into the fiber, the same procedure is repeated with the plane mirror M_1. The plane mirror should be adjusted with the piezo acuator in a position with an offset voltage close to the voltage later used to stabilize the cavity.

For the next steps it is vital that the laser is scanned over several free spectral ranges. After both mirrors are adjusted correctly, the lens L_0 is put up close to its calculated place. Observing the transmitted signal through the cavity with a photo diode behind the cavity and an oscilloscope, the position of the lens is altered until a position is found, in which the transmission signal looks best (compare Fig. 2.4).

Using the photo diode and walking the mirrors M_3 and M_4 one can improve the transmission signal by reducing the signal height of higher order cavity modes. Finally, using a CCD camera behind the cavity and viewing the transversal intensity profile of the transmitted cavity modes, one can slightly change the angle of the cavity mirrors M_1 and M_2 until, at best, only the Gaussian fundamental mode is transmitted. This completes the coupling of one laser to the cavity.

A.5 Drafts of the self-built transfer cavity

In Fig. A.3-A.6, the technical drawings of the spacer, the mirror mount body and front plate and piezo holder are presented. The spacer is based on a custom-made stainless steel tube (see Sec. 4.2), the mirror mount body and front plate are commercial items and the the piezo holder is made from stainless steel.

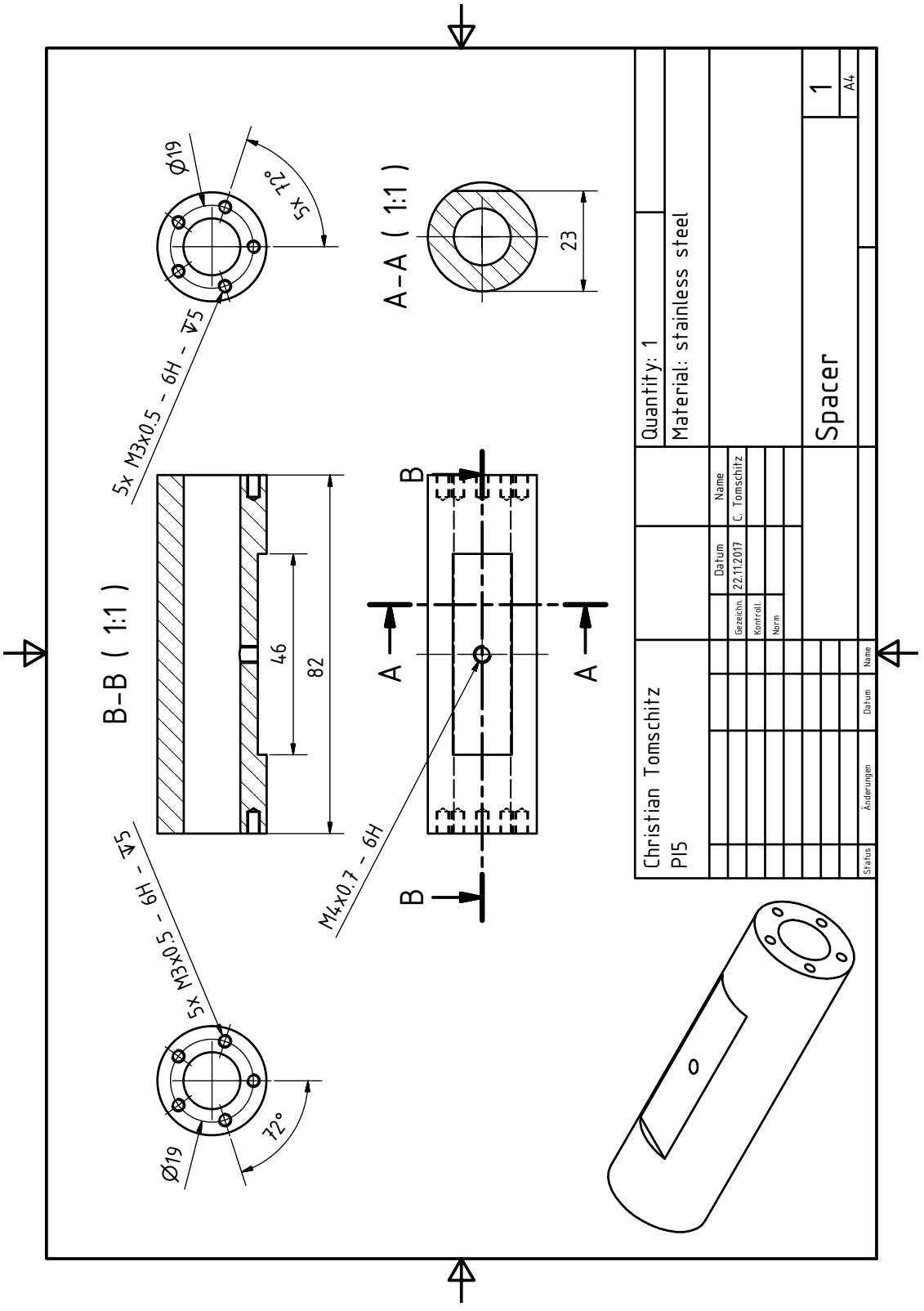

Fig. A.3: Technical drawing of the spacer.

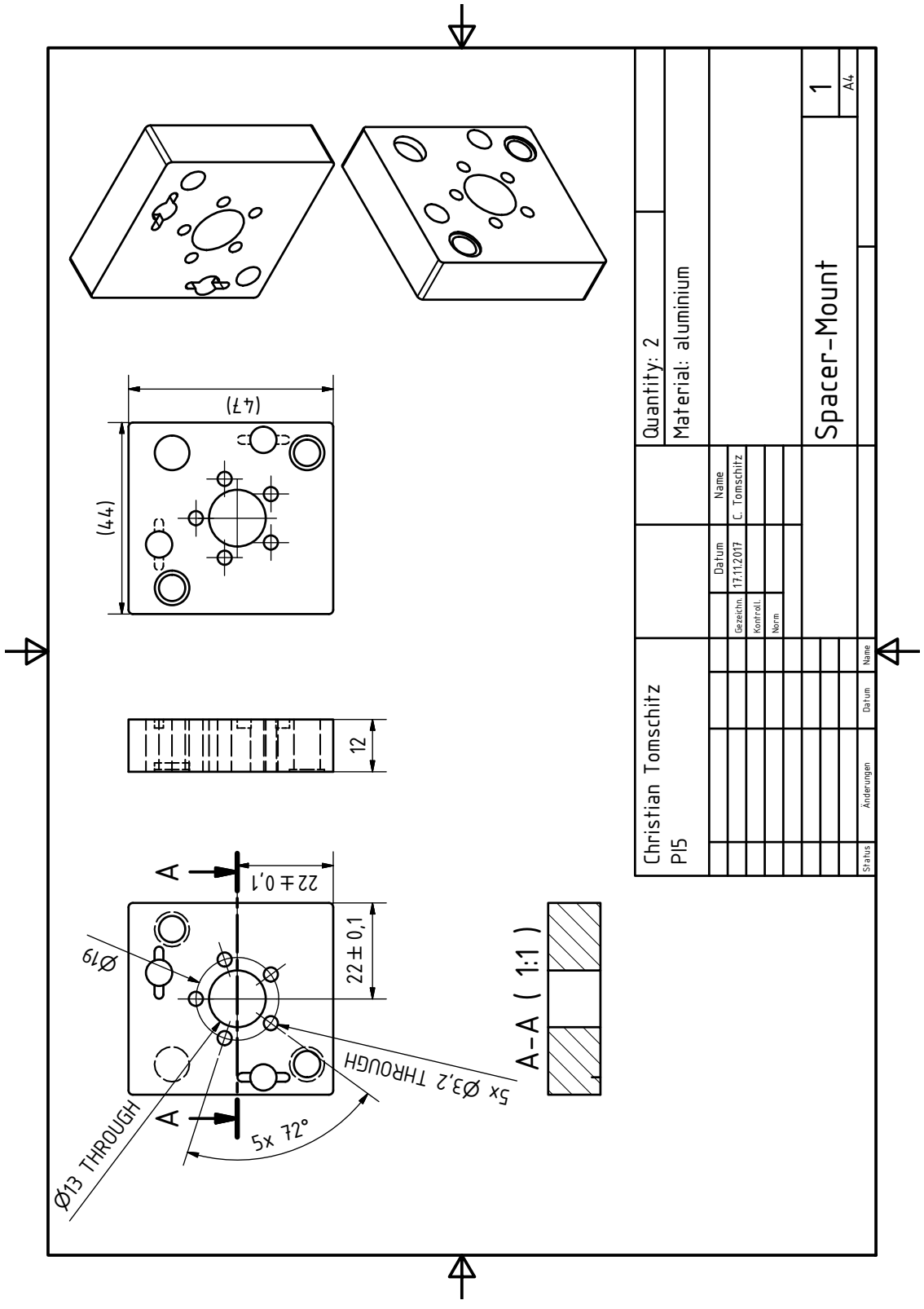

Fig. A.4: Technical drawing of the mirror mount (body).

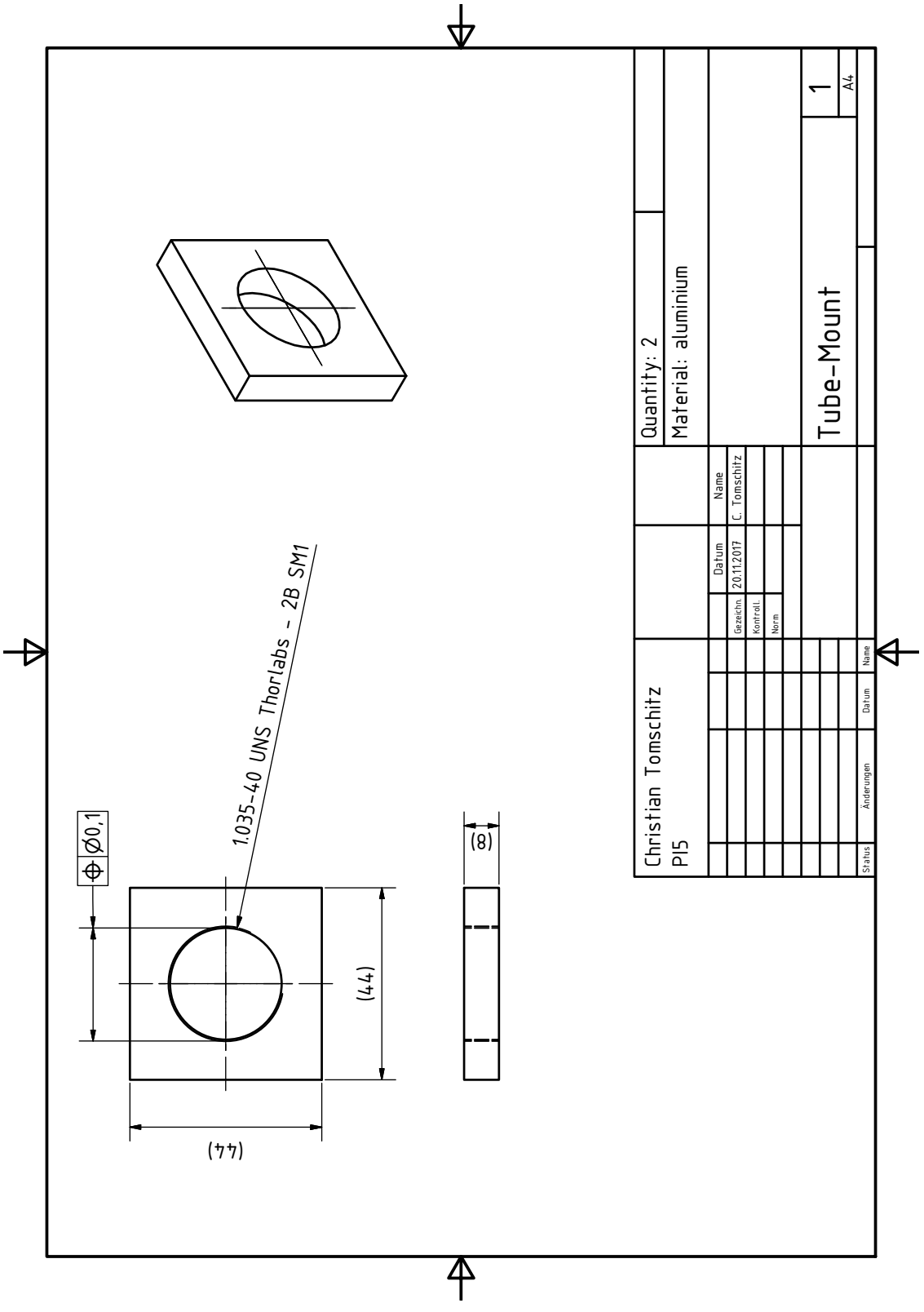

Fig. A.5: Technical drawing of the mirror mount (front plate).

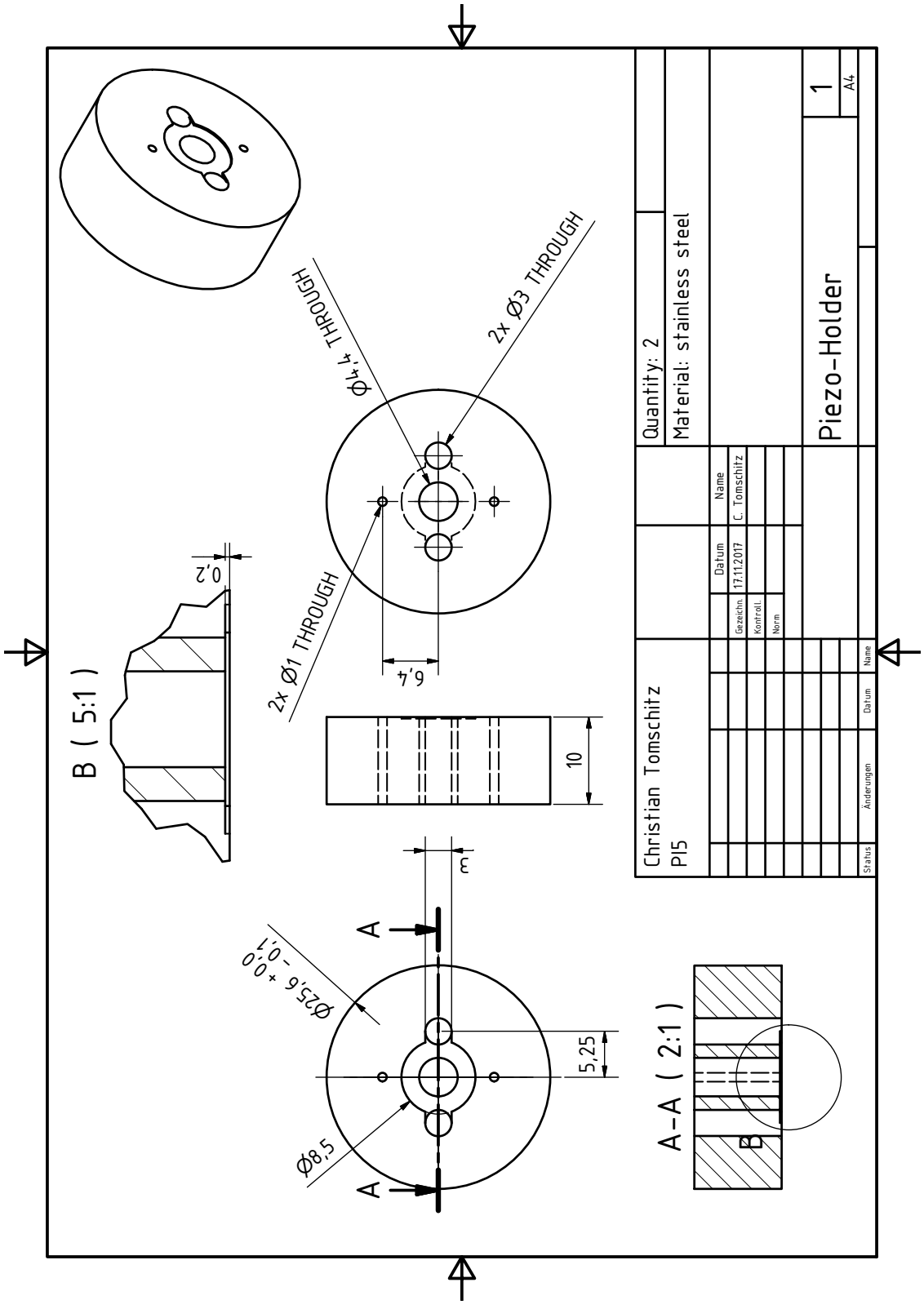

Fig. A.6: Technical drawing of the piezo holder.

Bibliography

[1] F. Engel, T. Dieterle, T. Schmid, C. Tomschitz, C. Veit, N. Zuber, R. Löw, T. Pfau and F. Meinert: *Observation of Rydberg Blockade Induced by a Single Ion.* 2018. Accepted in PRL. Online available at http://arxiv.org/pdf/1809.00993v1.

[2] T. F. Gallagher: *Rydberg Atoms.* Cambridge University Press, Cambridge, 1994.

[3] I. Martinson and L. J. Curtis: *Janne Rydberg – his life and work.* In: *Nuclear Instruments and Methods in Physics Research Section B: Beam Interactions with Materials and Atoms* **235**, 1-4, 17–22. 2005.

[4] R. Löw, H. Weimer, J. Nipper, J. B. Balewski, B. Butscher, H. P. Büchler and T. Pfau: *An experimental and theoretical guide to strongly interacting Rydberg gases.* In: *Journal of Physics B: Atomic, Molecular and Optical Physics* **45**, 11, 113 001. 2012.

[5] I. I. Beterov, I. I. Ryabtsev, D. B. Tretyakov and V. M. Entin: *Quasiclassical calculations of blackbody-radiation-induced depopulation rates and effective lifetimes of Rydberg nS, nP, and nD alkali-metal atoms with $n \leq 80$.* In: *Physical Review A* **79**, 5. 2009.

[6] R. F. Gutterres, C. Amiot, A. Fioretti, C. Gabbanini, M. Mazzoni and O. Dulieu: *Determination of the ^{87}Rb 5p state dipole matrix element and radiative lifetime from the photoassociation spectroscopy of the $Rb_2 0_g^-(P_{3/2})$ long-range state.* In: *Physical Review A* **66**, 2, 2420. 2002.

[7] D. Tong, S. M. Farooqi, J. Stanojevic, S. Krishnan, Y. P. Zhang, R. Côté, E. E. Eyler and P. L. Gould: *Local blockade of Rydberg excitation in an ultracold gas.* In: *Physical review letters* **93**, 6, 063 001. 2004.

[8] E. Urban, T. A. Johnson, T. Henage, L. Isenhower, D. D. Yavuz, T. G. Walker and M. Saffman: *Observation of Rydberg blockade between two atoms.* In: *Nature Physics* **5**, 2, 110–114. 2009.

[9] D. Comparat and P. Pillet: *Dipole blockade in a cold Rydberg atomic sample.* In: *Journal of the Optical Society of America B* **27**, 6, A208. 2010.

[10] I. Cirac and P. Zoller: *Quantum Computations with Cold Trapped Ions.* In: *Physical review letters* **74**, 20, 4091–4094. 1995.

[11] L. Childress and R. Hanson: *Diamond NV centers for quantum computing and quantum networks.* In: *MRS Bulletin* **38**, 02, 134–138. 2013.

[12] J.-W. Zhou, P.-F. Wang, F.-Z. Shi, P. Huang, X. Kong, X.-K. Xu, Q. Zhang, Z.-X. Wang, X. Rong and J.-F. Du: *Quantum information processing and metrology with color centers in diamonds.* In: *Frontiers of Physics* **9**, 5, 587–597. 2014.

[13] D. Loss and D. P. DiVincenzo: *Quantum computation with quantum dots.* In: *Physical Review A* **57**, 1, 120–126. 1998.

[14] P. Michler: *Single Semiconductor Quantum Dots.* NanoScience and Technology. Springer, Heidelberg, 2009.

[15] P. Michler (Editor): *Quantum Dots for Quantum Information Technologies.* Nano-Optics and Nanophotonics. Springer, Cham, 2017.

[16] R. P. Feynman: *Simulating physics with computers.* In: *International Journal of Theoretical Physics* **21**, 6-7, 467–488. 1982.

[17] A. Zeilinger, C. Macchiavello and G. M. Palma: *Quantum computation and quantum information theory.* World Scientific, Singapore, 2000.

[18] M. D. Lukin, M. Fleischhauer, R. Cote, L. M. Duan, D. Jaksch, J. I. Cirac and P. Zoller: *Dipole blockade and quantum information processing in mesoscopic atomic ensembles.* In: *Physical review letters* **87**, 3, 037 901. 2001.

[19] M. A. Nielsen and I. L. Chuang: *Quantum computation and quantum information.* Cambridge University Press, Cambridge, 2009.

[20] M. Saffman, T. G. Walker and K. Mølmer: *Quantum information with Rydberg atoms.* In: *Reviews of Modern Physics* **82**, 3, 2313–2363. 2010.

[21] H. Weimer, M. Müller, I. Lesanovsky, P. Zoller and H. P. Büchler: *A Rydberg quantum simulator.* In: *Nature Physics* **6**, 5, 382–388. 2010.

[22] E. Amaldi and E. Segré: *Effect of Pressure on High Terms of Alkaline Spectra.* In: *Nature* **133**, 3352, 141. 1934.

[23] J. B. Balewski, A. T. Krupp, A. Gaj, D. Peter, H. P. Büchler, R. Löw, S. Hofferberth and T. Pfau: *Coupling a single electron to a Bose-Einstein condensate.* In: *Nature* **502**, 7473, 664–667. 2013.

[24] T. Wilk, A. Gaëtan, C. Evellin, J. Wolters, Y. Miroshnychenko, P. Grangier and A. Browaeys: *Entanglement of two individual neutral atoms using Rydberg blockade.* In: *Physical review letters* **104**, 1, 010 502. 2010.

[25] L. Isenhower, E. Urban, X. L. Zhang, A. T. Gill, T. Henage, T. A. Johnson, T. G. Walker and M. Saffman: *Demonstration of a neutral atom controlled-NOT quantum gate.* In: *Physical review letters* **104**, 1, 010 503. 2010.

[26] H. Gorniaczyk, C. Tresp, J. Schmidt, H. Fedder and S. Hofferberth: *Single-photon transistor mediated by interstate Rydberg interactions.* In: *Physical review letters* **113**, 5, 053 601. 2014.

[27] O. Firstenberg, C. S. Adams and S. Hofferberth: *Nonlinear quantum optics mediated by Rydberg interactions.* In: *Journal of Physics B: Atomic, Molecular and Optical Physics* **49**, 15, 152 003. 2016.

[28] W. D. Phillips, D. J. Wineland, C. E. Wieman and S. J. Smith: *Colder and Better: Some New Developments in Laser Cooling, Trapping and Manipulation of Atoms.* In: *AIP Conference Proceedings*, volume 232, 211–218. 1994.

[29] H. J. Metcalf and P. Straten: *Laser Cooling and Trapping.* Graduate Texts in Contemporary Physics. Springer, New York, 1999.

[30] C. H. Greene, A. S. Dickinson and H. R. Sadeghpour: *Creation of polar and nonpolar ultra-long-range rydberg molecules.* In: *Physical review letters* **85**, 12, 2458–2461. 2000.

[31] V. Bendkowsky, B. Butscher, J. Nipper, J. P. Shaffer, R. Löw and T. Pfau: *Observation of ultralong-range Rydberg molecules.* In: *Nature* **458**, 7241, 1005–1008. 2009.

[32] H. R. Sadeghpour and S. T. Rittenhouse: *How do ultralong-range homonuclear Rydberg molecules get their permanent dipole moments?* In: *Molecular Physics* **111**, 12-13, 1902–1907. 2013.

[33] D. Booth, S. T. Rittenhouse, J. Yang, H. R. Sadeghpour and J. P. Shaffer: *Molecular physics. Production of trilobite Rydberg molecule dimers with kilo-Debye permanent electric dipole moments.* In: *Science (New York)* **348**, 6230, 99–102. 2015.

[34] H. Sassmannshausen, F. Merkt and J. Deiglmayr: *Experimental characterization of singlet scattering channels in long-range Rydberg molecules.* In: *Physical review letters* **114**, 13, 133 201. 2015.

[35] A. Gaj, A. T. Krupp, P. Ilzhöfer, R. Löw, S. Hofferberth and T. Pfau: *Hybridization of Rydberg Electron Orbitals by Molecule Formation.* In: *Physical review letters* **115**, 2, 023 001. 2015.

[36] F. Böttcher, A. Gaj, K. M. Westphal, M. Schlagmüller, K. S. Kleinbach, R. Löw, T. C. Liebisch, T. Pfau and S. Hofferberth: *Observation of mixed singlet-triplet Rb_2 Rydberg molecules.* In: *Physical Review A* **93**, 3. 2016.

[37] K. S. Kleinbach, F. Meinert, F. Engel, W. J. Kwon, R. Löw, T. Pfau and G. Raithel: *Photoassociation of Trilobite Rydberg Molecules via Resonant Spin-Orbit Coupling.* In: *Physical review letters* **118**, 22, 223 001. 2017.

[38] T. Schmid, C. Veit, N. Zuber, R. Löw, T. Pfau, M. Tarana and M. Tomza: *Rydberg Molecules for Ion-Atom Scattering in the Ultracold Regime.* In: *Physical review letters* **120**, 15, 153 401. 2018.

[39] S. Schmid, A. Härter and J. H. Denschlag: *Dynamics of a cold trapped ion in a Bose-Einstein condensate.* In: *Physical review letters* **105**, 13, 133 202. 2010.

[40] C. Zipkes, S. Palzer, C. Sias and M. Köhl: *A trapped single ion inside a Bose-Einstein condensate.* In: *Nature* **464**, 7287, 388–391. 2010.

[41] W. G. Rellergert, S. T. Sullivan, S. Kotochigova, A. Petrov, K. Chen, S. J. Schowalter and E. R. Hudson: *Measurement of a large chemical reaction rate between ultracold closed-shell ^{40}Ca atoms and open-shell $^{174}Yb^+$ ions held in a hybrid atom-ion trap.* In: *Physical review letters* **107**, 24, 243 201. 2011.

[42] A. Härter, A. Krükow, A. Brunner, W. Schnitzler, S. Schmid and J. H. Denschlag: *Single ion as a three-body reaction center in an ultracold atomic gas.* In: *Physical review letters* **109**, 12, 123 201. 2012.

[43] S. T. Sullivan, W. G. Rellergert, S. Kotochigova and E. R. Hudson: *Role of electronic excitations in ground-state-forbidden inelastic collisions between ultracold atoms and ions.* In: *Physical review letters* **109**, 22, 223 002. 2012.

[44] F. H. J. Hall and S. Willitsch: *Millikelvin reactive collisions between sympathetically cooled molecular ions and laser-cooled atoms in an ion-atom hybrid trap.* In: *Physical review letters* **109**, 23, 233 202. 2012.

[45] F. H. Hall, P. Eberle, G. Hegi, M. Raoult, M. Aymar, O. Dulieu and S. Willitsch: *Ion-neutral chemistry at ultralow energies: dynamics of reactive collisions between laser-cooled Ca^+ ions and Rb atoms in an ion-atom hybrid trap.* In: *Molecular Physics* **111**, 14-15, 2020–2032. 2013.

[46] Z. Meir, T. Sikorsky, R. Ben-shlomi, N. Akerman, Y. Dallal and R. Ozeri: *Dynamics of a ground-state cooled ion colliding with ultra-cold atoms.* In: *Physical Review Letters* **117**, 24. 2016.

[47] J. Joger, H. Fürst, N. Ewald, T. Feldker, M. Tomza and R. Gerritsma: *Observation of collisions between cold Li atoms and Yb^+ ions.* In: *Physical Review A* **96**, 3. 2017.

[48] R. Saito, S. Haze, M. Sasakawa, R. Nakai, M. Raoult, H. Da Silva, O. Dulieu and T. Mukaiyama: *Characterization of charge-exchange collisions between ultracold ^6Li atoms and $^{40}Ca^+$ ions.* In: *Physical Review A* **95**, 3, 245. 2017.

[49] K. S. Kleinbach, F. Engel, T. Dieterle, R. Löw, T. Pfau and F. Meinert: *Ionic Impurity in a Bose-Einstein Condensate at Submicrokelvin Temperatures.* In: *Physical review letters* **120**, 19, 193 401. 2018.

[50] T. Dieterle: *An Ion Microscope for spatially resolved Rydberg Atom Detection*. Master thesis, University of Stuttgart. 2017.

[51] D. R. Lide (Editor): *CRC handbook of chemistry and physics: A ready-reference book of chemical and physical data*. 84th edition. CRC Press, Boca Raton, 2003.

[52] D. A. Steck: *Rubidium 87 D Line Data*. Online available at http://steck.us/alkalidata. 2015.

[53] S. A. Lee, B. P. Stoicheff, J. Helmcke and J. L. Hall: *Doppler-free two-photon transitions to Rydberg levels: convenient, useful, and precise reference wavelengths for dye lasers*. In: *Optics Letters* **3**, 4, 141. 1978.

[54] N. Zuber: *Design and Setup of an Ultracold Dual-species Rydberg Experiment*. Master thesis, University of Stuttgart. 2016.

[55] M. P. Bradley, J. V. Porto, S. Rainville, J. K. Thompson and D. E. Pritchard: *Penning Trap Measurements of the Masses of ^{133}Cs, $^{87,85}Rb$, and ^{23}Na with Uncertainties ≤ 0.2 ppb*. In: *Physical Review Letters* **83**, 22, 4510–4513. 1999.

[56] G. Drake: *Springer Handbook of Atomic, Molecular, and Optical Physics*. Springer Science+Business Media, New York, 2006.

[57] C. J. Foot: *Atomic physics*. Oxford University Press, Oxford, 2005.

[58] D. A. Steck: *Quantum and Atom Optics*. Online available at http://steck.us/teaching. 2012.

[59] B. Huber: *Coherent Rydberg dynamics and interaction above room temperature: The frozen gas regime and beyond*. PhD thesis, University of Stuttgart. 2014.

[60] U. Fano: *Description of States in Quantum Mechanics by Density Matrix and Operator Techniques*. In: *Reviews of Modern Physics* **29**, 1, 74–93. 1957.

[61] A. Urvoy: *Large bandwidth excitation of Rydberg atoms in thermal vapor: fast dynamics and strong interaction effects*. PhD thesis, University of Stuttgart. 2016.

[62] G. Lindblad: *On the generators of quantum dynamical semigroups*. In: *Communications in Mathematical Physics* **48**, 2, 119–130. 1976.

[63] K. Mølmer, Y. Castin and J. Dalibard: *Monte Carlo wave-function method in quantum optics*. In: *Journal of the Optical Society of America B* **10**, 3, 524. 1993.

[64] T. Baluktsian: *Rydberg interaction between thermal atoms: Van der Waals-type Rydberg-Rydberg interaction in a vapor cell experiment*. PhD thesis, University of Stuttgart. 2013.

[65] R. Grimm, M. Weidemüller and Y. B. Ovchinnikov: *Optical dipole traps for neutral atoms*. In: *Advances in Atomic, Molecular and Optical Physics* **42**, 95–170. 2000.

[66] B. Arora, M. S. Safronova and C. W. Clark: *Magic wavelengths for the np−ns transitions in alkali-metal atoms*. In: *Physical Review A* **76**, 5, 334. 2007.

[67] B. Arora and B. K. Sahoo: *State-insensitive trapping of Rb atoms: linearly versus circularly polarized lights*. In: *Physical Review A* **86**, 3, 33. 2012.

[68] Q.-Q. Hu, C. Freier, Y. Sun, B. Leykauf, V. Schkolnik, J. Yang, M. Krutzik and A. Peters: *Observation of vector and tensor light shifts in ^{87}Rb using near-resonant, stimulated Raman spectroscopy*. In: *Physical Review A* **97**, 1. 2018.

[69] B. E. A. Saleh, M. C. Teich and J. W. Goodman: *Fundamentals of Photonics*. John Wiley & Sons, New York, 1991.

[70] E. Hecht: *Optics*. 4th edition. Addison-Wesley, San Francisco, 2010.

[71] M. Meister: *Setup of a stable reference cavity for laser spectroscopy*. Diploma thesis, University of Stuttgart. 2008.

[72] T. Kalkbrenner: *Ein Hochfinesse-Resonator mit beweglichem Spiegel als optomechanischer Sensor*. Diploma thesis, University of Konstanz. 1998.

[73] M. Bass (Editor): *Handbook of Optics*, volume 2 of *Fundamentals, Techniques, and Design*. 2nd edition. McGraw-Hill, New York, 1995.

[74] D. A. Steck: *Classical and Modern Optics*. Online available at http://steck.us/teaching. 2017.

[75] C. Tresp: *A Setup for Highly Precise Excitation and Detection of Rydberg Atoms*. Master thesis, University of Stuttgart. 2012.

[76] G. R. Fowles: *Introduction to Modern Optics*. 2nd edition. Dover Publications, New York, 1989.

[77] J. D. Pritchard: *Cooperative Optical Non-linearity in a blockaded Rydberg Ensemble*. PhD thesis, Durham University. 2011.

[78] A. Urvoy: *Set-up of a laser system for precision spectroscopy of highly excited caesium atoms*. Dipolma thesis, University of Stuttgart. 2011.

[79] I. I. Sobelman: *Atomic Spectra and Radiative Transitions*. Springer, Heidelberg, 1992.

[80] L. C. Biedenharn and J. D. Louck: *Angular momentum in quantum physics*. Addison-Wesley, Reading, 1981.

[81] P. Ilzhöfer: *Hybridization of Rydberg molecule orbitals*. Master thesis, University of Stuttgart. 2014.

[82] T. Schmid: *High precision excitation, manipulation and detection of Rydberg atoms*. Master thesis, University of Stuttgart. 2014.

[83] J. Marek and P. Munster: *Radiative lifetimes of excited states of rubidium up to quantum number $n = 12$*. In: *J. Phys. B: At. Mol. Phys.* **13**, 1731. 1980.

[84] M. Viteau, J. Radogostowicz, M. G. Bason, N. Malossi, D. Ciampini, O. Morsch and E. Arimondo: *Rydberg spectroscopy of a Rb MOT in the presence of applied or ion created electric fields*. In: *Optics express* **19**, 7, 6007–6019. 2011.

[85] R. Heidemann: *Rydberg Excitation of Bose-Einstein Condensates: Coherent Collective Dynamics*. PhD thesis, University of Stuttgart. 2008.

[86] E. Brion, L. H. Pedersen and K. Mølmer: *Adiabatic elimination in a Lambda system*. In: *Journal of Physics A: Mathematical and Theoretical* **40**, 5, 1033. 2007.

[87] H. Walther: *Advances in Atomic, Molecular, and Optical Physics*, volume 46 of *Advances In Atomic, Molecular, and Optical Physics*. 1. edition. Elsevier textbooks, 2001.

[88] B. C. Duncan, V. Sanchez-Villicana, P. L. Gould and H. R. Sadeghpour: *Measurement of the Rb $(5D_{1/2})$ photoionization cross section using trapped atoms*. In: *Physical Review A* **63**, 4, 043 411. 2001.

[89] Melles Griot: *Fundamental Optics*. Online available at www.cvimellesgriot.com. 2016.

[90] J. C. B. Kangara, A. J. Hachtel, M. C. Gillette, J. T. Barkeloo, E. R. Clements, S. Bali, B. E. Unks, N. A. Proite, D. D. Yavuz, P. J. Martin, J. J. Thorn and D. A. Steck: *Design and construction of cost-effective tapered amplifier systems for laser cooling and trapping experiments*. In: *American Journal of Physics* **82**, 8, 805–817. 2014.

[91] F. Christaller: *Aufbau und Charakterisierung von einem Lasersystem zur schmalbandigen Anregung von Rydberg-Atomen*. Bachelor thesis, University of Stuttgart. 2015.

[92] J. Balewski: *Hochauflösende Photoassoziationsspektroskopie von Rydberg-Dimeren und Trimeren*. Diploma thesis, University of Stuttgart. 2009.

[93] R. W. P. Drever, J. L. Hall, F. V. Kowalski, J. Hough, G. M. Ford, A. J. Munley and H. Ward: *Laser phase and frequency stabilization using an optical resonator*. In: *Applied Physics B Photophysics and Laser Chemistry* **31**, 2, 97–105. 1983.

[94] Toptica Photonics AG: *Sys DC 110 Diode Laser Supply Electronics Manual: Version 08, May 2013.*

[95] J. R. Lowell, T. Northup, B. M. Patterson, T. Takekoshi and R. J. Knize: *Measurement of the photoionization cross section of the $5S_{1/2}$ state of rubidium.* In: *Physical Review A* **66**, 6, R5. 2002.

[96] S. Kraft, A. Günther, J. Fortágh and C. Zimmermann: *Spatially resolved photoionization of ultracold atoms on an atom chip.* In: *Physical Review A* **75**, 6. 2007.

[97] R. V. Ambartzumian, N. P. Furzikov, V. S. Letokhov and A. A. Puretsky: *Measuring photoionization cross-sections of excited atomic states.* In: *Applied Physics* **9**, 4, 335–337. 1976.

[98] K. S. Kleinbach: *Ions and Electrons Interacting with Ultracold Atoms: Novel Approaches Based on Rydberg Excitations.* PhD thesis, University of Stuttgart. 2018.

[99] D. C. McKay: *Quantum simulation in strongly correlated optical lattices.* PhD thesis, University of Illinois. 2012.

[100] L. Jönsson: *Energy shifts due to the ponderomotive potential.* In: *Journal of the Optical Society of America B* **4**, 9, 1422. 1987.

[101] R. R. Freeman, P. H. Bucksbaum and T. J. McIlrath: *The ponderomotive potential of high intensity light and its role in the multiphoton ionization of atoms.* In: *IEEE Journal of Quantum Electronics* **24**, 7, 1461–1469. 1988.

[102] F. Markert, P. Würtz, A. Koglbauer, T. Gericke, A. Vogler and H. Ott: *ac-Stark shift and photoionization of Rydberg atoms in an optical dipole trap.* In: *New Journal of Physics* **12**, 11, 113 003. 2010.

[103] M. Aymar, O. Robaux and S. Wane: *Central-field calculations of photoionisation cross sections of excited states of Rb and Sr^+ and analysis of photoionisation cross sections of excited alkali atoms using quantum defect theory.* In: *Journal of Physics B: Atomic and Molecular Physics* **17**, 6, 993–1007. 1984.

[104] E. Courtade, M. Anderlini, D. Ciampini, J. H. Müller, O. Morsch, E. Arimondo, M. Aymar and E. J. Robinson: *Two-photon ionization of cold rubidium atoms with a near resonant intermediate state.* In: *Journal of Physics B: Atomic, Molecular and Optical Physics* **37**, 5, 967–979. 2004.

[105] M. Anderlini and E. Arimondo: *Control scheme for two photon ionization of condensate atoms.* In: *Optics Communications* **259**, 2, 676–682. 2006.

[106] J. W. Cooper: *Photoionization from Outer Atomic Subshells. A Model Study.* In: *Physical Review* **128**, 2, 681. 1962.

[107] U. Fano and J. W. Cooper: *Spectral Distribution of Atomic Oscillator Strengths.* In: *Reviews of Modern Physics* **40**, 3, 441–507. 1968.

[108] I. I. Beterov, C. W. Mansell, E. A. Yakshina, I. I. Ryabtsev, D. B. Tretyakov, V. M. Entin, C. MacCormick, M. J. Piotrowicz, A. Kowalczyk and S. Bergamini: *Cooper minima in the transitions from low-excited and Rydberg states of alkali-metal atoms.* Online available at http://arxiv.org/pdf/1207.3626v1.

[109] V. A. Zilitis: *Theoretical determination of oscillator strengths for the principal series of rubidium-like ions by the Dirac-Fock method.* In: *Optics and Spectroscopy* **107**, 1, 54–57. 2009.

[110] T. P. Dinneen, C. D. Wallace, K.-Y. N. Tan and P. L. Gould: *Use of trapped atoms to measure absolute photoionization cross sections.* In: *Optics Letters* **17**, 23, 1706. 1992.

[111] C. Gabbanini, S. Gozzini and A. Lucchesini: *Photoionization cross section measurement in a Rb vapor cell trap.* In: *Optics Communications* **141**, 1-2, 25–28. 1997.

[112] H. Wei, R. Ya-Ping, J. Feng-Dong, Z. Yin-Peng, L. Long-Wei, D. Xing-Can, X. Ping, X. Xiang-Yuan and Z. Zhi-Ping: *Measurement of the Absolute Photoionization Cross Section for the $5P_{3/2}$ State of ^{87}Rb in a Vapor Cell Magneto-optic Trap.* In: *Chinese Physics Letters* **29**, 1, 013 201. 2012.

[113] T. Aoki, Y. Yamanaka, M. Takeuchi, Y. Torii and Y. Sakemi: *Photoionization loss in simultaneous magneto-optical trapping of Rb and Sr.* In: *Physical Review A* **87**, 6. 2013.

[114] N. Amin, S. Mahmood, M. Anwar-ul Haq, M. Riaz and M. A. Baig: *Measurement of the photoionization cross-section of the $3p\ ^2P_{1/2,3/2}$ excited levels of sodium.* In: *The European Physical Journal D* **37**, 1, 23–28. 2006.

[115] A. Nadeem and S. U. Haq: *Photoionization from the $5p\ ^2P_{3/2}$ state of rubidium.* In: *Physical Review A* **83**, 6, 141. 2011.

[116] R. Côté: *From classical mobility to hopping conductivity: charge hopping in an ultracold gas.* In: *Physical Review Letters* **85**, 25, 5316–5319. 2000.

[117] L. Schmid: *Setting up an optical accordion lattice to determine the resolution of a Rydberg ion imaging system.* Bachelor thesis, University of Stuttgart. 2018.

Danksagung

An dieser Stelle möchte ich mich bei allen bedanken, die zum Gelingen dieser Masterarbeit beigetragen haben und mich bei der täglichen Arbeit am Institut unterstützt haben.

Zunächst wäre Herr Prof. Dr. Tilman Pfau zu nennen, der mich nach meiner Bachelorarbeit wieder am 5. Physikalischen Institut aufgenommen hat und hier einwandfreie Arbeitsbedingungen für die alltägliche Forschung schafft. Herzlichen Dank auch dafür, dass Sie es mir ermöglicht haben, Konferenzen in Erlangen, Glasgow und Hamburg zu besuchen und dort meine Forschungsergebnisse vorzustellen.

Ich danke Herrn PD Dr. Eberhard Goering, der den Mitbericht dieser Arbeit übernommen hat. Vielen Dank, dass Sie sich die Zeit genommen haben, sich mit den Geheimnissen der Atomphysik auseinanderzusetzen. Besonders gefreut hat mich auch Ihr Besuch im Rybli-Labor, den Sie genutzt haben, um sich meinen Aufbau vor Ort anzuschauen.

Christian Veit, Thomas Schmid und Nicolas Zuber ist für die hervorragende Betreuung über das gesamte letzte Jahr, die Hilfe bei der Lösung von experimentellen und theoretischen Problemen sowie für die Korrektur dieser Arbeit äußerst zu danken. Ihr habt eine sehr angenehme Arbeitsatmosphäre geschaffen, bei der ich trotz allem Frust, den die Atomphysik manchmal so mit sich bringt, große Freude bei der täglichen Arbeit hatte. Vielen Dank auch für die gemeinsamen Abendessen und Umtrünke zur Feier kleiner Meilensteine am Experiment. Ich habe eine tolle Zeit am Rybli-Experiment verbracht und enorm viel von euch gelernt! Für das Experiment wünsche ich euch auch in Zukunft bestes Gelingen und viele aufregende Forschungsergebnisse.

Der Superatoms-Gruppe um Felix Engel, Thomas Dieterle und Florian Meinert danke ich, dass ich das 1010 nm Lasersystem an ihrem laufenden Experiment testen durfte und Messzeit an ihrer Apperatur bekommen habe, um Messungen für meine Arbeit durchzuführen. Vielen Dank für die Geduld beim Erklären des Experiments und für die Möglichkeit, so eine Maschine auch mal alleine zu bedienen.

Allen bis jetzt nicht genannten Mitarbeiterinnen und Mitarbeitern am 5. Physikalischen Institut möchte ich für die tolle Arbeitsatmosphäre danken. Sowohl kleine Denkanstöße als auch ausufernde Diskussionen haben mir stets einen neuen Blickwinkel auf physikalische Probleme ermöglicht und mir neue Denkanstöße gegeben.

Julian Feile, Max Wohltmann und Stefan Jesenski ist für weitere Korrekturen dieser Arbeit zu danken. Vielen Dank, dass ihr eure Freizeit geopfert habt, um in eine völlig neue Welt einzutauchen und nach Fehlern in meiner Arbeit zu fischen.

Dem Verwaltungsteam am Institut, insbesondere Kati Kriesch und Astrid Buck, danke ich für die kompetente Hilfe beim ein oder anderen Verwaltungsakt.

Bei Gabriele Untereiner vom 1. Physikalischen Institut bedanke ich mich für die ausführliche und schnelle Hilfe bei der Herstellung eines Spiegels für den Transferresonator.

Ich möchte meiner Familie danken, die mich während des gesamten Studiums finanziell und ideell unterstützt und mir den Rücken freigehalten hat. Vielen, vielen Dank dafür! Zuletzt danke ich meiner Freundin Julia. Herzlichen Dank für deine Treue, deine immerwährende Unterstützung und die großartige Zeit außerhalb der wunderbaren Welt der Physik.